Order Number 9419757

Circulation variability in the Bering Sea

Okkonen, Stephen Richard, Ph.D.

University of Alaska Fairbanks, 1993

U·M·I
300 N. Zeeb Rd.
Ann Arbor, MI 48106

CIRCULATION VARIABILITY IN THE BERING SEA

A

THESIS

Presented to the Faculty

of the University of Alaska Fairbanks

in Partial Fulfillment of the Requirements

for the Degree of

DOCTOR OF PHILOSOPHY

By

Stephen Okkonen, B.S.

Fairbanks, Alaska

December 1993

CIRCULATION VARIABILITY IN THE BERING SEA

By

Stephen Richard Okkonen

RECOMMENDED:

Chairman, Advisory Committee

Department Head

APPROVED:

Dean, School of Fisheries and Ocean Sciences

Edward C Murphy

Dean of the Graduate School

15 December 1993

Date

Abstract

Sea surface height anomalies measured by the GEOSAT radar altimeter are used to develop an improved circulation scheme for the deep basin of the Bering Sea and to make inferences about the dynamics controlling the circulation. A conceptual model of the circulation in the Bering Sea is presented in three manuscripts. The first provides a description of a large eddy in the Alaskan Stream. This eddy is shown to influence circulation in the southern Aleutian Basin. The second manuscript reports on an empirical orthogonal function analysis of averaged sea surface height anomalies. The analysis is interpreted to describe the superposition of two principal circulation schemes. The former describes annual period, basin scale cyclonic circulation. The latter scheme reflects the southwestward propagation of ~1.9 year period, gyre scale baroclinic long waves across the Aleutian Basin. The final paper reports on observations of topographic planetary waves associated with the Bering Slope Current. The model provides a possible resolution of some of the discrepancies between previously published circulation schemes for the Bering Sea.

Table of Contents

List of Figures

List of Tables

Acknowledgments

I would like to thank my wife, Joann Jackinsky, and my children, Eero and Kaija, for their patience and love. I am indebted to my advisor, Joe Niebauer, for his support and the opportunities presented to me.

Chapter 1 Introduction

This work began with a rather innocent and somewhat nebulous desire to 'study the ocean using satellites'. Fortunately, Joe Niebauer and Walt Johnson admonished me to narrow my focus a bit. This thesis represents my efforts to adhere to that admonition.

The problem driving this research can, for the most part, be illustrated by a few of the many charts of circulation schemes proposed for the Bering Sea (Figure 1.1 to Figure 1.4) since the first chart of surface currents was published by Dall in 1882. While there are similarities, the differences between schemes are immediately apparent. That there have been so many schemes (see Hughes et al., 1974 for a review) is indicative of the difficulties encountered in attempting to describe the circulation. The principal inadequacy, owing to the remoteness and often inhospitable environment of the Bering Sea, has been a limited data base. Most researchers have relied on a compilation of their own data with that of previous investigators to obtain sufficient coverage and resolution of the circulation features in order to develop schemes for the entire sea (e.g. Dobrovol'skii and Arsen'ev 1959; Arsen'ev 1967; Hughes et al. 1974; and Sayles et al. 1979).

The inherent temporal and spatial sampling limitations associated with shipboard acquisition of oceanographic data are largely overcome by satellite borne instruments, although satellite observations are restricted to processes and phenomena which have surface signatures. That a satellite borne altimeter could be used to measure sea surface topography

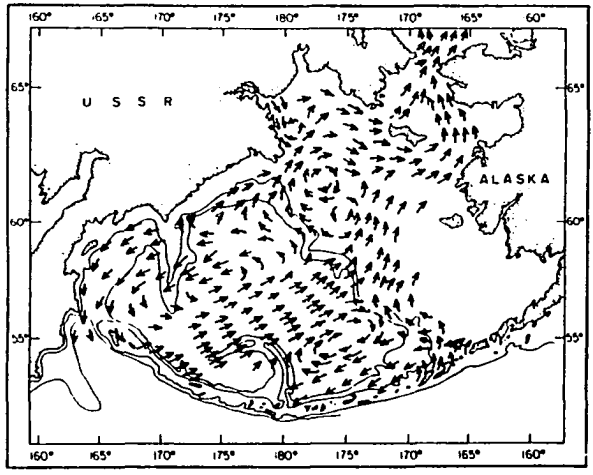

Figure 1.1 Bering Sea circulation according to Ratmanov (1937) (after Hughes et al., 1974).

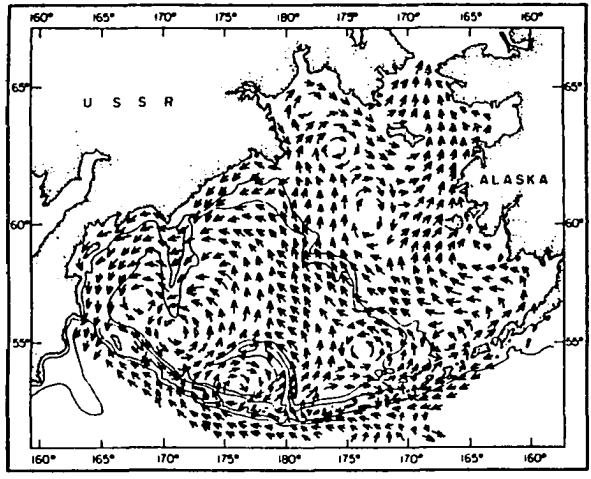

Figure 1.3 Bering Sea circulation according to Arsen'ev (1967) (after Hughes et al., 1974).

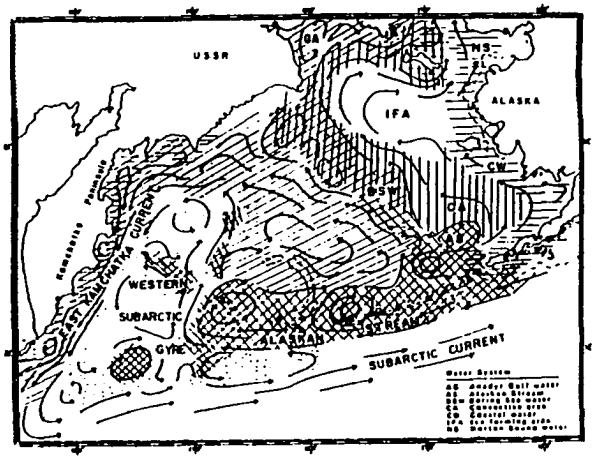

Figure 1.2 Bering Sea circulation according to Takenouti and Ohtani (1974).

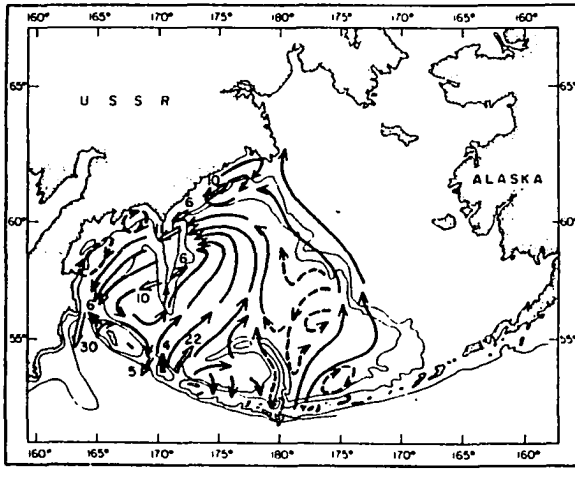

Figure 1.4 Bering Sea circulation according to Hughes et al. (1974).

and ocean currents was first proposed by Greenwood et al. (1969). That idea has been partially realized with the deployment of GEOS-3 in 1975 (Agreen, 1982), SEASAT in 1978 (Born et al., 1979), GEOSAT in 1985 (McConathy and Kilgus, 1987), and most recently by TOPEX/POSEIDEN in 1992. Although the goal of determining the quasi-instantaneous absolute current field over the world ocean has yet to be achieved, an accurate determination of the time varying components of ocean currents has been demonstrated (e.g. Douglas and Cheney, 1981; Cheney and Marsh, 1981; Chelton et al., 1990).

The objective of this thesis is to apply this proven methodology using sea surface heights measured by the GEOSAT altimeter to develop an improved circulation scheme for the deep basin of the Bering Sea and to make inferences about the dynamics controlling the circulation. Aspects of the circulation in the Bering Sea, based upon my own work, are reported in three manuscripts. The first begins with a description of a large eddy in the Alaskan Stream. This manuscript concludes with the supposition that the eddy influences circulation in the Bering Sea. The second manuscript uses an empirical orthogonal function analysis of averaged sea surface height anomalies to provide a perspective of low frequency basin scale and gyre scale circulation. The final paper reports on observations of planetary waves associated with the Bering Slope Current.

Chapter 2 Data and Methods

Introduction

This chapter reviews the theory behind the measurement of sea surface topography using a satellite borne radar altimeter and the methods by which this is accomplished.

Section 2.1 Sea surface topography from satellite altimetry

The sea surface is of interest to physical oceanographers because many dynamical ocean phenomena manifest themselves as changes in its topography. In particular, ocean currents reveal themselves in the sea surface topography according to the geostrophic and hydrostatic approximations. Logistical problems associated with shipboard acquisition of hydrographic data limit the temporal and spatial resolution of (dynamic) topographies constructed from this data. Satellites provide the best platform from which sensors can make synoptic measurements of oceanographic data on regional and global scales. Among the suite of sensors available to the oceanographer is the radar altimeter which can potentially measure the sea surface topography directly.

A quantitative description of sea surface topography requires, as does a description of terrestrial topography, a level surface as a datum. A level surface is an equipotential surface normal to the local effective gravity

force. A convenient equipotential surface is the geoid. The geoid is that equipotential surface which intersects mean sea level. If the ocean was at rest, its surface would define the geoid for the ocean covered areas of the earth. It is readily apparent that ship motion and the dearth of landmarks preclude using standard surveying techniques to describe the sea surface topography relative to the geoid. However, the recent deployment of a series of satellite borne altimeters has demonstrated the possibility of measuring the topography of the sea surface.

A satellite borne altimeter is a radar. It transmits a continuous stream of short pulses toward the earth which after being reflected from the surface are received by the radar. The instantaneous height of the altimeter above the earth's surface can be determined from the round trip travel time of each pulse and its speed through the intervening ionosphere and atmosphere.

Measuring the dynamic topography, the height of the sea surface above the geoid, first requires a record of the satellite's orbital height and position with respect to the center of the earth or to some reference surface (Fig. 2.1). This orbital record is the satellite's ephemeris. The GEOSAT ephemeris is based on a model of the earth's gravity field and Doppler tracking observations of the satellite. Because the shape of the earth is irregular, it is more convenient to approximate it as an ellipsoid to which the ephemeris can be referred.

These two measurements, the height of the altimeter above the sea surface, H_a, and the orbital height of the altimeter (satellite) above the reference ellipsoid, H_o, allow the height of the sea surface with respect

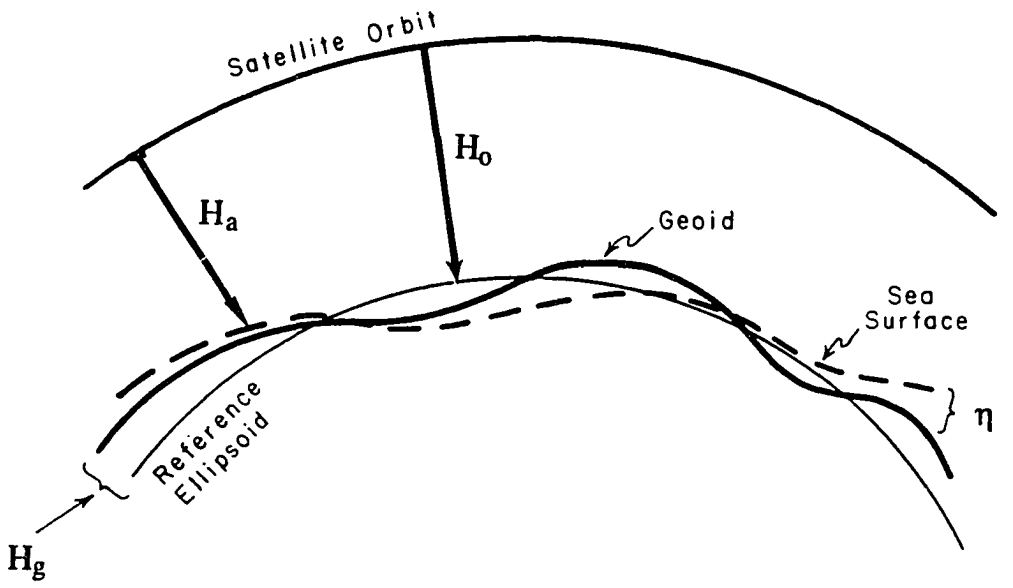

Figure 2.1 Schematic of measurements required to determine the sea surface topography.

to the reference ellipsoid, H_s, to be determined

$$H_s(x,y,t) = H_o(x,y,t) - H_a(x,y,t), \qquad (2.1)$$

where positive x and y are directed toward the east and north, respectively, and t represents the time variable. Because of the non-uniform distribution of the earth's mass within its volume, the geoid and the surface of the reference ellipsoid do not coincide everywhere. The geoid deviates from the ellipsoid over a range of -104 m to +64 m (Robinson, 1985). Consequently, the height of the geoid relative to the reference ellipsoid, H_g, must also be known in order to determine the dynamic sea surface topography, η. It follows then that

$$\eta(x,y,t) = H_s(x,y,t) - H_g(x,y). \qquad (2.2)$$

The next section will describe how the current field is obtained from the sea surface topography.

2.2 The geostrophic balance

Steady ocean currents for which dissipative processes can be neglected are described as being in geostrophic balance. The resulting approximations to the horizontal equations of motion, in which the pressure gradient force driving the current is balanced by Coriolis force, obtain:

$$fv = \frac{1}{\rho}\frac{\partial p}{\partial x}, \tag{2.3}$$

$$fu = -\frac{1}{\rho}\frac{\partial p}{\partial y}, \tag{2.4}$$

where u and v are the velocities in the x and y directions, ρ is the density of sea water, p is the local fluid pressure, and f is the Coriolis parameter given by

$$f = 2\,\Omega \sin\phi, \tag{2.5}$$

where Ω is the rotation rate of the earth and ϕ is the latitude. Geostrophic currents vary on length scales of order 10 km and larger and vary on time scales exceeding a few days.

The vertical distribution of mass in the ocean is well described for the length and time scales appropriate for the geostrophic approximation by the hydrostatic approximation

$$\frac{\partial p}{\partial z} = -\rho g, \tag{2.6}$$

where z is the positive upward direction and g is the gravitational acceleration.

In the ocean where the temperature and salinity fields produce both a horizontal and vertical distribution of density there will be a vertical shear in the horizontal geostrophic currents. By using (2.6) to eliminate the pressure from the vertical derivative of (2.3) and (2.4) and then vertically integrating the result from arbitrary levels z1 to z2, the integral form of the thermal wind equations, describing the vertical shear, are obtained

$$v_{z2} - v_{z1} = -\frac{g}{\rho f}\int_{z1}^{z2}\frac{\partial \rho}{\partial x}dz \quad , \tag{2.7}$$

$$u_{z2} - u_{z1} = \frac{g}{\rho f}\int_{z1}^{z2}\frac{\partial \rho}{\partial y}dz \quad , \tag{2.8}$$

where u_{z1} and v_{z1} are the components of the geostrophic velocity at level z1 and u_{z2} and v_{z2} are their counterparts at level z2.

It is apparent from (2.7) and (2.8) that the absolute geostrophic velocity field in a given domain of the ocean can be determined provided both the geostrophic velocity at some level and the hydrography over that domain are known. Because of the difficulty and expense of acquiring direct measurements of currents over large areas, physical oceanographers have relied on the assumption that there is a level of no motion in the ocean.

Satellite altimetric measurements of sea surface topography provide the means by which the oceanographer can eliminate the need for assuming a level of no motion by choosing the sea surface as a reference level and the surface currents as the reference currents. It can be shown

through the hydrostatic and geostrophic approximations that geostrophic surface currents are proportional to the slope of the sea surface (relative to the geoid):

$$v_s = \frac{g}{f}\frac{\partial \eta}{\partial x} \tag{2.9}$$

$$u_s = -\frac{g}{f}\frac{\partial \eta}{\partial y}, \tag{2.10}$$

where u_s and v_s are the geostrophic surface currents. At mid-latitudes, a 10 cm s^{-1} current will have a slope of about 10^{-6}, or 10 cm in 100 km. In order to accurately compute the surface geostrophic current the slope of the geoid must be known to an accuracy exceeding that of actual sea surface slope associated with the current. At present there are only a very few areas of limited extent for which a geoid description of this accuracy exists. Unfortunately, this limitation precludes using satellite altimetry to accurately determine the absolute surface geostrophic currents over most of the world ocean.

However, the time varying surface currents can be derived from altimetric measurements without the need for a geoid. By separating the sea surface heights above the geoid and ellipsoid into mean and perturbation components:

$$\eta(x,y,t) = \overline{\eta}(x,y) + \eta'(x,y,t), \tag{2.11}$$

$$H_s(x,y) = \overline{H_s}(x,y) + H_s'(x,y,t), \tag{2.12}$$

where the overbar indicates the temporal mean and the prime indicates the perturbation, and making use of the definition for mean sea surface height above the ellipsoid,

$$\overline{H_s}(x,y) = \overline{\eta}(x,y) + H_g, \tag{2.13}$$

substitution into (2.2) gives the time varying component of sea surface topography

$$\eta'(x,y,t) = H_s'(x,y,t). \tag{2.14}$$

While the terms on the right hand side of (2.13) are not explicitly known, $\overline{H_s}$ can be computed by averaging (2.1) using the measurements acquired by the satellite as it repeatedly passes over a given location on the ocean surface.

Section 2.3 Altimeter data and its processing

At the conclusion of a classified geodetic mission, the GEOSAT altimetric satellite (see McConathy and Kilgus, 1987 for a mission description) was maneuvered into an orbit which repeated itself every 17.0505 days. The altimetric coverage provided by the satellite orbit traced out a pattern of 244 adjacent ground tracks separated by 1.475 degrees of longitude with repeating tracks exhibiting a cross-track excursion of less than 1 km. The unclassified phase of operation was called the GEOSAT Exact Repeat Mission (ERM). The data from the ERM were processed by the National Oceanic and Atmospheric Administration's (NOAA) National Ocean Service into two Geophysical Data Record (GDR) sets; one for ocean heights (above a reference ellipsoid) (Cheney et al., 1987) and one for land and ice heights.

The altimetric data set used in the analysis for this study is the JPL-Oceans-8902 version of the GEOSAT altimetry oceans GDR (Zlotnicki et al., 1990). It is an edited and condensed version of the NOAA GDR. The JPL version is the product of a series of steps (see Zlotnicki et al., 1990 for details), the most important of which:

1) delete from the NOAA GDR those records for which instrument noise and signal strength criteria were not met,

2) apply environmental corrections (i.e. ocean tide, wet troposphere, dry troposphere, ionosphere, and inverse barometer) to the sea surface heights (SSH),

3) interpolate the corrected sea surface heights to a fixed set of points ('normal points') along the orbital ground tracks which have a nominal along-track spacing of 7.013 km,

4) assign the interpolated sea surface heights from one orbital period to one of the appropriate 244 ascending (south to north) files or 244 descending (north to south) files.

There are errors associated with all of the environmental corrections applied in step two. The error budget is summarized in Table 2.1. The largest of the errors are associated with the determination of the satellite's orbit. Because the orbit error has a wavelength of roughly the circumference of the earth it can be modeled as a low order polynomial over segments of an orbit and then removed. Of the remaining errors, the wet troposphere and ocean tide are the most problematic. The presence of moisture in the troposphere slows the radar pulse resulting in an overestimate of the distance between the altimeter and the sea surface. The global distribution of water vapor is predicted by the Fleet Numerical Oceanographic Center (FNOC) 2.5° x 2.5° atmospheric general circulation model. The wet troposphere height uncertainty varies over spatial scales approximating those of mesoscale oceanic phenomena potentially masking real mesoscale oceanic features or introducing variations in the height measurements which are falsely interpreted as oceanic features. The wet troposphere correction diminishes with increasing latitude such that, north of 35°N, it is about a third of that in the equatorial regions (Zlotnicki et al., 1989). Consequently, the wet troposphere error correction, as applied, was assumed to be adequate.

Table 2.1 GEOSAT measurement uncertainty (from Lybanon and Crout, 1987).

Error source	Uncertainty 1σ (cm) *Baseline mission*	*Wavelength of error (kilometers)*
Altimeter		
Instrument noise	2	
Bias drift	2	>10000
Time tag	0.2	20000
Tracker bias	2	200-1000
Media		
Electromagnetic bias	2	200-1000
Skewness	1	200-1000
Troposphere (dry)	0.7	1000
Troposphere (wet)	6	200
Ionosphere	4	>1000
Orbit		
Gravity	80	>10000
GM	2	10000
Atmospheric drag	10	10000
Troposphere	1	10000
Solar radiation pressure	10	10000
Earth albedo	2	10000
Earth/ocean tides	1	10000
Station coordinates	10	10000
Station/spacecraft clocks	10	10000
Higher order ionosphere	5	10000
root sum squares	83	

Although the global uncertainty associated with tidal errors is about 1 cm locally there can be errors of about 10 cm associated with the aliasing of the M2 tide (Jacobs et al., 1991). In addition to tidal errors, there remain significant errors associated with the satellite's orbit. These errors collectively introduce an uncertainty of order 1 m into the measurement of the altimeter's height above the sea surface, H_a. The removal of the orbit error begins with the computation of sea surface height anomalies. The removal of the tidal alias error will be described later in this section.

Raw sea surface heights at the normal points on ascending and descending orbital tracks lying within the region bounded by meridians 140°E and 120°W, parallels 35°N and 72°N, and acquired during the two years (1987-1988) corresponding to ERM orbital cycles (henceforth ERMs) 4-46, were read from the JPL tapes. Each orbital track was assigned an identifying index corresponding to the longitude of its equator crossing measured eastward from the Greenwich meridian. For example, the ascending orbital track which crosses the equator immediately east of the Greenwich meridian at 1.003°E is identified as orbital ground track 001A. The ascending tracks lying immediately to the east and west (equator crossing longitudes of 2.478°E and 359.545°E) of 001A are identified as orbital tracks 002A and 244A, respectively. The descending orbital track which crosses the equator immediately east of the Greenwich meridian at 0.3°E is identified as 001D. Moving eastward, the identifying index for each successive orbital track increments by one. The coverage of the North Pacific Ocean afforded by the orbital ground tracks is shown in Figure 2.2.

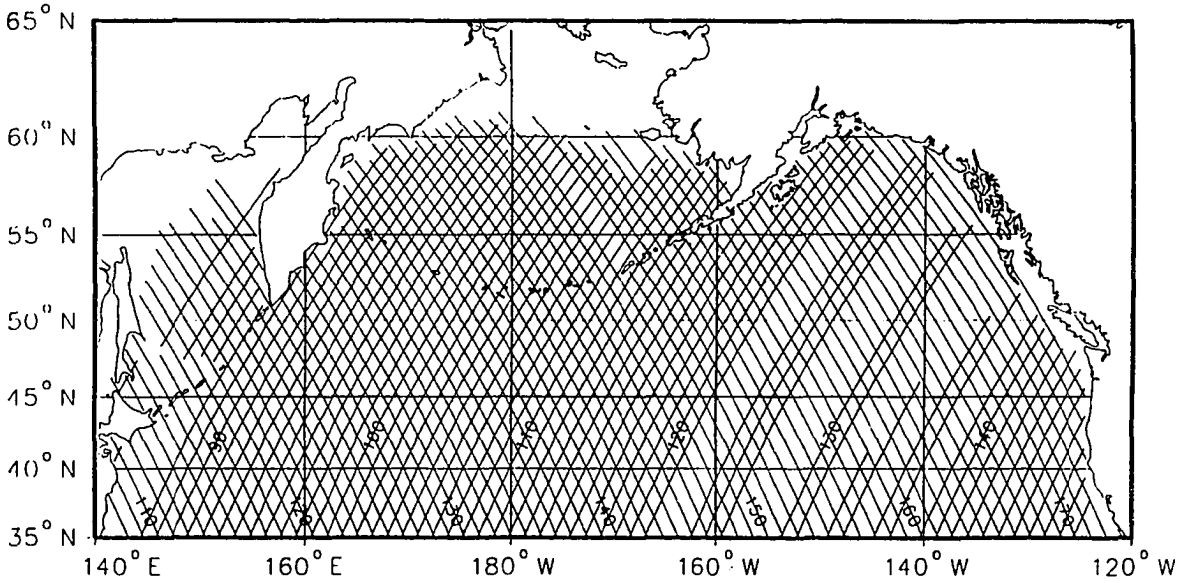

Figure 2.2 A map of ERM 10 orbital ground track segments in the North Pacific along which measurements by the altimeter were acquired.

Sea surface height anomalies (SSHa) are computed using a slightly modified version of the collinear tracks method (Cheney et al., 1983) which begins with the computation of the mean SSH at each normal point x_m,

$$\bar{h}(x_m) = \sum_{n=1}^{N_m} h_n(x_m) \quad , \tag{2.15}$$

where $\bar{h}$ is the arithmetic mean, N_m is the number of ERMs for which there are SSH measurements at x_m, and the subscripts n and m represent the ERM and normal point location, respectively.

A first estimate of the SSHa, uncorrected for orbit error, at each normal point is simply the difference between the raw SSH and the arithmetic mean of SSH

$$h_n'(x_m) = h_n(x_m) - \bar{h}(x_m). \tag{2.16}$$

where h' is the raw SSHa.

There is a problem with the anomalies computed using the arithmetic mean. Because the number of valid raw measurements at each normal point varies, there can be artificial jumps in the along track profiles of arithmetic mean sea level. Inspection of (2.16) indicates that these discontinuities would then manifest themselves in the raw SSH anomalies.

The discontinuities described above are eliminated by replacing the arithmetic mean of SSH in (2.16) with an 'improved mean' (Chelton et al., 1990). The procedure by which the improved mean is obtained begins with the computation of the mean of the finite difference estimate of the along-track derivative of SSH

$$\overline{\Delta h}(x_m) = \frac{1}{N_m} \sum_{n=1}^{N_m} h_n(x_m) - h_n(x_{m-1}) \quad , \tag{2.17}$$

where $\overline{\Delta h}$ is the mean of the along-track first differences of SSH and N_m is the number of ERMs for which there exists a SSH at each of the normal points x_m and x_{m-1}.

Integrating (2.17) gives the improved mean of SSH

$$\overline{h}(x_m) = \overline{h_0} + \sum_{m=1}^{M} \overline{\Delta h}(x_m) \quad , \tag{2.18}$$

where M is the number of normal points in each continuous, unbroken segment of the ground track, and $\overline{h_0}$ is an integration constant for each continuous ground track segment. This integration constant is the coefficient in a weighted least squares procedure which minimizes

$$\sum_{m=1}^{M} w_N\{h_o - [\bar{h}(x_m) - \overline{\Delta h}(x_m)]\}^2 \quad , \tag{2.19}$$

where M is the number of normal points along a given ground track at which both $\bar{h}(x_m)$ and $\overline{\Delta h}(x_m)$ exist, and where w_N is a bell shaped weighting function which has a value of 1 when there is the maximum number of values for both $\bar{h}(x_m)$ and $\overline{\Delta h}(x_m)$ (i.e.N=43) and has a value of 0 when N=0.

Introducing the improved mean into (2.16) gives SSH anomalies which are still contaminated by errors associated with uncertainties in the modeled ephemeris. The radial orbit error has an rms amplitude of 2.2 m (Zlotnicki et al., 1990). However, the wavelength of this error is of the order of the earth's circumference. Consequently, over restricted domains such as that employed for this study the error can be modeled as a low order polynomial fit to the along-track profiles of the SSHa.

The orbit error is estimated in a two step procedure. In the first step, a least squares fit of a quadratic to each profile of SSHa (calculated using the improved mean) is computed. The estimated variance of the residual SSH at each normal point, $\sigma^2(x_m)$, is given by

$$\sigma^2(x_m) = \frac{1}{N_m - 1} \sum_{n=1}^{N_m} \{h'_n(x_m) - [a(t)x_m^2 + b(t)x_m + c(t)]\}^2 \quad , \tag{2.20}$$

where a, b, and c are the coefficients of the quadratic fit for the nth ERM. The orbit error contaminating the SSHa was estimated by a second least squares fit performed on each individual profile of SSHa. The least squares procedure, this time weighted by the inverse of the variance, minimizes

$$\sum_{m=1}^{M} \frac{1}{\sigma^2(x_m)} \{h'_n(x_m) - [a(t)x_m^2 + b(t)x_m + c(t)]\}^2 \qquad (2.21)$$

where a, b, and c are the coefficients of the modeled orbit error for nth ERM. The weighted least squares procedure serves to reduce the bias associated with eddies and large geoid gradients.

Subtracting the appropriate orbit error from each along-track profile of SSHa produces the set of SSHa profiles corrected for orbit error, h",:

$$h''_n(x_m) = h'_n(x_m) - [a(t)x_m^2 + b(t)x_m + c(t)]. \qquad (2.22)$$

The final error in the anomaly data for which a correction was applied is associated with the Schwiderski (1980) tidal model. Because tidal frequencies are higher than the frequency at which GEOSAT measures SSH, the component of SSH due to errors in the tidal model is aliased to lower frequencies. The alias frequencies for the major tidal constituents are given by Cartwright and Ray (1990). The constituent having the largest error is the M2 tide. Its alias frequency is 1.15 cpy which translates to a period of 317 days.

Jacobs et al. (1991) show that about 80% of the SSH variability at a 1.15 cpy frequency leaks into the annual signal of SSH variability. Some of the principal forcing mechanisms for the ocean (wind and buoyancy) have annual signals. The basin scale response of the ocean, insofar as it can be described by linear dynamics, will also occur at an annual period. It is therefore desirable to estimate and remove the tidal error due to aliasing which contaminates the SSHa at this stage of processing.

In addition to the temporal aliasing of the M2 tide, spatial aliasing occurs due to the relatively long interval between sampling along adjacent ground tracks. For measurements at a pair of normal points having the same latitude but lying on adjacent ground tracks, the measurement at the more eastward normal point occurs 3.0048 days (43 orbits x 100.626 min/orbit) after the measurement at the more westward normal point. During this time the M2 tide undergoes a little less than six cycles. If, at a given time, the tide is assumed to have the same amplitude and phase at both normal points, the measured phase at the more eastward point leads the measured phase of its more westward neighbor by about 69.8 degrees. Consequently, the aliased M2 tide manifests itself in the SSHa field as a westward propagating wave whose wavelength is a little more than 5 ground track spacings. This is significant because the phase speed associated with the aliased M2 tide is about that of a mid-latitude, annual period, baroclinic Rossby wave.

A two step procedure is used to estimate the tidal height error (Jacobs et al., 1991). In the first step, a least squares procedure fits a 1.15 cpy sinusoidal function with a constant bias and a time dependent linear trend to the time series of SSHa at each normal point. The resulting estimated sine and cosine coefficients describe the 1.15 cpy signal which is composed of the oceanic signal and the M2 tidal error. The second step partitions the 1.15 cpy signal into oceanic and tidal error components. This step relies on the assumption that both of the components of the 1.15 cpy signal have constant phases and amplitudes over a small region (a few degrees square) at a given time. This means that the sine and cosine

coefficients for the 1.15 cpy ocean signal are constant as are the sine and cosine coefficients of the aliased tide. Taking advantage of the spatial aliasing of the M2 tide, the 1.15 cpy signal is partitioned into its two components by minimizing

$$\sum_{i=1}^{N} \{c_i - O_c - [T_c \cos\Phi_i - T_s \sin\Phi_i]\}^2 + \{s_i - O_s - [T_c \sin\Phi_i + T_s \cos\Phi_i]\}^2 , \qquad (2.23)$$

where c_i and s_i are the cosine and sine coefficients of the 1.15 cpy composite signal at the ith normal point within the small region centered on normal point x_m, N is the number of normal points within the region, O_c and O_s are the cosine and sine coefficients of the oceanic signal in the region, T_c and T_s are the cosine and sine coefficients of the aliased tidal error, and Φ_i is the phase at the time the SSH was measured at the ith normal point. The terms in square brackets account for the different measured phases at each normal point. The phase of the tidal error is referenced to the phase of the 1.15 cpy signal.

SSHa, corrected for orbit error and M2 tidal error, is given by

$$\eta(x_m,t) = h''_n(x_m) - T_c(x_m) \cos(\omega t) - T_s(x_m) \sin(\omega t), \qquad (2.24)$$

where ω is the M2 tidal alias frequency, and t is the time relative to 1 Jan 1987. Following the application of environmental, orbital, and tidal alias corrections, the root mean square accuracy for SSHa is about 5 cm (Sailor and LeShack, 1987; Zlotnicki et al., 1989). The resulting time-space matrix of SSHa is the working data set upon which subsequent analysis is based.

Chapter 3 The Shedding of an Anticyclonic Eddy from the Alaskan Stream

Introduction

The most prominent members of the mesoscale eddy field are rings. Rings are formed when meanders in western boundary currents pinch off (Fugilister and Worthington, 1951). Their size and longevity make them important agents for the meridional transport of mass, heat and salt. They also may, at different times in their life history, be regions of enhanced or diminished biological productivity relative to the surrounding waters (e.g. Davis and Wiebe, 1985; Wiebe et al, 1985). As a consequence, an understanding of their structure, dynamics, and life history is necessary to assess their role in the circulation systems in which they reside.

This chapter presents observations of a meander which subsequently separates from the Alaskan Stream as an anticyclonic eddy or ring. The Alaskan Stream has, heretofore, been characterized as being an unusually stable western boundary current (Reed et al., 1991; Stabeno and Reed, 1991). Because the Alaskan Stream provides a significant inflow to the Bering Sea it will be suggested that the eddy influences circulation in the Bering Sea. This conjecture will be investigated further in the next chapter. Observations of the eddy were made by the GEOSAT altimeter during 1987 and 1988. The temporal evolution of the meander/eddy is described in terms of its trajectory, structure, vorticity, and energetics.

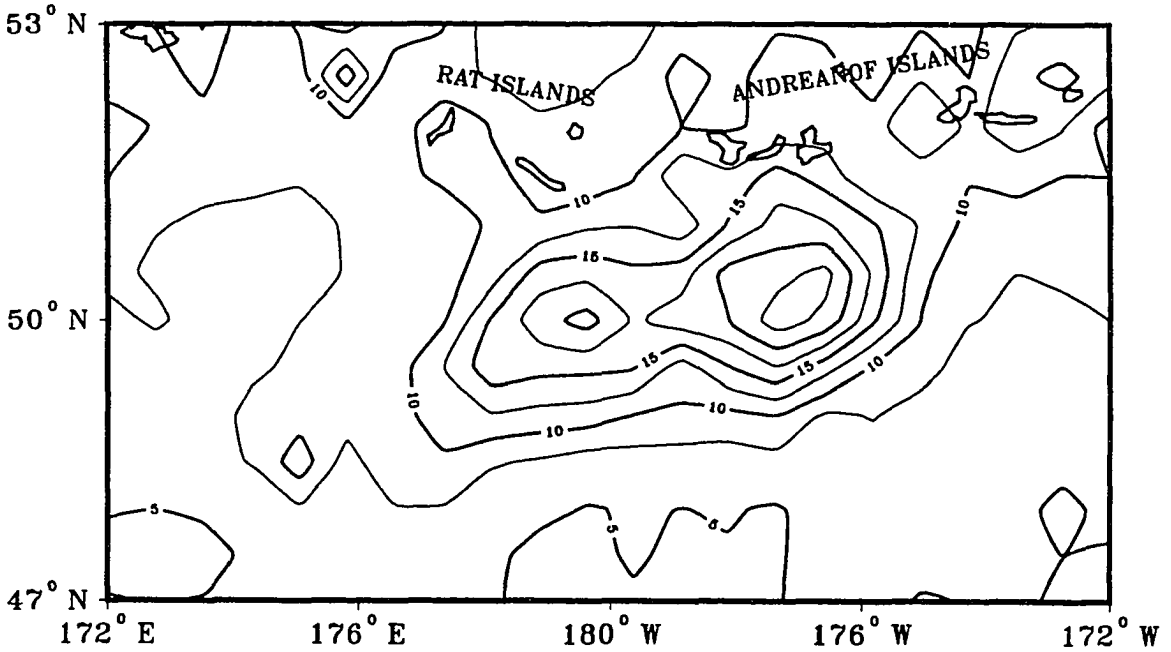

Figure 3.1 Root-mean-square SSH variability near the central Aleutian Islands for 1987-1988. The contour interval is 2.5 cm.

Section 3.1 Methods

A contour plot of the root-mean-square (rms) variability of SSH shows a region of high variability just south of the central Aleutian Islands (Figure 3.1). Contour plots of SSH anomalies for each ERM repeat cycle were generated. The plots showed an isolated, westward propagating, positive mesoscale anomaly in the same region. During the two years of observation, this SSH anomaly, interpreted to represent a meander or eddy, was the only significant, positive anomaly to transit the region.

A description of eddy structure and dynamics requires determining the location of its center of mass. The combined effects of relatively wide

ground track spacing (~105 km at 50 N) and missing data preclude using standard methods (Brown et al., 1983; Hooker and Olson, 1984) to estimate the center of the observed meander/eddy. The method used herein is a modification of the adjacent minor chord perpendicular bisector method (Hooker and Olson, 1984). The modified version requires that a minimum of two ground tracks intersect the meander/eddy. The locations of the even integer heights greater than 10 cm are linearly interpolated from the along track profiles of SSH. For any even integer height, the corresponding interpolated locations lie on that height contour. Adjacent locations on this contour delineate a set of triangles. A circle can be circumscribed around each triangle Each intersection of perpendicular bisectors of adjacent minor chords produces an estimate of the meander/eddy center. The overall center estimate (X_c, Y_c) is the mean of all the intersections (Xint,Yint) between adjacent perpendicular bisectors. That is,

$$X_c = \frac{1}{\sum_{j=1}^{N} w_j n_j} \sum_{j=1}^{N} w_j \sum_{i=1}^{n_j} Xint_{ij} \qquad (3.1)$$

$$Y_c = \frac{1}{\sum_{j=1}^{N} w_j n_j} \sum_{j=1}^{N} w_j \sum_{i=1}^{n_j} Yint_{ij} \qquad (3.2)$$

where n_j is the number of inscribed triangles constructed at height j. Repeating the computation of the center estimate for each repeat cycle of altimetric coverage yields the trajectory of the meander/eddy.

Both the meander and eddy were modeled as having an axially symmetric Gaussian profile

$$h = h_o \exp\left(-\frac{r^2}{r_o^2}\right) \tag{3.3}$$

where h is the sea surface displacement at radial distance r from the previously determined meander/eddy center. For each repeat cycle, measurements of SSH were fit in a least squares procedure to the logarithmic form of equation (3.3) to estimate the maximum sea surface displacement, h_o, and the e-folding radius, r_o.

The strength or circulation, Γ, of the eddy (vortex) was computed from the areal integral of its vorticity (Pedlosky, 1987)

$$\Gamma = \int \int_A \zeta \, dA \tag{3.4}$$

in which the relative vorticity, ζ, is given by

$$\zeta = \frac{v}{r} + \frac{\partial v}{\partial r} \tag{3.5}$$

where v is the azimuthal velocity at a radial distance r from the eddy center. The azimuthal velocity is computed from the gradient current balance

$$\frac{v^2}{r} + fv = g\frac{\partial h}{\partial r} \tag{3.6}$$

in which the Coriolis parameter, f, was fixed at its value for 49° N.

The available potential energy associated with the displacement of the sea surface (Gill, 1982) due to the eddy is

$$APE = \frac{1}{2}\rho_0 g \int \int_A h^2 dA \tag{3.7}$$

where ρ_0 is the basic state density (assumed to be 1.0 x 10^3 kg/m^3), g is gravitational acceleration, h is the meander/eddy height described by equation (3.3). The area of integration for equations (3.4) and (3.7) lies within a circle whose radius is $\sqrt{2}\ r_0$.

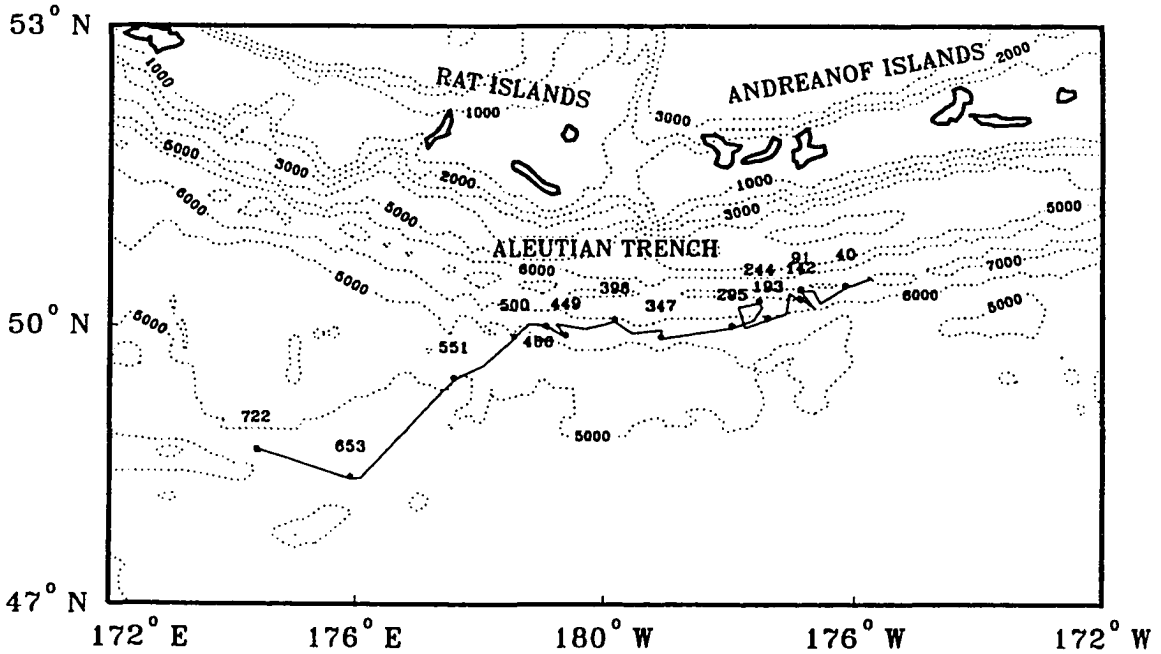

Figure 3.2 Trajectory of the meander/eddy center (solid line) as estimated from the modified perpendicular bisector method. The nominal time of observation (days since 1 Jan 87) is given for selected locations. The standard errors for individual center locations range from 15 km to 63 km. The bathymetry of the central Aleutian region is also shown (dotted lines).

Section 3.2 Results

The first repeat cycle for which there are sufficient measurements of SSH to estimate the center location is ERM 5. The nominal date of observation, taken to be the central date of the 17 day ERM repeat cycle, is 23 Jan 1987. The path of the meander/eddy center is shown in Figure 3.2. The center roughly follows the 6000 m isobath to 50°N, 179°E where its trajectory diverges from the Aleutian Trench and turns to the southwest on day 466. This occurs during ERM 31 for which the nominal date of

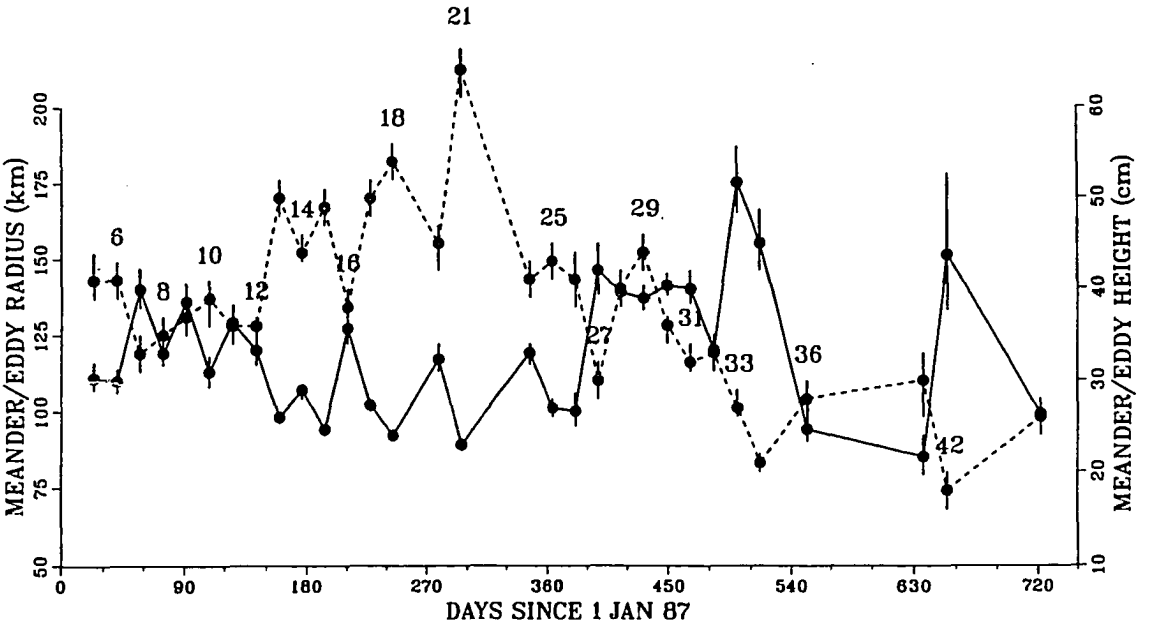

Figure 3.3 Time series of meander/eddy height (dashed line) and e-folding radius (solid line) computed from least squares fits of the SSHa data to an axially symmetric Gaussian profile. The ERM repeat cycle number is given for selected measurements. Error bars represent one standard deviation.

observation is 10 April 1988. Because an isolated anticyclonic eddy in the northern hemisphere propagates to the southwest (e.g. Firing and Beardsley, 1976) the closure of the meander and subsequent separation of the eddy from the Alaskan Stream are inferred to occur near this location and time. The last observation of the eddy puts the location of the estimated center to be near 48.6°N, 174.4°E for which the nominal date of observation is 20 Dec 1988.

The overall translation speeds for the meander and eddy, based upon the aforementioned separation criterion, are about 1.0 cm/sec and 1.5 cm/sec, respectively.

The sea surface displacement, h_0, of the meander/eddy generally increases until attaining a maximum during ERM 21, after which the displacement generally diminishes (Figure 3.3). In contrast, the e-folding radius exhibits a slight decreasing trend for most of the period of meander development (Figure 3.3). For the remainder of the record, except for a brief period (repeat cycles 27-31), the radius varies considerably. A comparison of the time evolution of the estimated e-folding radius to that of the sea surface displacement shows the two parameters to have a weak inverse relationship.

Figure 3.4 shows the evolution of the circulation as computed for the meander/eddy from the respective eddy profiles defined by the Gaussian parameters depicted in Figure 3.3. By making the simple assumption that the eddy spins down due to Ekman dynamics it follows that the circulation decays exponentially (Pedlosky, 1987). Assuming that the strength of the eddy will be greatest at the time of separation, Figure 3.4 indicates that the meander grows until the eddy is shed during ERM 21 (day 296, 22 Oct 1987). This date differs significantly from the estimate based on the path of the meander/eddy center.

The time series of available potential energy (Figure 3.5) provides a possible resolution of this discrepancy. The maximum APE occurs during ERM 29 (day 432, 6 March 1988). Assuming, also, that the APE associated with the eddy will be greatest at the time of separation, eddy separation

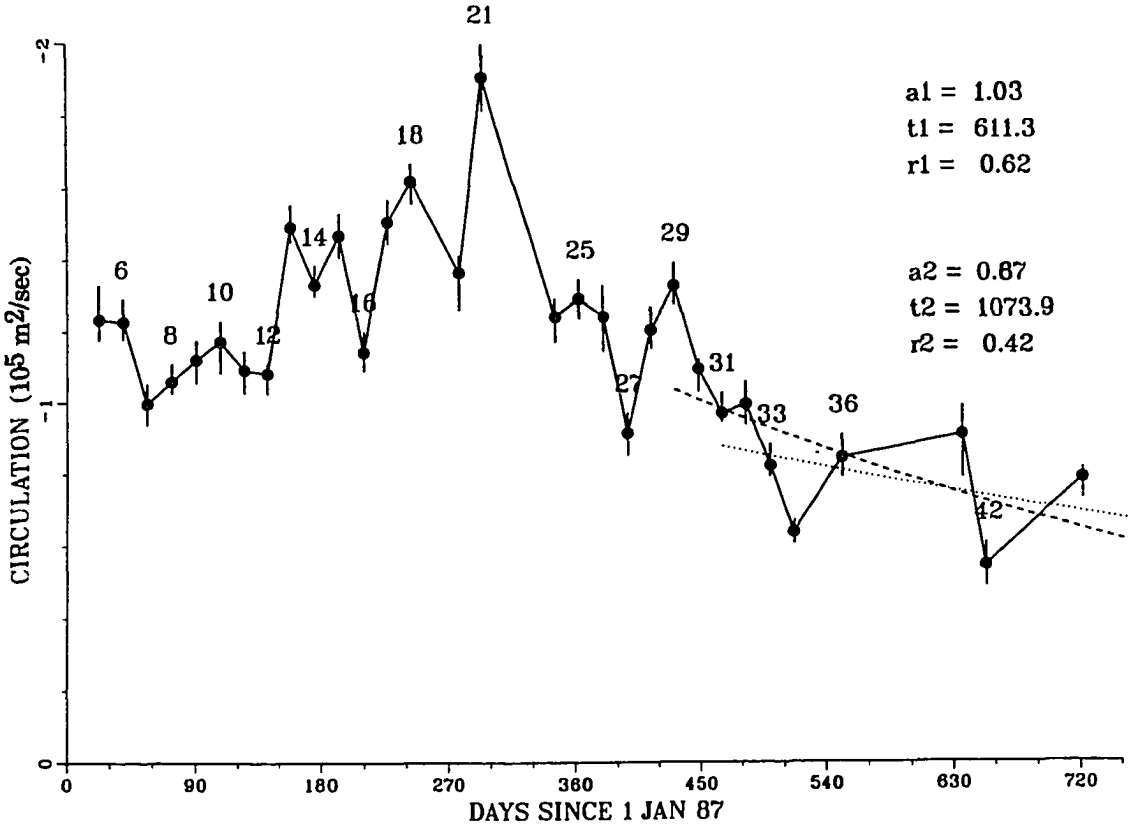

Figure 3.4 Time series of circulation (10^5 m^2 s^{-1}). The ERM repeat number is given for selected measurements. Error bars represent one standard deviation. The dashed and dotted curves show the least squares estimates of an exponential decay of circulation referenced to ERM 29 (day 432) and ERM 31 (day 466), respectively. The values for the initial circulation, a1 and a2, e-folding spin down time, t1 and t2, and correlation coefficient, r1 and r2, are given for the two curves.

occurs about a month earlier than that inferred from the meander/eddy trajectory. Returning to the plot of circulation (Figure 3.4), there is a local maximum at ERM 29. This date is more consistent with the estimates of

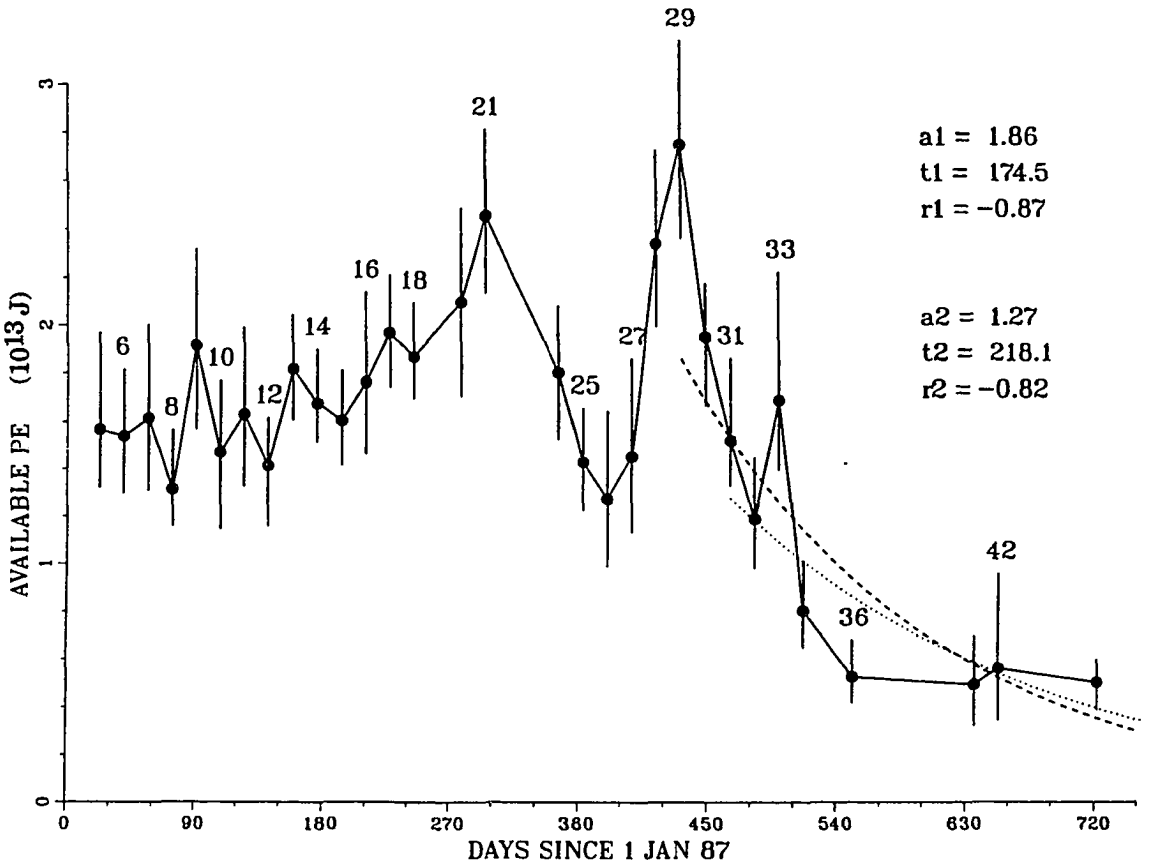

Figure 3.5 Time series of available potential energy (10^{13} J). The ERM repeat cycle number is given for selected measurements. Error bars represent one standard deviation. The dashed and dotted curves show the least squares estimates of an exponential decay of APE referenced to ERM 29 (day 432) and ERM 31 (day 466), respectively. The values for the initial APE, a1 and a2, e-folding spin down time, t1 and t2, and correlation coefficient, r1 and r2, are given for the two curves.

separation date deduced from the plots of the meander/eddy center and circulation.

Performing least squares fits of the post separation measurements of circulation to an exponential decay function, time referenced to days 432

and 466, the respective e-folding spin down times of 612 days and 1079 days are obtained. Least squares fits of the post separation available potential energies to the exponential decay function, also time referenced to days 432 and 466, yield e-folding spin down times of 174 days and 218 days, respectively.

Section 3.3 Discussion

The shedding of eddies from the Alaskan Stream was first proposed by Thomson (1972). Steady, barotropic frictional theory was invoked to show that, where the Alaskan Stream becomes approximately zonal in the vicinity of the central Aleutian Islands, the upstream vorticity balance between negative vorticity imparted by lateral friction and positive vorticity resulting from the combined contributions of wind stress curl and changing planetary vorticity, breaks down without an external source of positive relative vorticity. According to this argument, the Alaskan Stream becomes unstable and either separates from the northern boundary or reestablishes stability by shedding the excess negative vorticity in the form of anticyclonic eddies.

Despite the limited spatial coverage of the meander/eddy afforded by the GEOSAT altimeter, the region of instability and eddy separation, indicated by the meander center trajectory, agrees with that predicted by Thomson (1972). Representative estimates of eddy height, O(40 cm), diameter, O(300 km), and azimuthal velocity, O(30 cm/sec), obtained using the Gaussian model are within the range of values reported for anticyclonic rings spawned by other current systems (e.g. Olson et al., 1985; Andrews, 1983; Lutjeharms and Valentine, 1988).

The dates of occurrence of meander growth, eddy separation and decay deduced from the time series of circulation and available potential energy are in reasonable agreement with those inferred from the center trajectory. Comparison of the eddy decay time scales obtained from these

two time series indicate that the eddy is largely able to maintain its integrity (vorticity) as it loses mass through frictional decay. This is a characteristic of both warm-core (Olson et al., 1985) and cold-core (Olson, 1980) Gulf Stream rings.

While there is no direct evidence to suggest that the Alaskan Stream eddy is a ring, it is dynamically similar to warm-core rings found in other current systems. Hydrographic measurements are obviously required to make such a determination.

The observed occurrence of eddy shedding from the Alaskan Stream has many possible implications. Depending on the timing of the growth of the meander migratory routes of fish stocks might be altered. As mentioned earlier, the biological environment of the ring may be significantly different than the surrounding waters through which it migrates. The physical/biological front may be a locus for the aggregation of both producers and consumers. Because the Alaskan Stream represents the largest source for transport into the Bering Sea (Favorite, 1974), eddy development and subsequent shedding might modulate the circulation of the Bering Sea.

At the time of separation the eddy has a diameter of about 300 km. If this eddy is a ring, the volume of the ring portion of this eddy (100 km ring width, 1500 m depth) is 9.4×10^{13} m^3. Compared to the mean transport of 14 Sv (annual transport = 4.4×10^{14} m^3) into the Bering Sea east of the Komandorskii Islands (Favorite, 1974), the ring volume represents a transport anomaly of 21%. Associated with this transport anomaly are the

corresponding heat and salt anomalies which may also affect Bering Sea circulation.

Chapter 4 Circulation Variability in the Bering Sea

Introduction

The Bering Sea is a semi-enclosed sea bounded by Siberia to the north and west, continental Alaska to the east, and the Aleutian-Komandorskii island arc to the south. At its north end it is connected to the Arctic Ocean through the narrow (85 km) and shallow (50 m) Bering Strait. It is connected to the North Pacific through the numerous passes in the island arc. Bering Sea waters cover an area of 2.3×10^6 km^2 and occupy a volume of 3.7×10^6 km^3. In size it ranks second only to the Mediterranean Sea among the semi-enclosed seas of the world ocean. A continental shelf underlies 44 percent of the Bering Sea; principally as a broad (~ 500 km), flat, and shallow (~ 170 m at the shelf break) expanse in the northeastern half of the sea. The deep basin (maximum depth ~ 3800 m) occupies the southwestern half of the sea and covers 43 percent of the area. The remaining area is continental slope. Shirshov Ridge and Bowers Ridge partition the abyssal Bering Sea into three smaller basins, the Kamchatka, Bowers, and Aleutian Basins, of which the Aleutian Basin is the largest (Figure 4.1).

Most of the previously published circulation schemes suggest that the water from the Alaskan Stream enters the Bering Sea through the passes of the Aleutian-Komandorskii island arc. Of the 39 passes identified by Favorite (1967), only 14 passes have a cross sectional area greater than 1 km^2 or a sill depth exceeding 200 m. Arsen'ev (1967) identified the east side

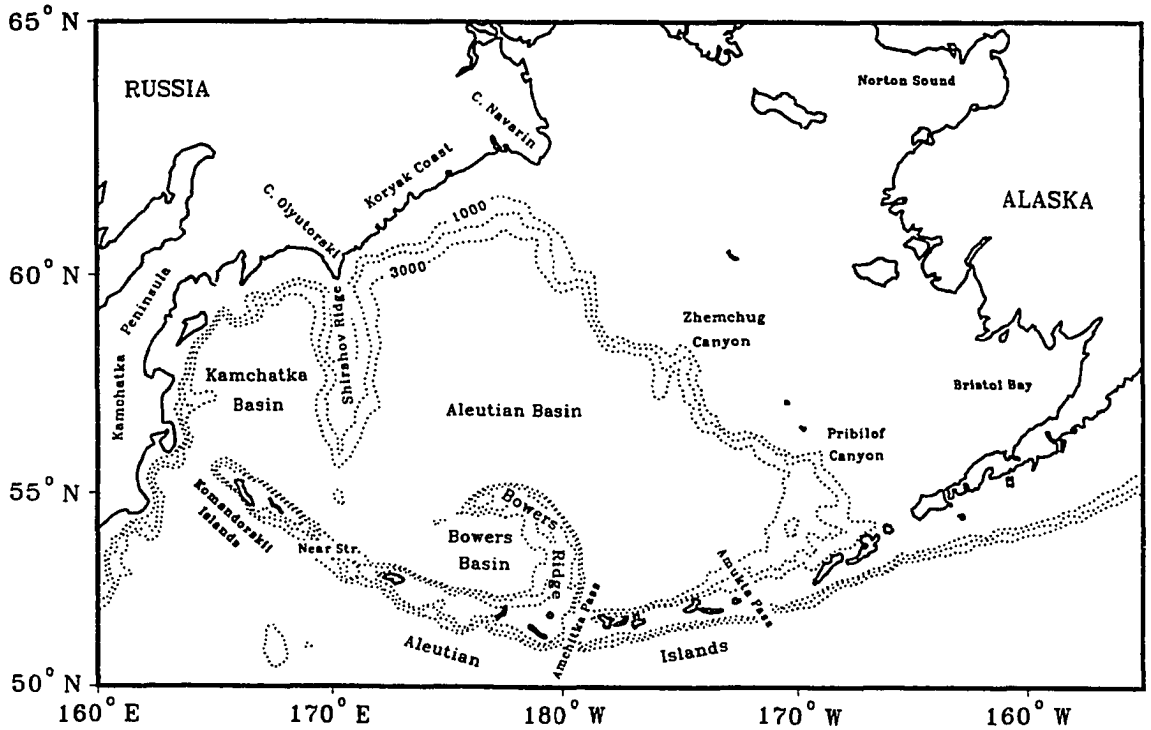

Figure 4.1 Bathymetry of the Bering Sea Basin and geographic names.

of Near Strait as the principal conduit through which flow from the North Pacific enters the Bering Sea. Much of this inflow is thought to recirculate within the Kamchatka Basin and to later exit through Kamchatka Strait and through the west side of Near Strait. Comparative budgets of flow through the passes are given in Tables 4.1 and 4.2. Waters in the southeast Aleutian Basin feed a northwestward flowing 'transverse current' (Dobrovol'skii and Arsen'ev 1959) which lies adjacent to the eastern continental shelf. This current was given the name Bering Slope Current by Kinder et al. (1975). They estimated the mean transport of the current to be about 5 Sv and offered two different descriptions of the current; water mass analyses indicated a three banded current system whereas the

Table 4.1 Flow (Sv) through the passes of the Aleutian-Komandorskii island arc according to Arsen'ev (1967) (from Favorite, 1974).

Pass	Transport out	Transport in
Kamchatka	21.0[1]	2.6[2]
Near		14.4
West Aleutian group[4]		0.7
Central Aleutian group[5]		4.4
Total	21.0	22.1[3]

[1] Above 3000 m
[2] Below 3000 m
[3] Loss through Bering Strait - 1.1 Sv
[4] Kiska, Buldir, and Semichi Passes
[5] Tanaga and Amchitka Passes

Table 4.2 Flow (Sv) through the passes of the Aleutian-Komandorskii island arc, summer/winter (Hughes et al., 1974).

Pass	Transport out	Transport in
Kamchatka	20/35	
Near		25/25
Buldir and Kiska	5/	
Central & eastern Aleutian		/10 (including Buldir and Kiska)

dynamic topographies indicated a system of eddies. Tidal currents dominate the flow on the outer continental shelf adjacent to the Bering Slope Current although the mean flow over the outer shelf is also to the

northwest at 5-15 cm s-1 (Kinder and Schumacher, 1981a,b). A branch of the Bering Slope Current crosses the shelf break near Cape Navarin and is identified as the primary source for the outflow through the Bering Strait to the Arctic Ocean (Kinder et al., 1986; Overland and Roach, 1987). The southwestward flowing branch, the East Kamchatka Current, continues as a western boundary current along the Koryak and Kamchatka coasts to exit the Bering Sea through Kamchatka Strait (Ratmanov 1937) and the western portion of Near Strait (Dobrovol'skii and Arsen'ev 1959). The resulting large scale circulation in the deep basin is ascertained to be cyclonic, more confidently so in the western half of the sea. The locations and persistence of the numerous eddies which populate many of the aforementioned circulation schemes have not been discussed because they are scheme dependent, subject to the sampling limitations alluded to above. This aspect of the Bering Sea circulation will be addressed in a later section.

Section 4.1 Sea surface height variability

Wyrtki et al. (1976) observed that eddy activity in the ocean is associated with the sheared flows characteristic of most ocean currents. Using an altimeter to measure the temporally and spatially varying topographic signatures of this eddy activity (discussed in Chapter 2) is, therefore, an excellent method by which to monitor the strength and location of ocean currents. This method has been used by a number of researchers to study the current regimes in many different regions of the

world ocean (e.g. Cheney et al., 1983, global circulation; Douglas and Cheney, 1981, western North Atlantic and Gulf Stream; Thompson et al., 1983, Gulf of Mexico; Wakker et al., 1990, Agulhas Current; White et al., 1990, California Current; Chelton et al., 1990, Southern Ocean). Similarly, this method is used herein to provide an initial, altimetric perspective of circulation in the Bering Sea.

The two year (1987-1988) root-mean-square (RMS) SSH variability was computed at each normal point along all ascending and descending orbital ground tracks within the study domain. The computed values at all normal points were interpolated to a grid spaced 0.75° in longitude and 0.5° in latitude and then contoured (Figure 4.2). In considering the plot of SSH variability for the Bering Sea region, it is appropriate to first look outside the Bering Sea at the variability signature of the Alaskan Stream because this current is the principal source for transport into the Bering Sea (Favorite, 1974). The presence of the Alaskan Stream is indicated by the band of moderate (8 cm - 10 cm) to high variability (> 10 cm) occurring along the south side of the Alaska Peninsula and Aleutian-Komandorskii island arc and extending westward out to about 170°E. The localized region of high variability south of Amchitka Pass near 180° was shown in the previous chapter to be the signature of a meander in the Alaskan Stream which subsequently separates from the stream as an eddy.

On the north side of the island arc there are two northward protruding fingers of moderate variability which suggest continuity of flow with Alaskan Stream. The first protrusion extends northward along the eastern flank of Bowers Ridge. The principal pass near this location is

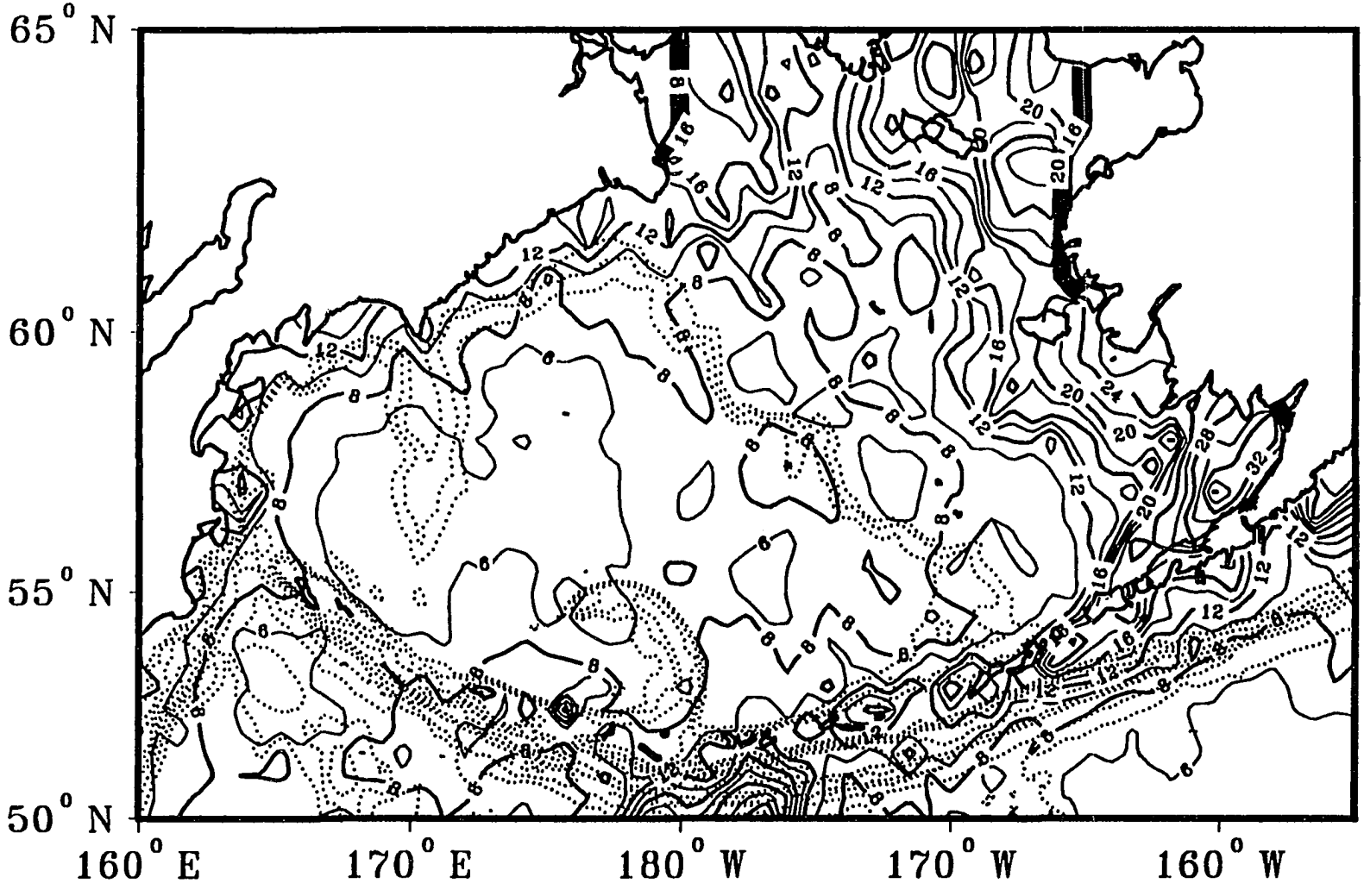

Figure 4.2 Two year (1987-1988) root-mean-square SSH variability (cm) in the Bering Sea. Bathymetric contours are shown as dotted lines at intervals of 1000 m.

Amchitka Pass. The second protrusion, exhibiting somewhat less variability than the first, extends northward from the eastern side of Near Strait into the large region of low variability (< 6 cm) which lies over much of the western half of the deep basin. Because the SSH variability on the Bering Sea side of Amchitka Pass suggests a more strongly sheared flow than through Near Strait it might be reasonable to infer that greater transport into the Bering Sea occurs through the former pass. However, it is generally accepted that the greatest transport into the Bering Sea occurs through Near Strait (e.g. Arsen'ev, 1967; Favorite, 1974). Two possible resolutions of the apparent contradiction are offered. The cross sectional area of Near Strait is more than five times that of Amchitka Pass (Favorite, 1974). As a consequence, a large transport through Near Strait can be supported by a relatively slowly moving (varying) current. This interpretation is supported by Natarov (1963) and Hughes et al. (1974) who have reported that there is little variation in the flow through Near Strait. An alternative resolution is that eastern flank of Bowers Ridge can act, in the manner like the western boundary of an ocean basin, as a sink for quasigeostrophic energy, the manifestation of which would be a time varying eddy field (Rhines, 1969). Consequently, the locally elevated SSH variability may reflect more the presence of a western boundary current along the eastern side of Bowers Ridge than a substantial flow through Amchitka Pass.

A third finger protrudes northward from the eastern Aleutian Islands near 174°W. Its proximity to Seguam Pass and Amukta Pass and greater SSH variability *vis a vis* the previously discussed protrusions may

be interpreted to indicate substantial flow from the Alaskan Stream into the southern Aleutian Basin through these passes. However, the small cross sectional areas of these two passes, 2.1 km^2 and 19.3 km^2 respectively (Favorite, 1974), argue against such an interpretation. A time series of SSH anomaly profiles along ascending ground track A147, which traverses the protrusion, reveals the presence of significant SSH anomalies during ERMs 5 to 11 at about 53°N and during most of ERMs 26 to 33 at about 53.5°N to 54°N suggestive of eddy-like features (Figure 4.3). Although not apparent from the bathymetric contours in Figure 4.1, a chart of the region (NOAA 513) shows a submarine canyon (Amilia Canyon) and knoll (Amilia Knoll) interrupting the generally smooth bathymetric contours west of this location. Wave scattering is a mechanism which may explain the locally elevated SSH variability. Planetary waves can be scattered by topographic features for which the radius of curvature is less than or equal to the wavelength of the incident wave (LeBlond and Mysak, 1978). While there is no evidence that planetary waves are incident upon the knoll and canyon, the knoll is a prominent topographic feature with a radius of curvature less than the wavelength of the eddy-like features observed in Figure 4.3.

The most striking aspect of the pattern of SSH variability over the deep basin of the Bering Sea is its relationship to the bathymetry. In general, regions exhibiting moderate and high SSH variability overlay or are adjacent to steep bathymetric slopes associated with the margins of the deep basin and the two ridges which partition it. At large scales, the sea surface over the deep basin east of 180°E exhibits slightly more variability

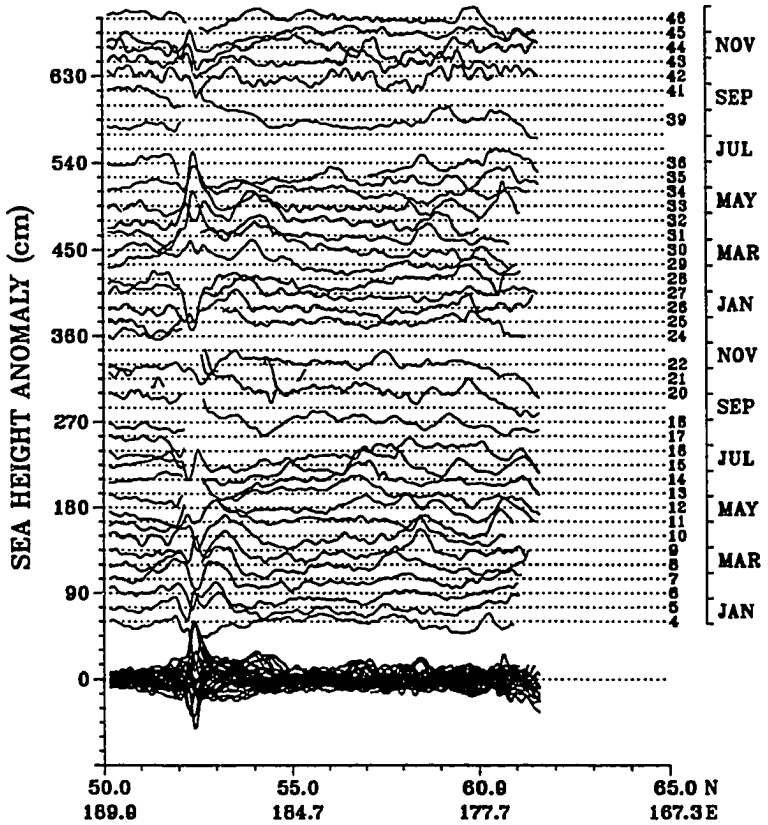

Figure 4.3 Two year time series of SSH anomaly profiles along ascending ground track A147. Successive profiles are displaced 15 cm.

than west of this meridian. In contrast, the greatest variability occurs along the Koryak and Kamchatka coasts from Cape Navarin to beyond Cape Africa. This band of moderate to high variability is the signature of the southwestward flowing western boundary current of the basin, the East Kamchatka Current. Two fingers of moderate variability protrude from this current. One extends southeastward across Kamchatka Strait.

This extension is interpreted to indicate a recirculation of some of the East Kamchatka Current within the deep basin. A second finger near Cape Olyutorski extends southward along the eastern flank of Shirshov Ridge into the large region of low variability overlaying the western deep basin. As was suggested for the observed locally elevated SSH variability along the eastern side of Bowers Ridge, this particular finger of variability may also reflect the presence of a western boundary-like current along the eastern flank of Shirshov Ridge.

The location of the Bering Slope Current corresponds to the punctuated band of moderate variability enclosed by the 8 cm contour, the axis of which extends across the central Bering Sea with a southeast-northwest orientation. The region of greatest variability associated with the Bering Slope Current is centered on the western wall of Zhemchug Canyon with the downstream portion of the current exhibiting slightly more variability than the upstream half.

It is inferred from the contrast between the high variability observed over the outer shelf just south of Cape Navarin and the low variability over the central outer shelf in the vicinity of Zhemchug Canyon that most of the flow that crosses the shelf break in the central Bering Sea does so near Cape Navarin so as to feed a western boundary current which flows northward along the Siberian coast (Kinder et al., 1986).

The very high SSH variability observed over the eastern shelf along the Alaska coast from Bristol Bay to Norton Sound and over the western shelf north of Cape Navarin is likely uncorrected tidal error. Accordingly, inferences about circulation and its variability over most of the continental

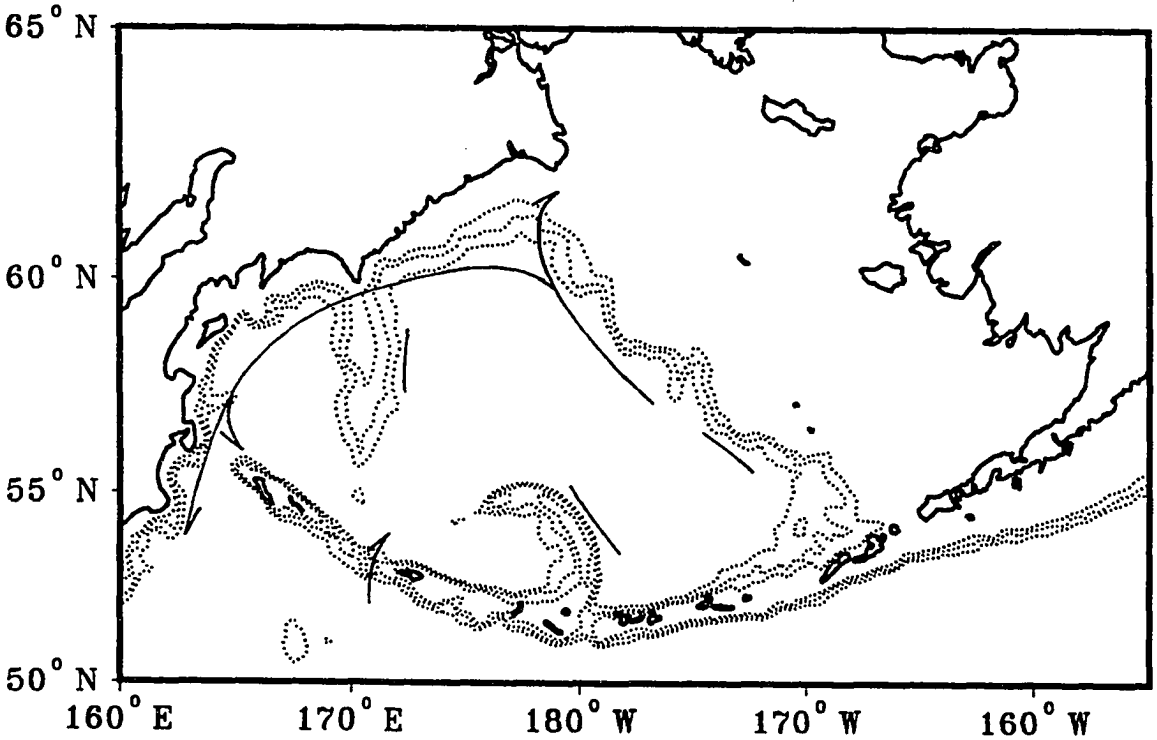

Figure 4.4 Bering Sea Basin circulation components inferred from SSH variability.

shelf of the Bering Sea cannot be made with confidence and are not presented as part of this study.

Assuming that the regions of moderate to high variability in Figure 4.2 are associated with significant currents in the deep basin, and by adhering to the convention that the large scale circulation is cyclonic, the first components of a circulation model for the deep basin of the Bering Sea, based primarily on altimeter data, are presented in Figure 4.4. The East Kamchatka Current and Bering Slope Current are shown, although the latter is depicted as being discontinuous. Some recirculation of the East Kamchatka Current occurs along the north side of Komandorskii Island.

Inflow to the Bering Sea is shown to be through Near Strait. Currents are indicated for the eastern flanks of Shirshov Ridge and Bowers Ridge although the direction of the flow is not yet specified. An empirical orthogonal function analysis is applied to the altimeter data in the next section of this chapter to refine the circulation model.

Section 4.2 Empirical orthogonal function analysis of sea surface height variability

The temporal and spatial variability of SSH in the Bering Sea is investigated using an empirical orthogonal function (EOF) analysis. The utility of an EOF analysis performed on (typically noisy) geophysical data is that it serves to partition the data into modes of variability, the first few of which often allow for some physical interpretation. Oceanographic field variables subjected to EOF analysis include sea surface temperature (e.g. Weare et al., 1976), pycnocline depth (e.g. White and Tabata, 1987), and sea surface height anomalies (e.g. Chelton et al., 1990).

Each mode of variability is described by a standing wave pattern (eigenvector), a time amplitude function (TAF) which modulates the eigenvector, and an eigenvalue, which divided by the sum of all eigenvalues represents the fraction of the total variance explained by that mode. For a given mode, the time varying amplitude at a specific location is recovered by taking the product of the appropriate TAF and eigenvector element corresponding to the specified location.

A statistical noise level is established according to a method described by Overland and Priesendorfer (1982). The noise level is a fractional variance threshold derived from EOF analyses of randomly drawn data sets. Each EOF mode obtained from an analysis of observational data must explain a fraction of the total variance in excess of the noise level to be statistically significant.

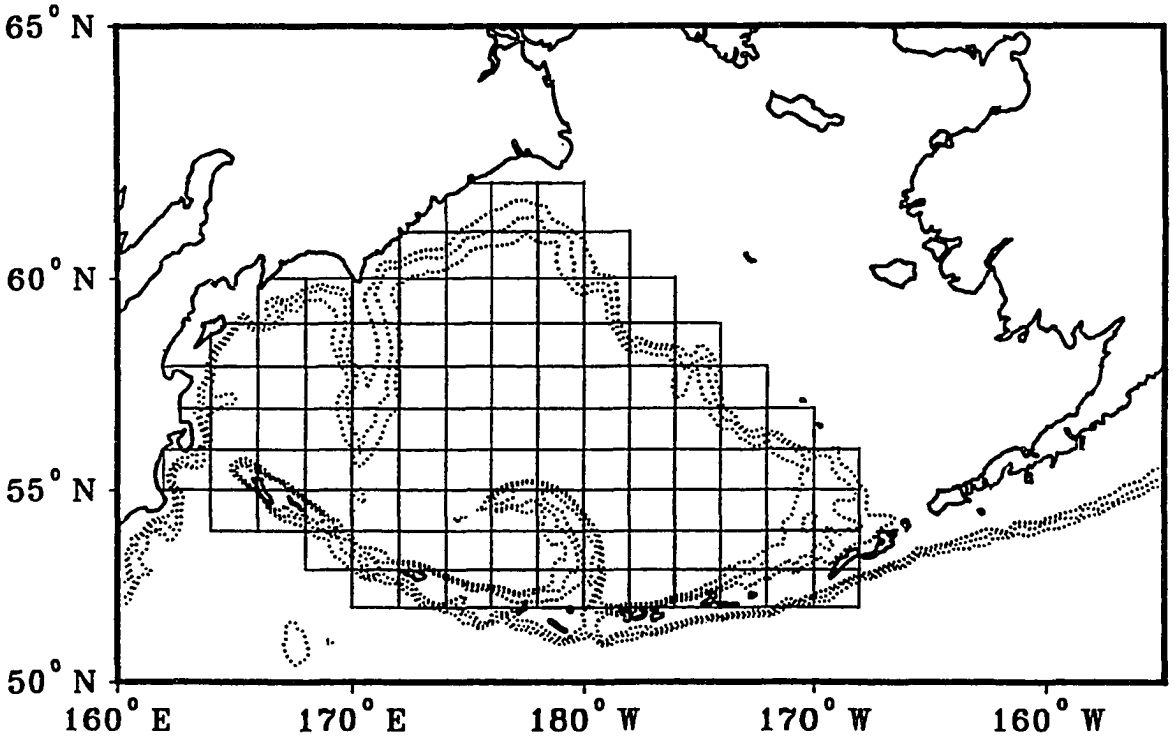

Figure 4.5 Locations of the 107 2.0° longitude x 1.0° latitude grid cells.

Due to decreasing numbers of altimetric measurements made over the Bering Sea during 1987 and 1988 (see Zlotnicki et al., 1990) it was necessary to average the SSHa data in space-time bins in order to produce continuous time series of SSH anomalies for each of 107 regularly spaced 2.0° longitude x 1.0° latitude grid cells overlying the deep basin of the Bering Sea and its margins (Figure 4.5). The dimensions of each bin were 2.0° longitude x 1.0° latitude x 3 months. This resulted in the time series of average SSHa for each grid cell being represented by a three month running mean of ascending and descending track measurements of SSHa acquired within that grid cell. The rather coarse bin dimensions were necessary to ensure

Table 4.3 Variance explained by the first six EOF modes of SSHa in the Bering Sea. Cumulative variances may not agree with the sum of the individual variances due to round off errors. (107 grid cells).

Mode	1	2	3	4	5	6
Variance explained (%)	24.3	19.5	12.7	10.4	9.1	7.3
Cumulative variance (%)	24.3	43.7	56.4	66.8	75.9	83.2

at least one SSHa measurement was acquired by the altimeter in each space-time bin. The EOF analysis was performed on the resulting space-time (107 locations x 22 three month running means) matrix of the averaged SSH anomalies. The severe temporal and spatial averaging restricts this EOF analysis to long period (≥ 6months), long wavelength (≥ 220km) SSH anomalies.

The first six EOF modes which cumulatively explain 83.2% of the variance in SSHa (Table 4.3) are above the statistical noise level according to Overland and Preisendorfer (1982). However, discussion will be confined to the first three modes because they represent lower frequency variability than do the higher modes.

Mode 1 In general, SSH displacements along and above the margins of the three basins in the deep Bering Sea are out of phase with SSH displacements in the interiors of the basins (Figure 4.6). The greatest SSH variability is found along the Koryak coast southwest of Cape Navarin. A secondary maximum in SSH variability occurs along the Kamchatka Peninsula centered near Kamchatka Strait. The TAF indicates that the

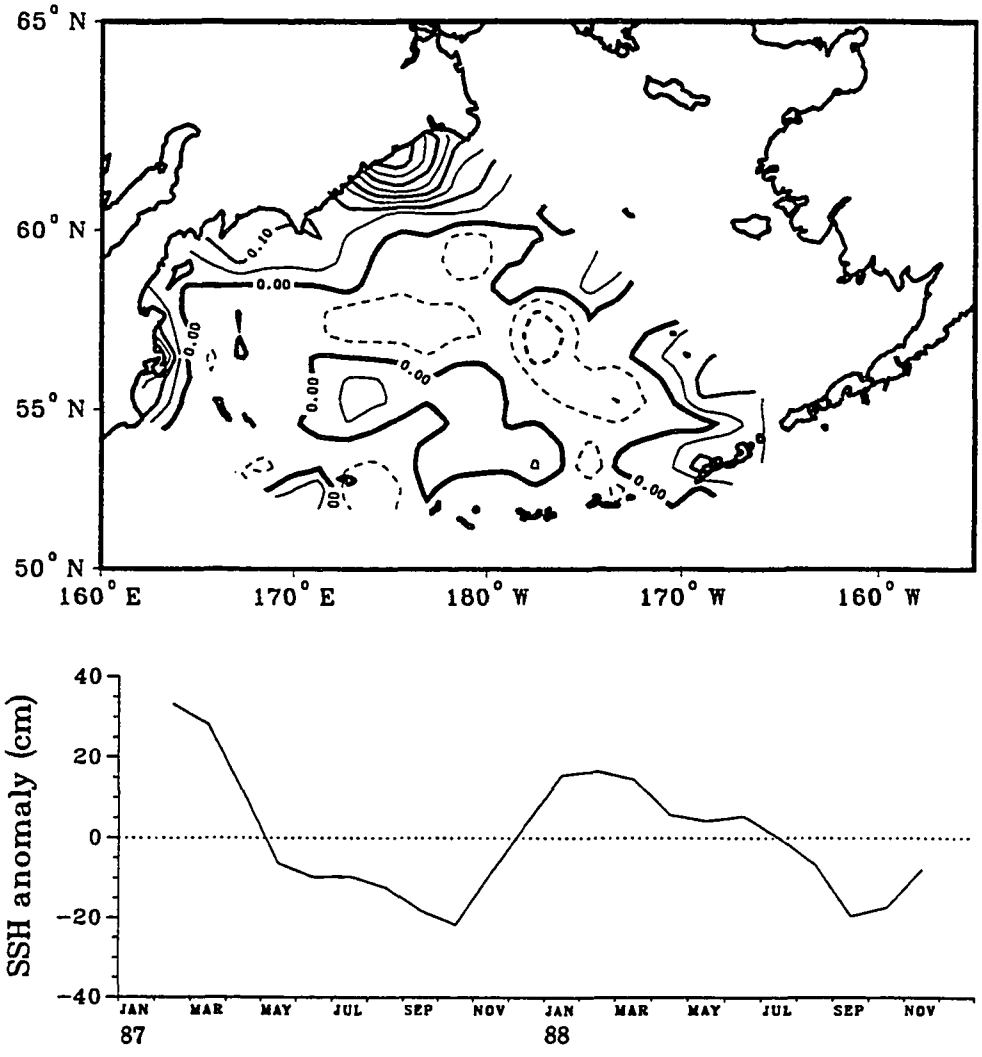

Figure 4.6 The eigenvector and time amplitude function for the first EOF mode. The contour interval is 0.05.

eigenvector pattern undergoes a strong annual period fluctuation.

Considered within the context of a mean cyclonic circulation in the deep Bering Sea, the TAF and SSH displacement along the basin margins relative to the displacement in the interior suggests that winter circulation

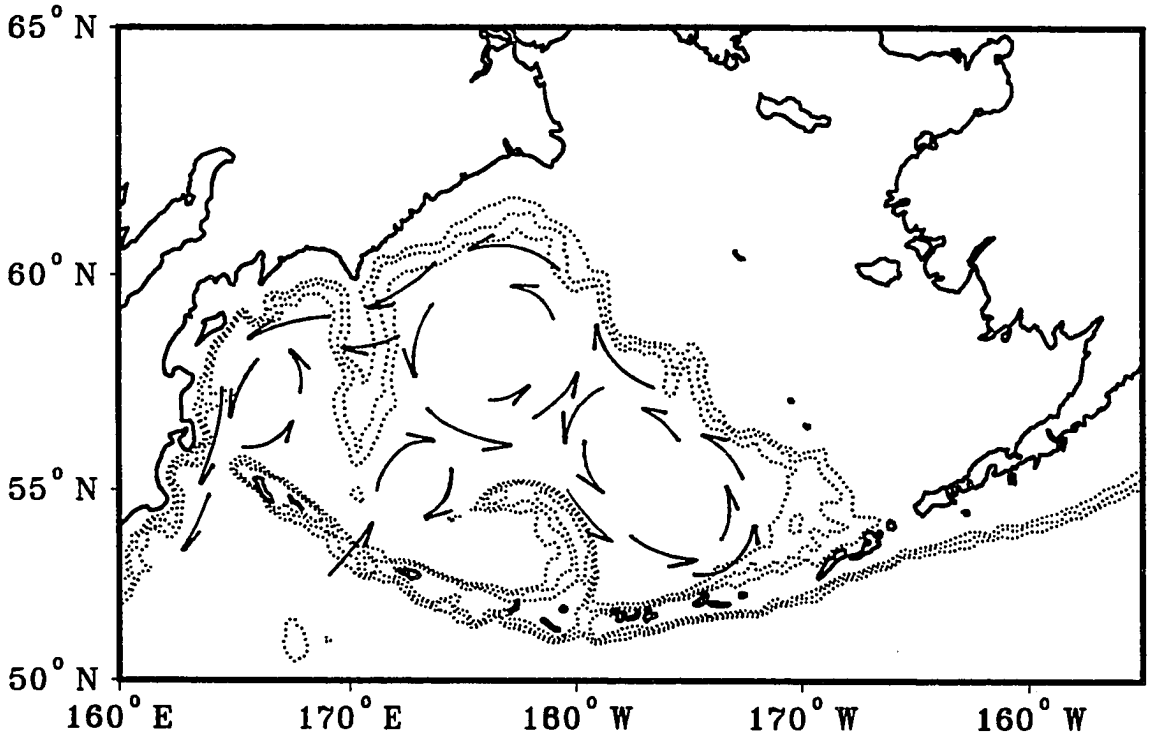

Figure 4.7 The winter surface circulation inferred from the first mode eigenvector pattern.

is strongly cyclonic and that flow largely follows the bathymetry. The two local maxima in SSH variability along the western boundary are interpreted to suggest that the overall, winter circulation derives from cyclonic gyres in the Aleutian and Kamchatka Basins (Figure 4.7). This circulation model implies that the East Kamchatka Current has a maximum southward transport during the winter and a minimum southward transport in the fall. This qualitatively agrees with seasonal baroclinic transport estimates of Reid (1973) and Hughes et al. (1974). Reid (1973) attributes the seasonality of the transport to the large annual signal in wind forcing over the region.

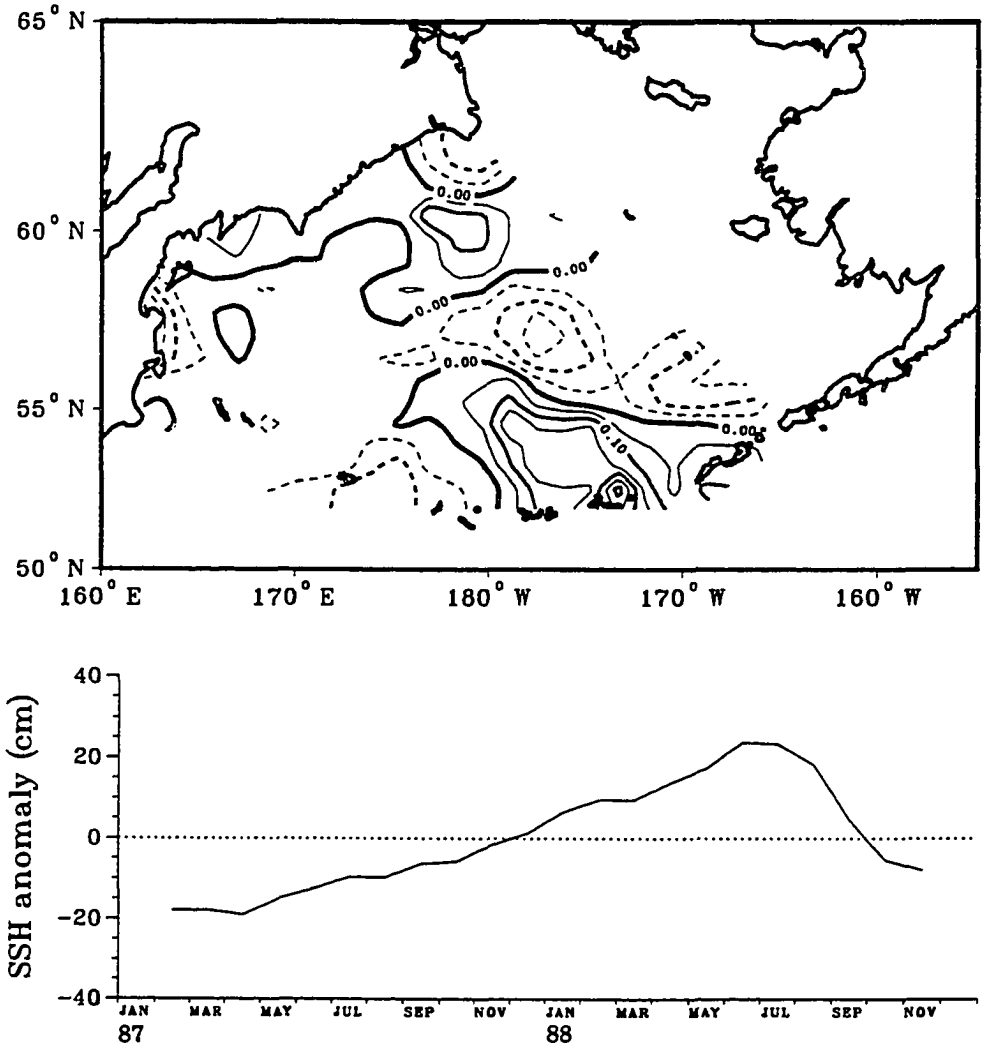

Figure 4.8 The eigenvector pattern and time amplitude function for the second EOF mode. The contour interval is 0.05.

As noted above, this mode is characterized by an annual signal which is approximately the alias period (317 days) for SSH errors associated with the Schwiderski (1980) model ocean tide correction for the M_2 tidal constituent (Cartwright and Ray, 1990). It is believed however,

that this mode depicts primarily non-tidal behavior owing to the alias correction applied (Jacobs et al., 1992) and because the length scales associated with the spatial pattern of this eigenvector do not correspond to the wavelength of the tidal alias error (7.6° of longitude, Cartwright and Ray, 1990).

Mode 2 Figure 4.8 shows that the greatest variability for this mode occurs in the Kamchatka and Aleutian Basins. The nodes of the eigenvector pattern partition the Aleutian Basin into three principal regions of variability which are suggestive of gyre-like or meander-like circulation features. The amplitude of these features diminishes from south to north. SSH anomalies in the Bowers Basin and the western Kamchatka Basin fluctuate in phase with the gyre-like anomaly in the central Aleutian Basin. The eigenvector pattern implies that when flow onto the shelf south of Cape Navarin is strong, cyclonic circulation in the Kamchatka Basin is anomalously weak. In addition to that occuring through Kamchatka Strait, flow between the North Pacific and Bering Sea appears to occur through Amchitka Pass and Amukta Pass. The TAF indicates interannual periodicity for this mode.

Mode 3 Figure 4.9 shows the eigenvector pattern, although somewhat more complex, is similar to the eigenvector pattern of the previous mode. Gyre-like features occupy the Aleutian Basin, but are displaced to the west of the locations of mode 2 features. The greatest amplitudes are associated with those features in the central Aleutian Basin. The displacement of anomalies in Bowers Basin and Kamchatka Basin are in phase with the gyre-like feature in the central Aleutian Basin, as was the case for the

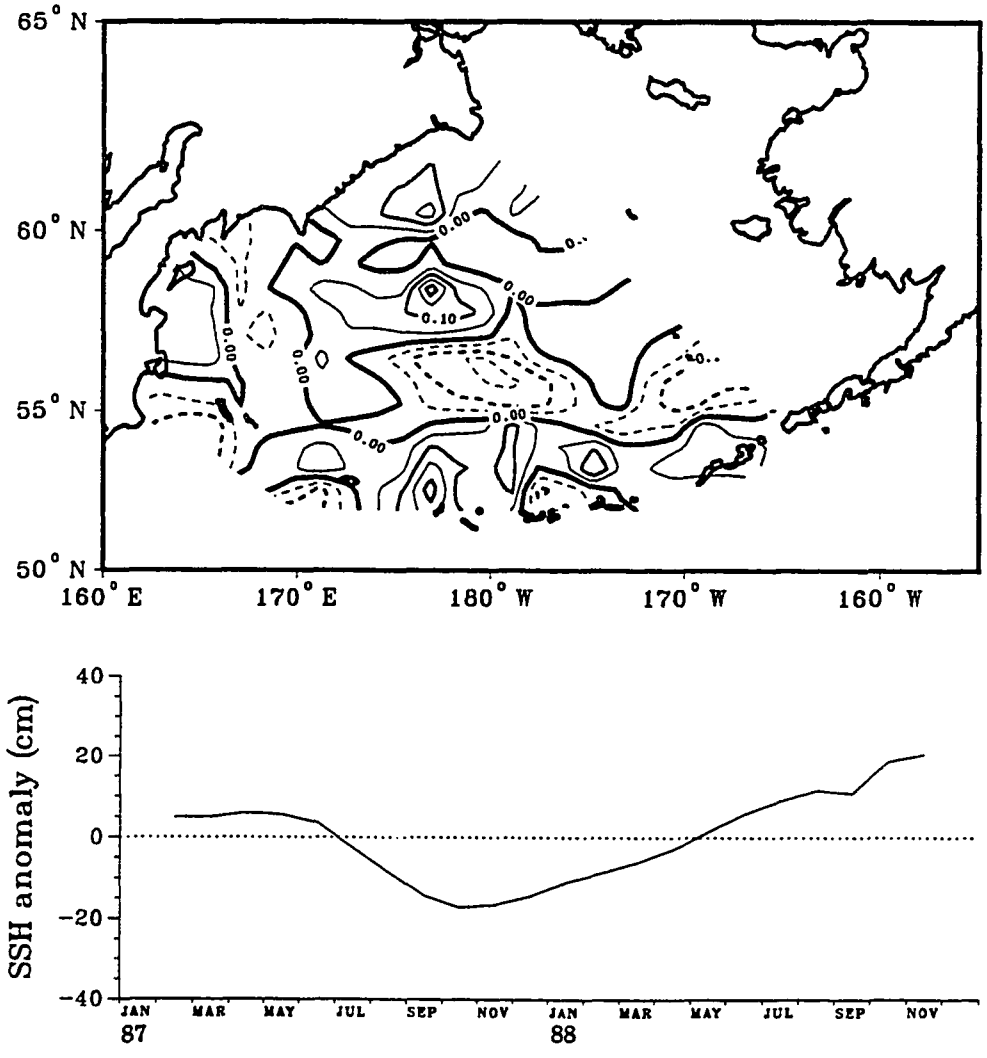

Figure 4.9 The eigenvector pattern and time amplitude function for the third EOF mode. The contour interval is 0.05.

previous mode. The Kamchatka anomaly extends further eastward than it did in the previous mode so that anomalous flow through Kamchatka Strait is inferred to be weaker than that described by mode 2. Flows

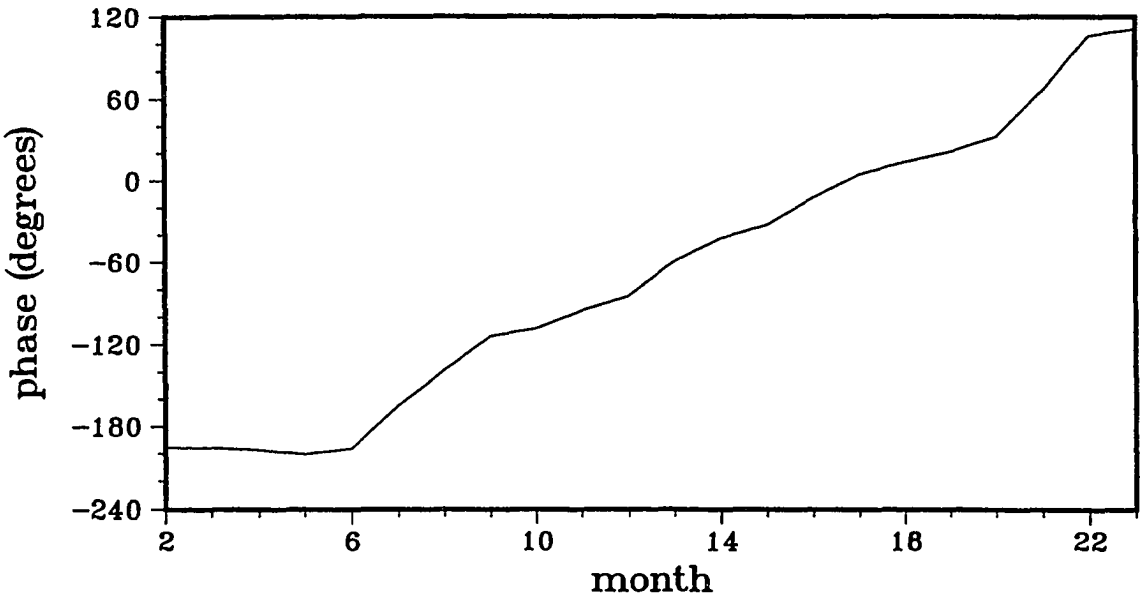

Figure 4.10 Phase of the combined mode 2 and mode 3 SSHa field.

through Near Strait, Buldir Pass, and Amchitka Pass are also inferrred. The TAF indicates this mode also fluctuates interannually.

Although their associated variances are somewhat different, the second and third modes are characterized by similar spatial patterns modulated by greater than annual period signals. As a result, these modes are interpreted to represent components of the same (or very similar) statistical process(es). Assuming that similar statistical processes reflect similar physical processes, these two modes are collectively interpreted as describing the westward propagation of low frequency features across the Aleutian Basin.

Figure 4.10 shows the phase, φ, of the SSH anomaly field associated with the combined second and third modes. Phase was computed from the respective time amplitude functions

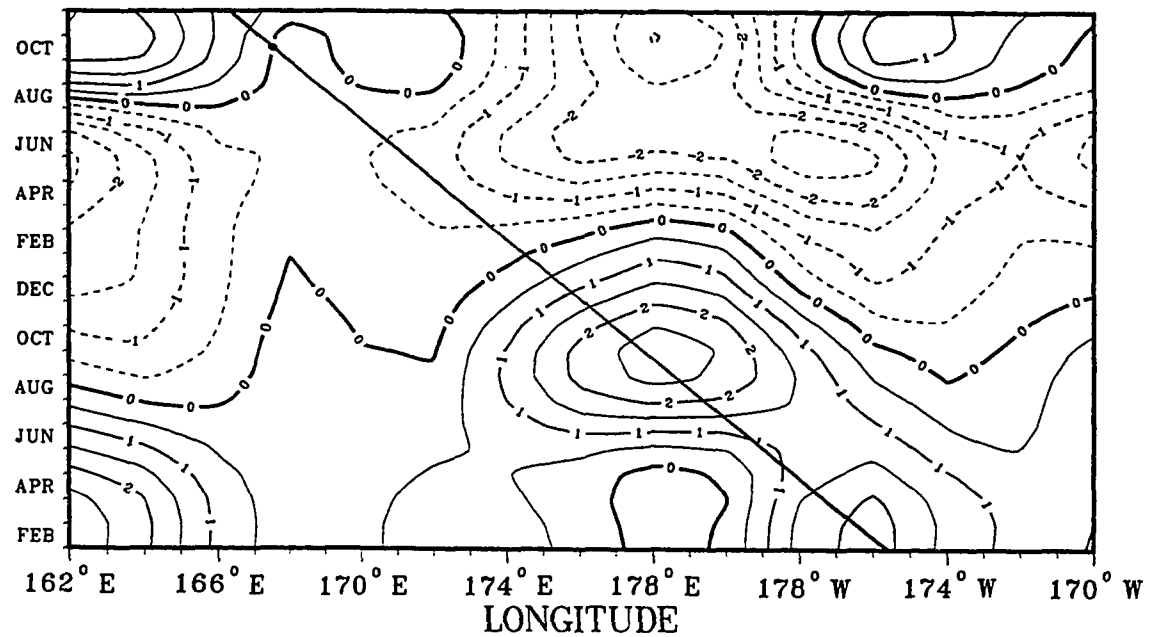

Figure 4.11 Longitude-time plot of mode 2 + mode 3 reconstructed SSH anomalies along 56.5°N. The inclined line represents an estimated phase speed of -1.9 cm s^{-1}. Contour interval is 0.5 cm.

$$\varphi(t) = \tan^{-1}\left[\frac{TAF_3(t)}{TAF_2(t)}\right] \tag{4.1}$$

where t is time in months. The time derivative (slope) of the phase gives the fluctuation frequency of the combined second and third mode anomaly field. The derivative was estimated by a least squares fit of the computed phase to a linear trend and bias. Inverting the frequency gives a period for westward propagating anomalies of 1.93 ± 0.06 years.

A longitude-time plot for the zonal band of grid cells centered at 56.5°N was reconstructed from the second and third modes to emphasize propagating features (Figure 4.11). This longitude band was chosen because it zonally spans the center of the deep basin. The plot shows two

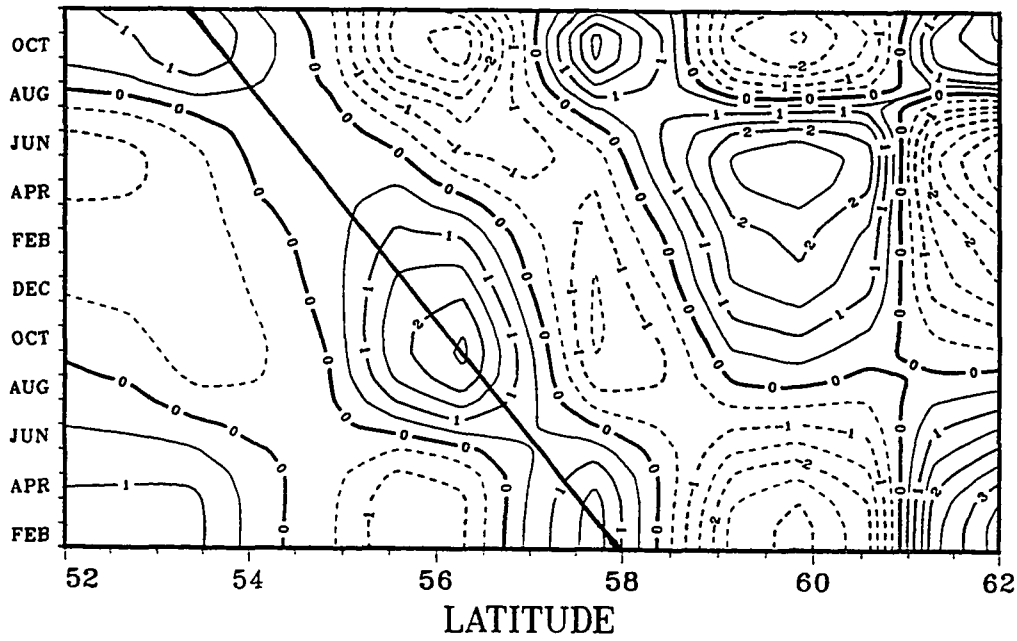

Figure 4.12 Latitude-time plot of mode 2 + mode 3 reconstructed SSH anomalies along 179°E. The inclined line represents an estimated meridional phase speed of -0.9 cm s^{-1}. The contour interval is 0.5 cm.

regions of elevated variability. The western region reflects the presence of the East Kamchatka Current. The eastern region indicates westward propagation of SSH anomalies across the central Aleutian Basin from roughly 173°W to 173°E. The zonal phase speed estimated from the longitude-time plot is -1.9 cm s^{-1}. The corresponding zonal wavelength, λ_x, given by the product of the zonal phase speed and estimated period, is about 1160 km.

The latitude-time plot of reconstructed SSHa along the meridional band centered at 179°E is shown in Figure 4.12. This latitude band was chosen because it meridionally spans the center of the deep basin. The inclination of the reconstructed SSHa contours south of 61°N indicate the

anomalies have a southward component of propagation away from the shelf break. The amplitude of the anomaly field is diminished near 54.5°N which suggests that Bowers Ridges acts as a partial barrier to propagation. It is inferred from the orientation of the nodal lines at 61°N that there is little or no cross-shelf propagation at this shelf-break location. The meridional phase speed estimated from the slope of the southward propagating features is about -0.9 cm s^{-1}. The corresponding meridional wavelength, λ_y, given by the product of the meridional phase speed and estimated period, is about 550 km.

Simple geometry determines the direction of anomaly propagation to be 205°T. The wavelength in the direction of propagation, λ, given by

$$\frac{1}{\lambda^2} = \frac{1}{\lambda_x^2} + \frac{1}{\lambda_y^2}, \tag{4.2}$$

is computed to be about 500 km. The phase speed in the direction of propagation, c, similarly obtained,

$$\frac{1}{c^2} = \frac{1}{c_x^2} + \frac{1}{c_y^2} \tag{4.3}$$

is about 0.8 cm s^{-1}.

The relatively long period and long wavelength which characterize the propagating anomalies suggest that they may represent the surface signature of baroclinic Rossby waves. The dispersion relation for baroclinic Rossby waves is

$$\omega = -\frac{\beta k}{k^2 + l^2 + \lambda_i^{-2}} \tag{4.4}$$

in which ω is the wave frequency, β is the meridional derivative of the Coriolis parameter, k and l are the zonal and meridional wavenumbers and λ_i is the internal Rossby radius of deformation given by

$$\lambda_i^2 = \frac{g\, h_{eq}}{f^2}. \qquad (4.5)$$

where f is the Coriolis parameter, g is the gravitaional acceleration, and h_{eq} is the upper layer equivalent depth.

For wavelengths long compared to the radius of deformation (4.4) can be simplified to give the phase speed for non-dispersive baroclinic Rossby waves

$$\frac{\omega}{k} = -\beta\lambda_i^2. \qquad (4.6)$$

Kinder and Coachman (1977), using a two layer approximation, estimate the internal radius of deformation for the eastern Aleutian Basin to have a seasonal range of between 7 and 20 km.

Substituting a mid-range deformation radius of 14 km into (4.5) along with $\beta = 1.28\text{x}10^{-11}$ s^{-1} m^{-1} gives a theoretical zonal phase speed of only 0.25 cm s^{-1} for baroclinic Rossby waves at Bering Sea latitudes. This is significantly less than the 'observed' zonal phase speed of 1.9 cm s^{-1}. Solving (4.5) using a 20 km Rossby radius gives zonal phase speed of only 0.51 cm s^{-1}, still significantly less than the 'observed' zonal phase speed.

Another perspective can be gained by considering whether westward propagating wave-like anomalies of the 'observed' period are allowed at latitudes spanned by the Bering Sea. This concept is specified in terms of a critical latitude, Φ_c

$$\Phi_c = \tan^{-1}\left(\frac{(g\, h_{eq})^{1/2}}{2R\omega}\right) \tag{4.7}$$

where R is the radius of the earth. The critical latitude is the latitude below which baroclinic Rossby waves of a given frequency are allowed to propagate away from an eastern boundary. Substituting (4.5) into (4.7) and expressing the Coriolis parameter as $2\Omega\sin\Phi_c$ allows the critical latitude to be expressed as a function of the internal Rossby radius

$$\Phi_c = \cos^{-1}\left(\frac{R\omega}{\Omega\lambda_i}\right). \tag{4.8}$$

Taking R = 6371 km, $\omega = 2\pi/1.9$ yr = $1.11\text{x}10^{-7}$ s^{-1}, $\Omega = 7.29\text{x}10^{-5}$ s^{-1}, and λ_i = 14 km establishes the critical latitude for a 1.9 yr baroclinic Rossby wave at about 46°N. However, for λ_i = 20 km the critical latitude is about 61°N. Even though reasonable estimates of the internal Rossby radius locate the Bering Sea near the critical latitude for a 1.9 year baroclinic Rossby wave, it can not be concluded that the observed waves are, in fact, baroclinic Rossby waves because they propagate much faster than the theoretical wave speed. To address the discrepancy between observation and theory it is helpful to consider wind forcing as a generating mechanism.

Figure 4.13 shows the averaged autospectral density of wind stress curl over the Aleutian Basin. In addition to the dominant spectral peak at a period of one year, there is a tertiary peak at about 1.8 years. This is very nearly the estimated period of variability for the (mode 2 + mode 3) anomaly field. This suggests that these propagating anomalies are resonantly forced by this particular spectral component of the wind. This does not

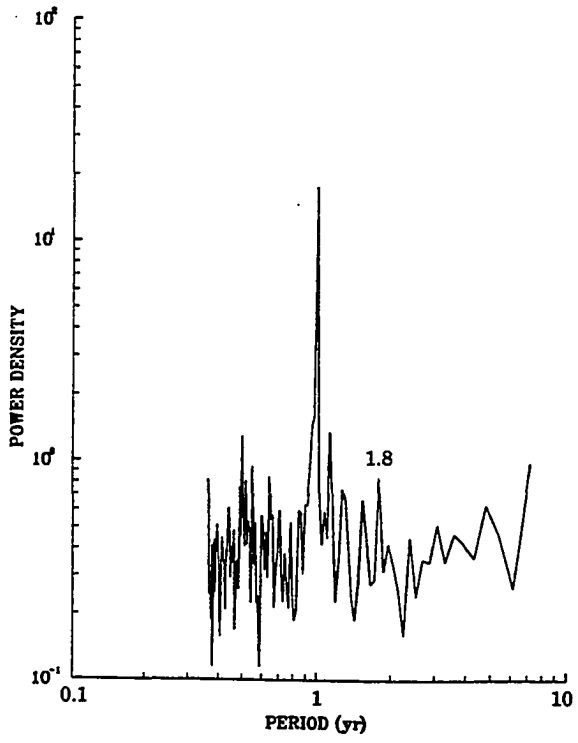

Figure 4.13 Spatially averaged autospectral density of 3° x 3° wind stress curl between 51°N and 60°N and between 175°E and 173°W.

mean that the observed wave-like anomalies are baroclinic Rossby waves but that a mechanism exists for the generation of these anomalies. This is essentially the same argument offered by White and Tabata (1987) and Matthews et al. (1992) for fast (relative to the theoretical baroclinic Rossby wave speed) propagating annual period waves in the North Pacific.

Recall that for the first mode, the eigenvector pattern was characterized by basin scale anomalous circulation. The individual eigenvector elements having the greatest amplitudes occured along the western boundary. In contrast, the second and third mode eigenvector patterns were characterized by gyre scale features, whose greatest

amplitudes occured in the Aleutian and Kamchatka Basins. In a simsilar manner, the first mode differs from the second and third modes according to their characteristic time scales. The first mode fluctuates annually whereas, the second and third modes fluctuate interannually. Note also that the variance explained by combining the second and third modes is very roughly equivalent to (although somewhat larger than) that explained by the first mode. This suggests that flow in the East Kamchatka Current is largely seasonal whereas circulation in the Aleutian Basin more closely reflects the influence of low frequency, westward propagating baroclinic waves. This suggestion is largely borne out by seasonal maps of SSH anomaly fields reconstructed from the first three modes (Figures 4.14a-d). Both winter maps suggest anomalous cyclonic circulation extends over much of the deep Bering Sea to support strong flow along the western boundary, although outflow through Kamchatka Strait is inferred to be weaker in 1988 than in 1987. In contrast, the summer maps indicate that the most prominent circulation features reside primarily in the Aleutian Basin interior. The propagation of low frequency, baroclinic long waves across the Aleutian Basin provides a possible explanation for some of the differences between the many proposed circulation schemes, some of which were depicted in Figure 3.1 (see also Hughes et al., 1974). For example, Ratmanov's (1937) circulation scheme shows an anticyclonic gyre in the southern Aleutian Basin whereas, Arsen'ev 's (1967) scheme shows a cyclonic gyre at the same location. A propagating gyre scale wave (anomaly) would, over its period of variability, effect circulation patterns having opposite directions of rotation.

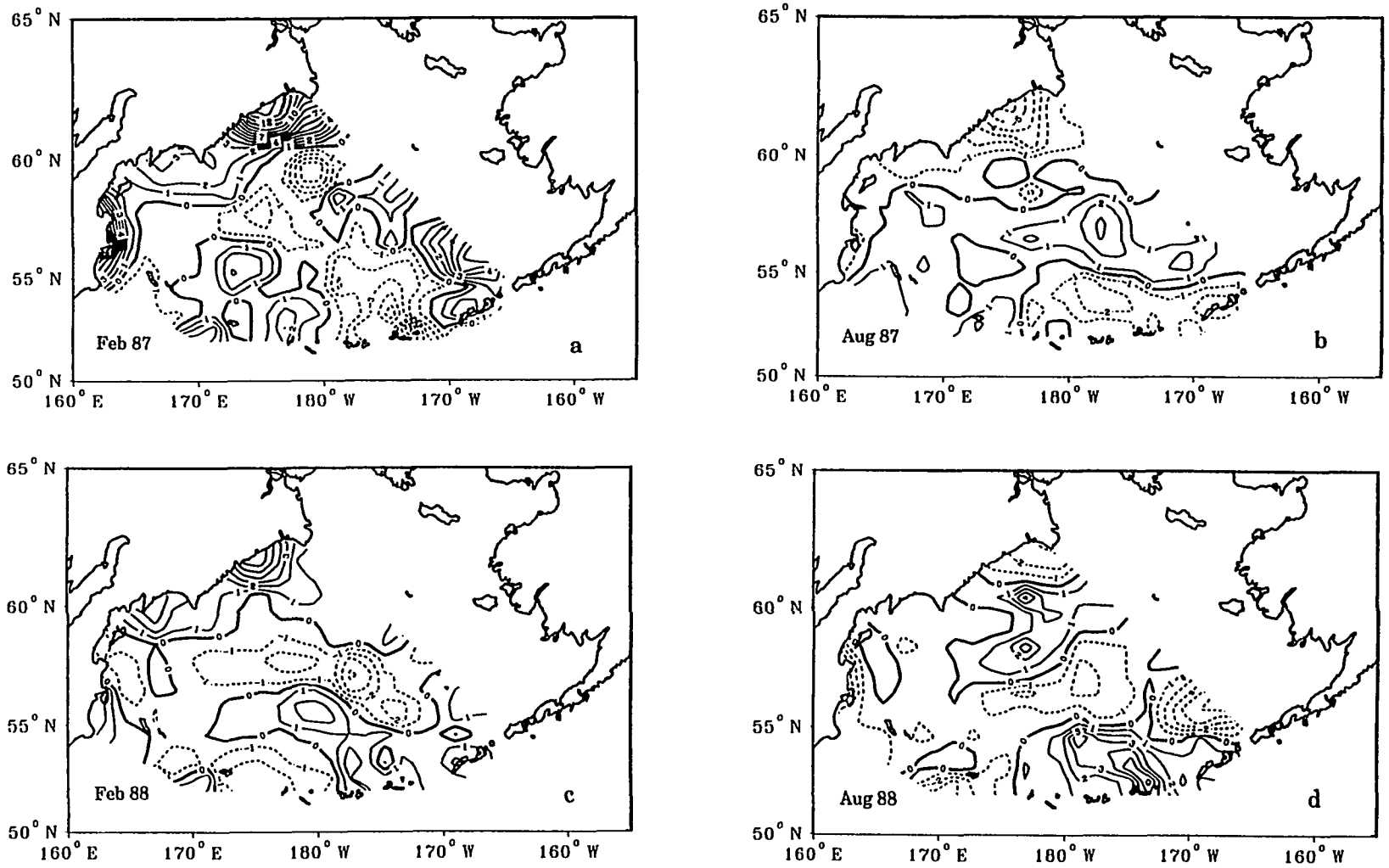

Figure 4.14 Seasonal maps of the reconstructed mode 1 + mode 2 +mode 3 SSH anomaly field.

a) Feb 1987, b) Aug 1987, c) Feb 1988, d) Aug 1988.

Section 4.3 The influence of the Alaskan Stream eddy on circulation in the Bering Sea

It was hypothesized in Chapter 3 that the Alaskan Stream eddy might influence circulation in the Bering Sea. If the Alaskan Stream eddy does influence circulation in the Bering Sea and/or if factors that lead to eddy generation are also factors which influence circulation in the Bering Sea, then an EOF analysis of a larger data set which includes data for the grid cells south of the Aleutians through which the eddy passed (i.e. including the direct statistical influence of SSH variability associated with the eddy itself) should result in modes of variability similar to the modes described above. An EOF analysis was performed on a space-time matrix of the GEOSAT data which included an additional 16 grid cells south of the Aleutians (Figure 4.15). The resulting eigenvalues for modes above the noise level are summarized in Table 4.4.

Table 4.4 Variance explained by the first four EOF modes of SSHa in the Bering Sea. Cumulative variances may not agree with the sum of the individual variances due to round off errors. (123 grid cells).

Mode	1	2	3	4
Variance explained (%)	35.3	18.3	15.3	7.7
Cumulative variance (%)	35.3	53.6	68.9	76.5

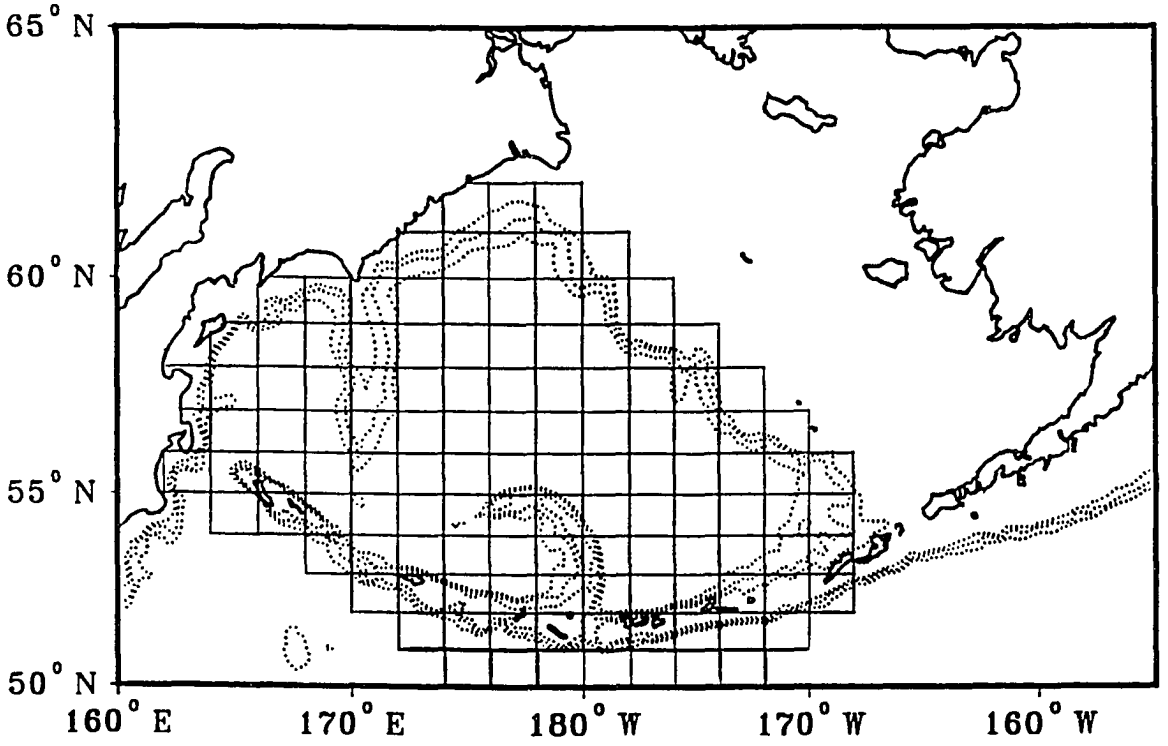

Figure 4.15 Locations of the 123 2.0° longitude x 1.0° latitude grid cells.

The eigenvectors and TAFs for the first three modes (Figures 4.16 - 4.18) exhibit essentially the same spatial patterns and periods of variability as obtained from the EOF analysis of the original, smaller space-time matrix. However, the relative rankings and the variances explained by these modes have been altered. The first and second EOF modes for the 123 grid cell space-time matrix resemble the second and third EOF modes for the original 107 grid cell space-time matrix. The Alaskan Stream eddy is the most significant feature in both these modes. The location of the eddy center in the second mode is to the west of its first mode location. What was the first mode of variability for the original space-time matrix has become the third mode for the augmented matrix. The variance explained by the

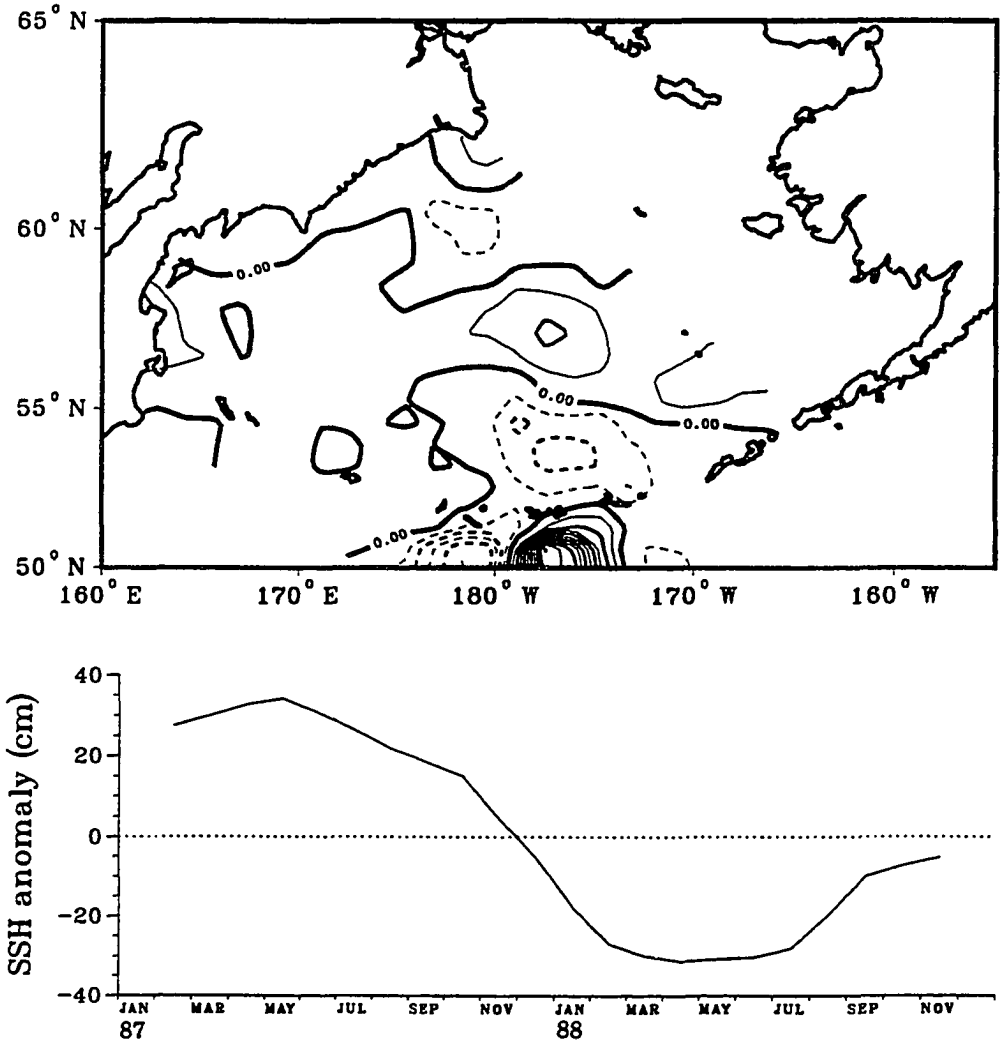

Figure 4.16 First mode eigenvector pattern and time amplitude function. The contour interval is 0.05.

fourth mode was less than twice the noise level and is not described.

To visualize the relationship between the Alaskan Stream eddy and circulation in the Aleutian Basin, monthly maps of low frequency variability in the SSHa field were reconstructed from the first two EOF

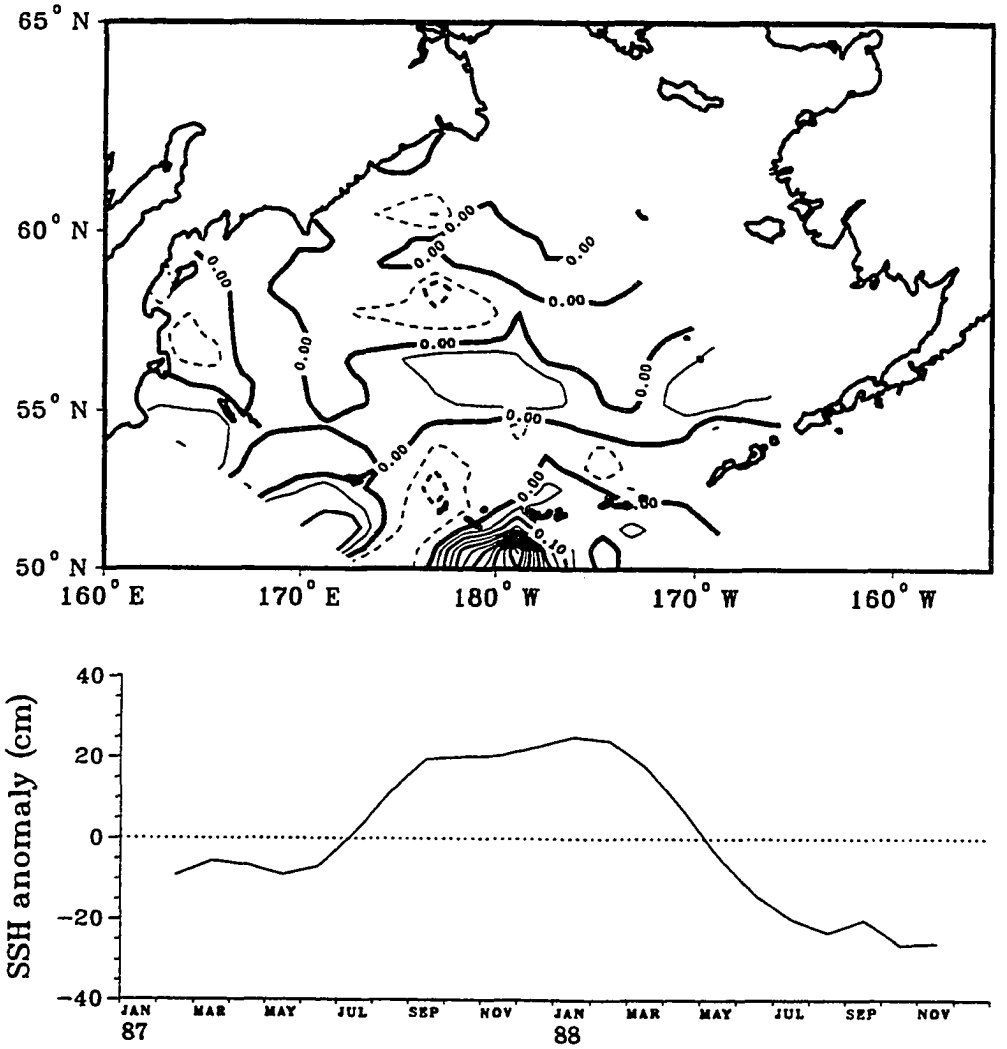

Figure 4.17 Second mode eigenvector pattern and time amplitude function. The contour interval is 0.05.

modes depicted in Figures 4.16 and 4.17 (i.e. the two modes dominated by variability associated with the Alaskan Stream eddy). Selected monthly maps are shown in Figure 4.19 to 4.24. The June 1987 map (Figure 4.19) closely resembles the spatial pattern of the mode 1 eigenvector. Circulation

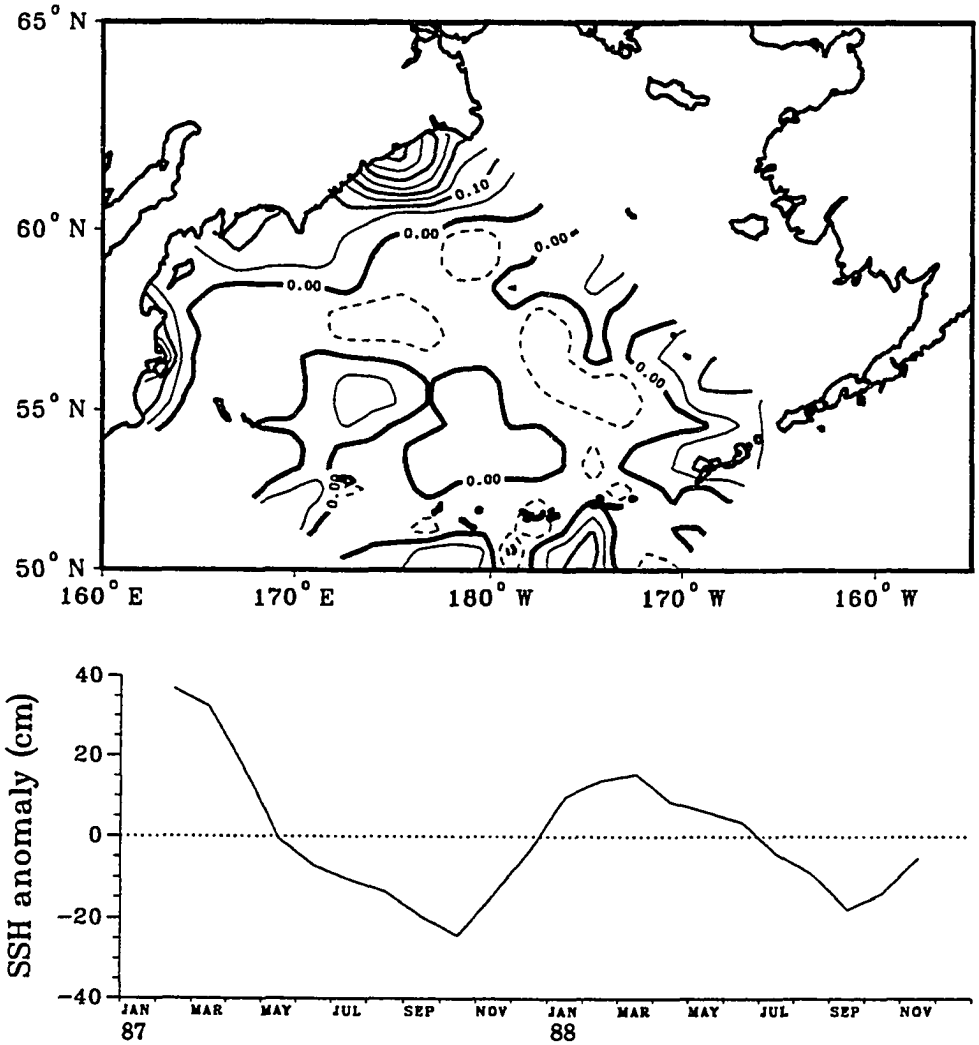

Figure 4.18 Third mode eigenvector pattern and time amplitude function. The contour interval is 0.05.

in the southern Aleutian Basin is more cyclonic (or equivalently, less anticyclonic) than the local, two year mean circulation. Eigenvector contours passing through Amchitka Pass suggest southward flow (or reduced northward flow) through the pass. The August 1987 map (Figure

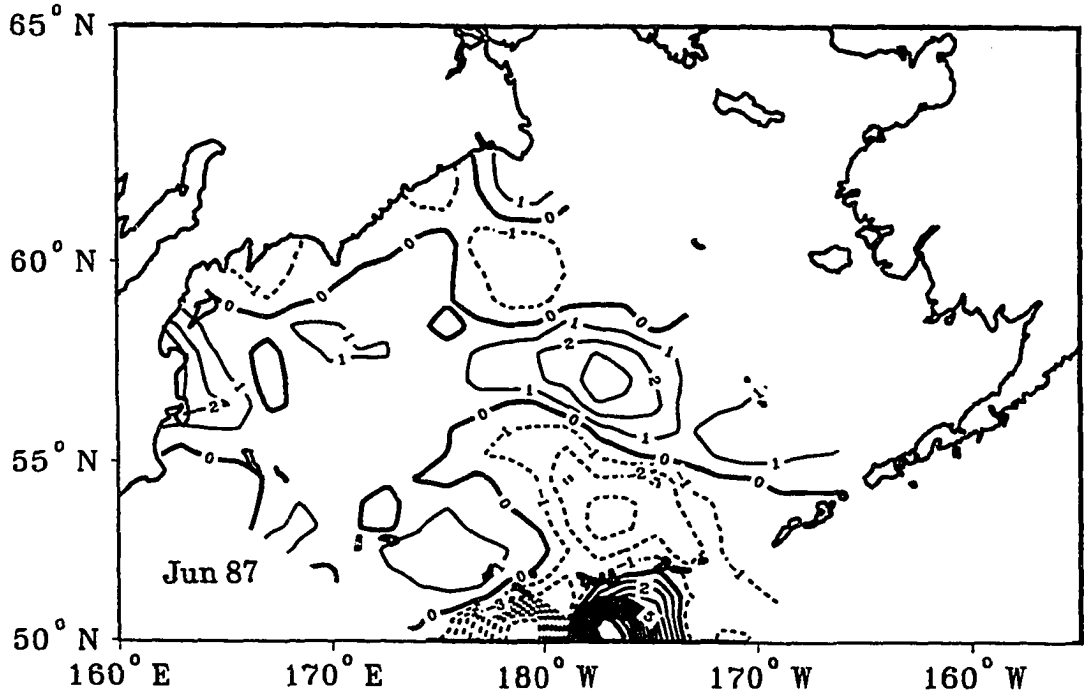

Figure 4.19 Map of the reconstructed mode 1 + mode 2 SSH anomaly field for June 1987 (123 grid cells). The contour interval is 1 cm.

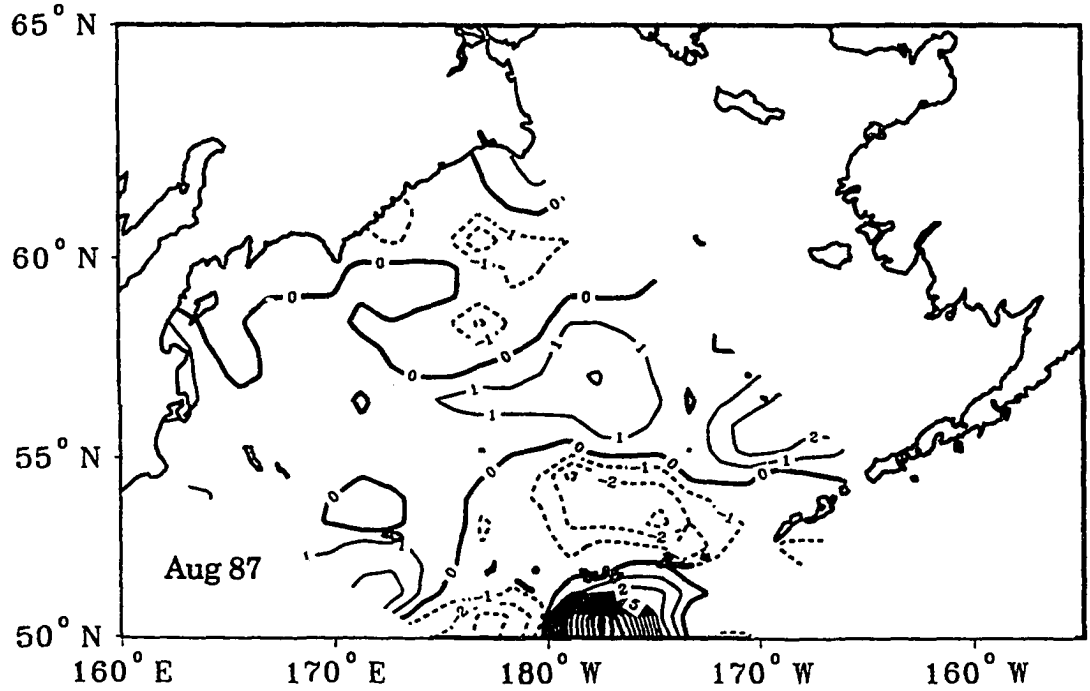

Figure 4.20 Map of the reconstructed mode 1 + mode 2 SSH anomaly field for August 1987 (123 grid cells). The contour interval is 1 cm.

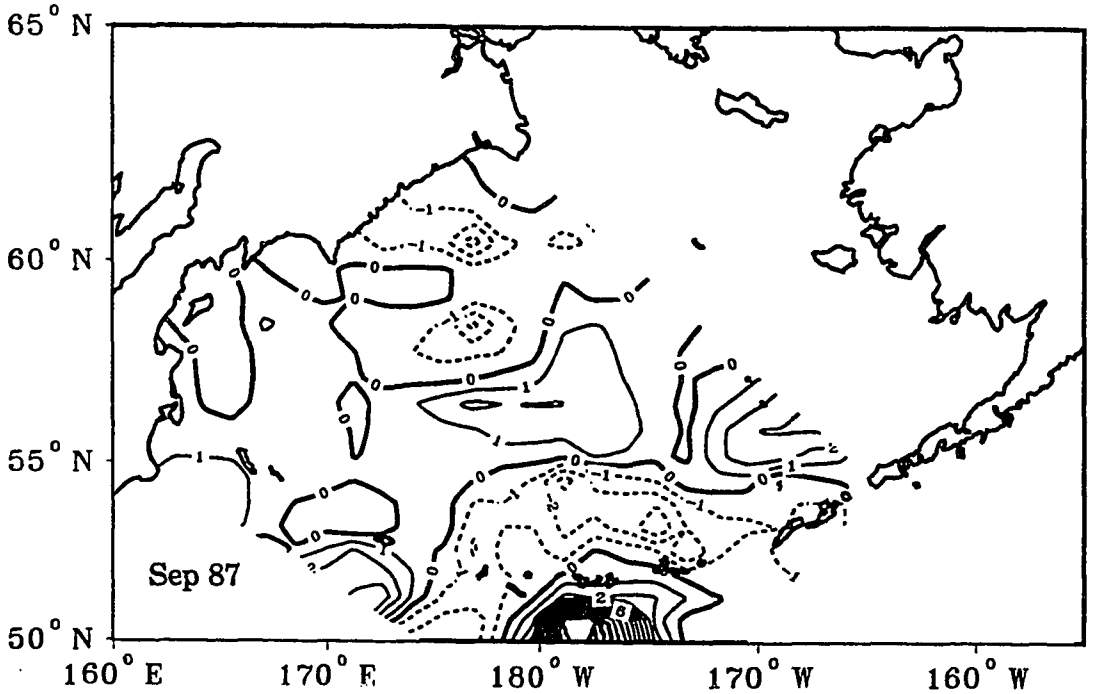

Figure 4.21 Map of the reconstructed mode 1 + mode 2 SSH anomaly field for September 1987 (123 grid cells). The contour interval is 1 cm.

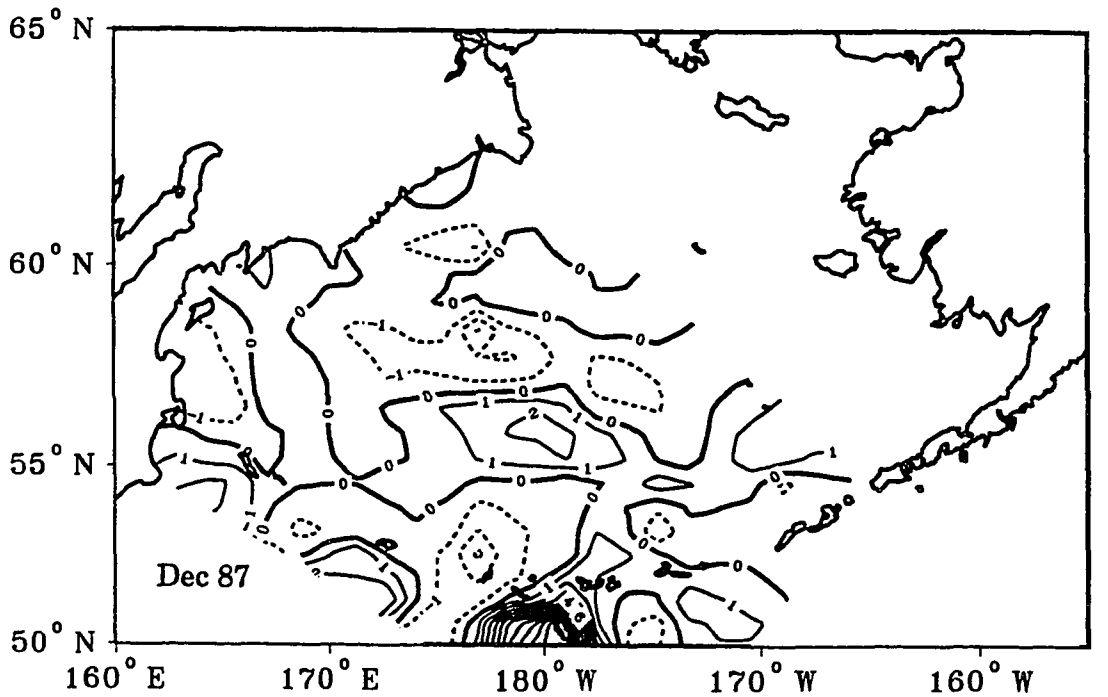

Figure 4.22 Map of the reconstructed mode 1 + mode 2 SSH anomaly field for December 1987 (123 grid cells). The contour interval is 1 cm.

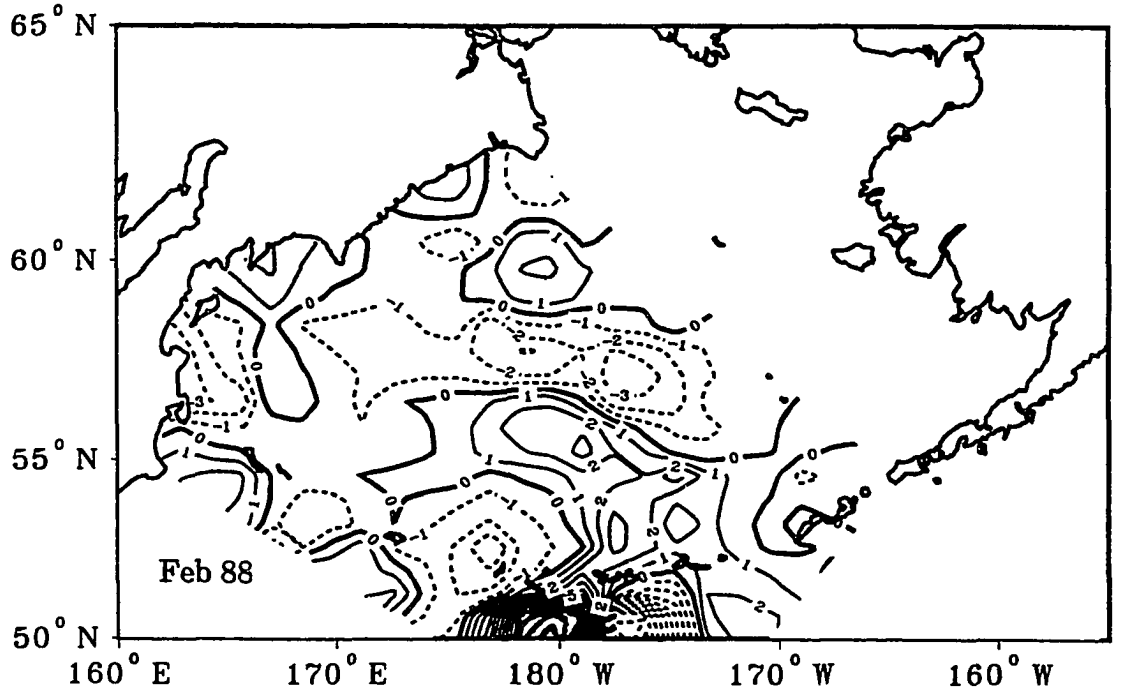

Figure 4.23 Map of the reconstructed mode 1 + mode 2 SSH anomaly field for February 1988 (123 grid cells). The contour interval is 1 cm.

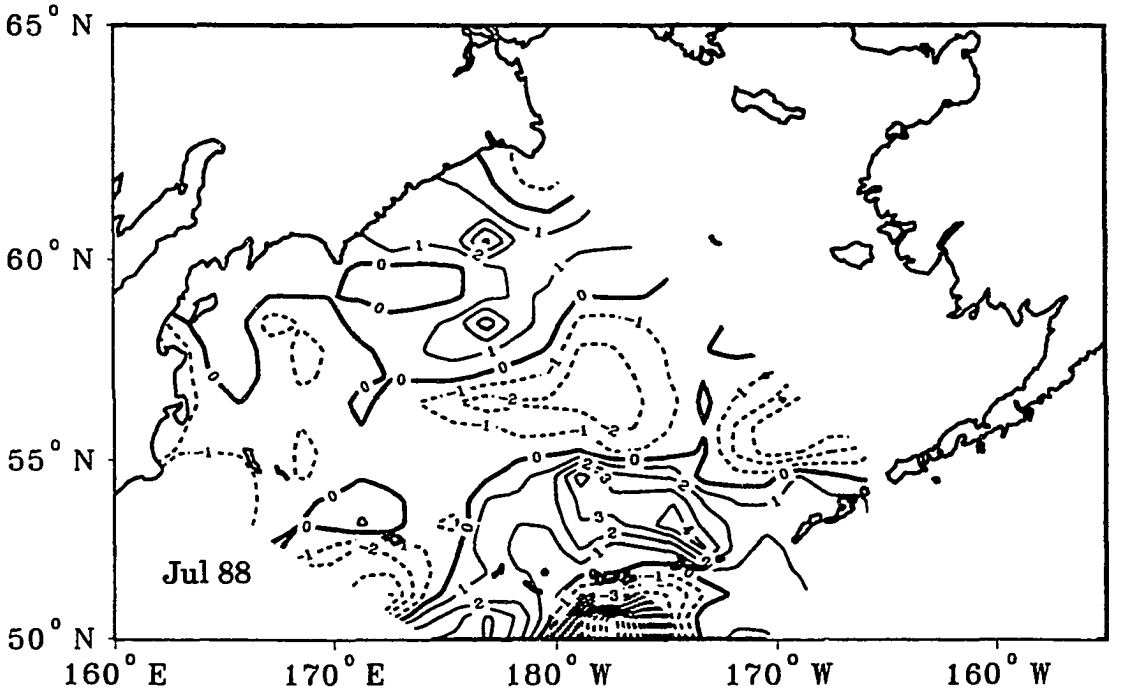

Figure 4.24 Map of the reconstructed mode 1 + mode 2 SSH anomaly field for July 1988 (123 grid cells). The contour interval is 1 cm.

4.20) is similar to the June map except that the amplitudes of the SSH anomaly features have diminished. The existence of flow through Amchitka Pass can not be determined. In September 1987 (Figure 4.21) the eigenvector node bordering the Alaskan Stream eddy passes through Amchitka Pass to form a northward protruding positive SSH anomaly near 177°W. The eigenvector contours suggest this anomaly is fed by flow from the Alaskan Stream eddy through Amchitka Pass. In December 1987 (Figure 4.22) the protrusion has extended northward along 177°W to connect with the 'anticyclonic' gyre-like feature lying between Bowers Ridge and Zhemchug Canyon. By February 1988 (Figure 4.23) circulation in the southern Aleutian Basin has become anticyclonic (less cyclonic) while the two other main gyre-like anomalies in the Aleutian Basin have also changed their sense of rotation (relative to June 1987). The contour spacing in Amchitka Pass is closest from December 1987 through March 1988 (January and March 1988 not shown) indicating that the greatest northward flow through the pass occurs during these months. Flow becomes indeterminate in June 1988 and southward the following month (Figure 4.24). While circulation in the southern Aleutian Basin appears to be influenced by the presence of the Alaskan Stream eddy the data does not allow such a connection to be conclusively extended to the rest of the Aleutian Basin. Nonetheless, a signal could pass through Amchitka Pass as a Kelvin wave (Leblond and Mysak, 1978) and propagate along the continental slope to trigger long wave propagation. Because Kelvin waves propagate very quickly such a signal could not be detected by the altimeter.

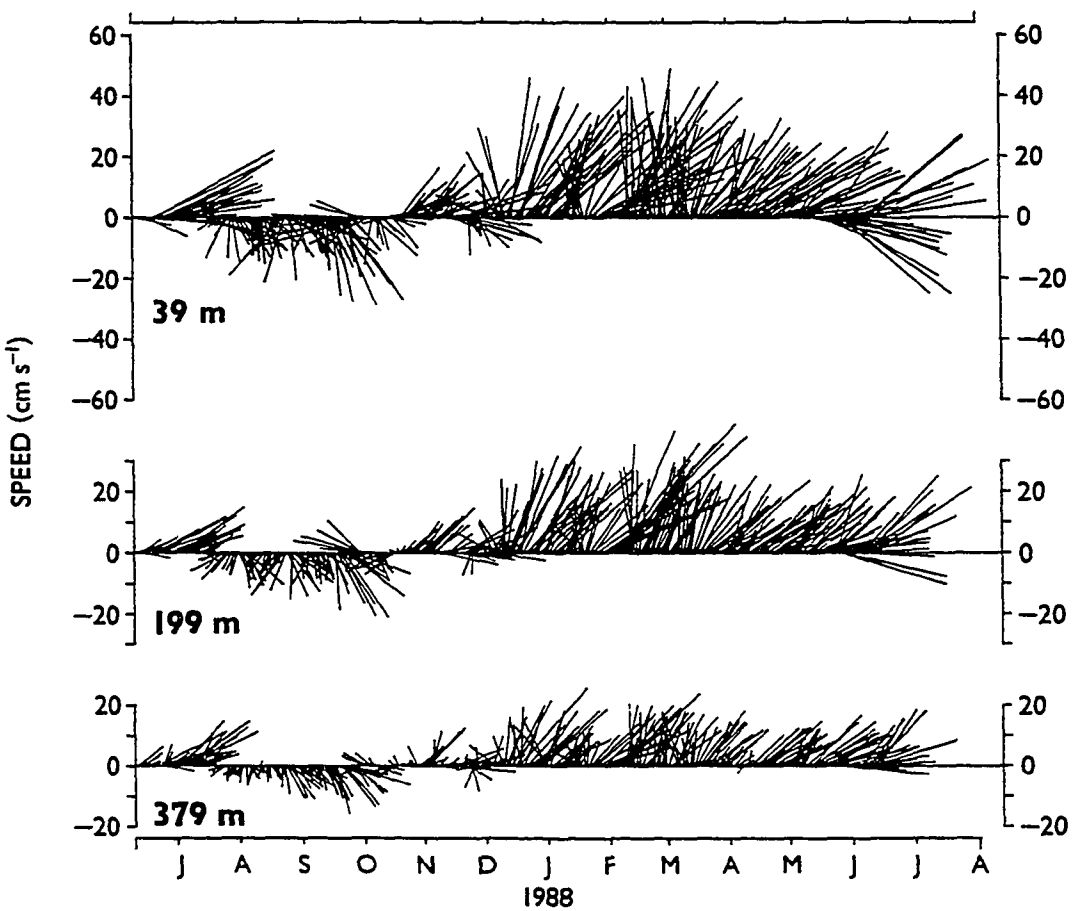

Figure 4.25 Daily net current vectors at the Amchitka Pass mooring (after use of 35 h filter), 11 June 1987 - 12 June 1988. Up is north on the plots. (from Reed, 1990).

Figure 4.25 shows a year long record (June 1987-June 1988) of current meters moored in Amchitka Pass (Reed, 1990). There initially is a northward component of flow through the pass. Flow having a southward component begins in July 1987 and continues until October 1987 when a northward component of the flow is reestablished. Near the end of the record the flow is generally eastward with alternating weak northward and southward components. Overall, periods of inflow and outflow

through Amchitka Pass as inferred from the maps of recontructed SSHa are in reasonable agreement with those indicated by the current meter record. The discrepencies between what is indicated by the current meter records and what is inferred from the reconstructed SSHa data are likely attributable to the severe temporal and spatial smoothing of the SSHa data prior to the EOF analysis.

In the previous chapter, the eddy center was seen to be located near the longitude of Amchitka Pass during the first months of 1988 and that the eddy height at this time was estimated to be about 40 cm. Toulany and Garrett (1984) have shown that flow through a pass is geostrophically limited by the difference between sea surface heights at the ends of the pass. Accordingly, the maximum geostrophic current through the pass is

$$v = \frac{g}{f}\frac{\partial \eta}{\partial x} \tag{4.9}$$

for which

g acceleration due to gravity, 9.81 m s^{-1}

f Coriolis parameter, 1.14×10^{-4} s^{-1}

$\partial\eta/\partial x$ sea surface slope, 4.0×10^{-1} m / 9×10^{4} m = 4.4×10^{-6}.

The resulting northward flow is about 38 cm s^{-1}. In spite of the rough estimate for sea surface slope the computed current speed through the pass compares favorably with the ~45 cm s^{-1} estimated from Figure 4.25.

Section 4.4 Discussion and Conclusions

A scheme for low frequency, large scale surface circulation in the Bering Sea basin based on an EOF analysis of averaged SSH anomalies has been presented. The scheme reflects the superposition of a gyre scale system of westward propagating SSH anomalies (interpreted to be baroclinic long waves) on a generally cyclonic basin scale circulatory system. The latter system is characterized by weak interior flow feeding a relatively strong southwestward flowing western boundary current. The propagating long wave field has a period of about 1.9 years, whereas the intensity of the basin wide cyclonic circulation has an annual periodicity. The superposition of the two circulatory systems provides a potential resolution of some differences between the many proposed circulation schemes based on computations of the geostrophic circulation, water mass analysis, drifting buoys, and wind driven models. A large eddy in the Alaskan Stream appears to have a direct influence on flow through Amchitka Pass and on circulation in the southern Aleutian Basin.

The principal shortcoming of the analysis in the preceding sections of this chapter is that it is predicated on a short data record. After smoothing the record spanned only 22 months. This is approximately the estimated period of the propagating baroclinic long waves and, as such, provides only one realization of the physical process responsible for their existence. Accordingly, the argument that they are forced by a 1.8 year component of the wind field is only conjecture.

While it would require many years of regular hydrographic surveys over the entire Bering Sea basin to verify the conceptual model of circulation based on the altimeter data, a numerical model would provide a perspective for comparison in a more timely manner.

Chapter 5 Topographic Planetary Waves in the Bering Slope Current

Introduction

The Bering Slope Current flows poleward along the eastern boundary of the Aleutian Basin, the largest of the three deep basins occupying the southwestern half of the Bering Sea (Figure 4.1). The shelf break, along which the Bering Slope Current flows, extends from the easternmost Aleutian Islands to south of Cape Navarin. The Bering Slope Current was first identified as a component of the Bering Sea circulation by Dobrovol'skii and Arsen'ev (1959). Named the 'Transverse Current', it was depicted as a northwestward flowing current adjacent to the eastern continental shelf. Since then numerous circulation schemes for the Bering Sea (e.g. Arsen'ev 1967; Takenouti and Ohtani, 1974; Hughes et al., 1974) have shown a broad northwestward flow paralleling the shelf break.

The first hydrographic study to specifically investigate the water mass characteristics, their distribution, and the associated flow field of this current system was reported by Kinder et al. (1975) who proposed the now generally accepted name 'Bering Slope Current'. The authors presented two descriptions of the current system, a three banded current and a system of eddies.

This chapter presents measurements made by the GEOSAT altimeter of sea surface height (SSH) anomalies in the vicinity of the Bering Slope Current (BSC) system. These measurements show that the

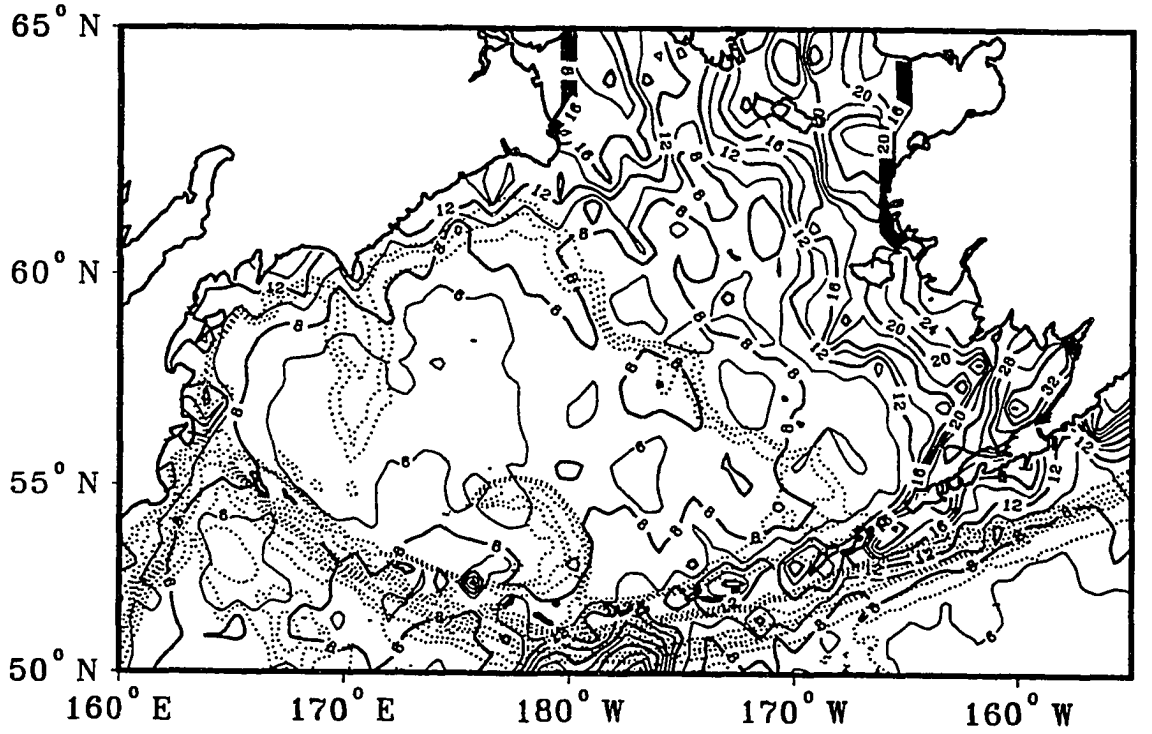

Figure 5.1 Two year (1987-1988) root mean square (rms) SSH variability in the Bering Sea. The contour interval is 2 cm.

downstream leg of the BSC, in contrast to the upstream leg, is characterized by a prominent SSH anomaly field whose wavelength and period satisfy the dispersion relation for topographic planetary waves.

Section 5.1 Observations

The BSC appears in the plot of the two year (1987-1988) root mean square (rms) variability as a band of moderate height variability with a maximum slightly greater than 8 cm (Figure 5.1). This band is just seaward of and parallel to the shelf break in the central Bering Sea and

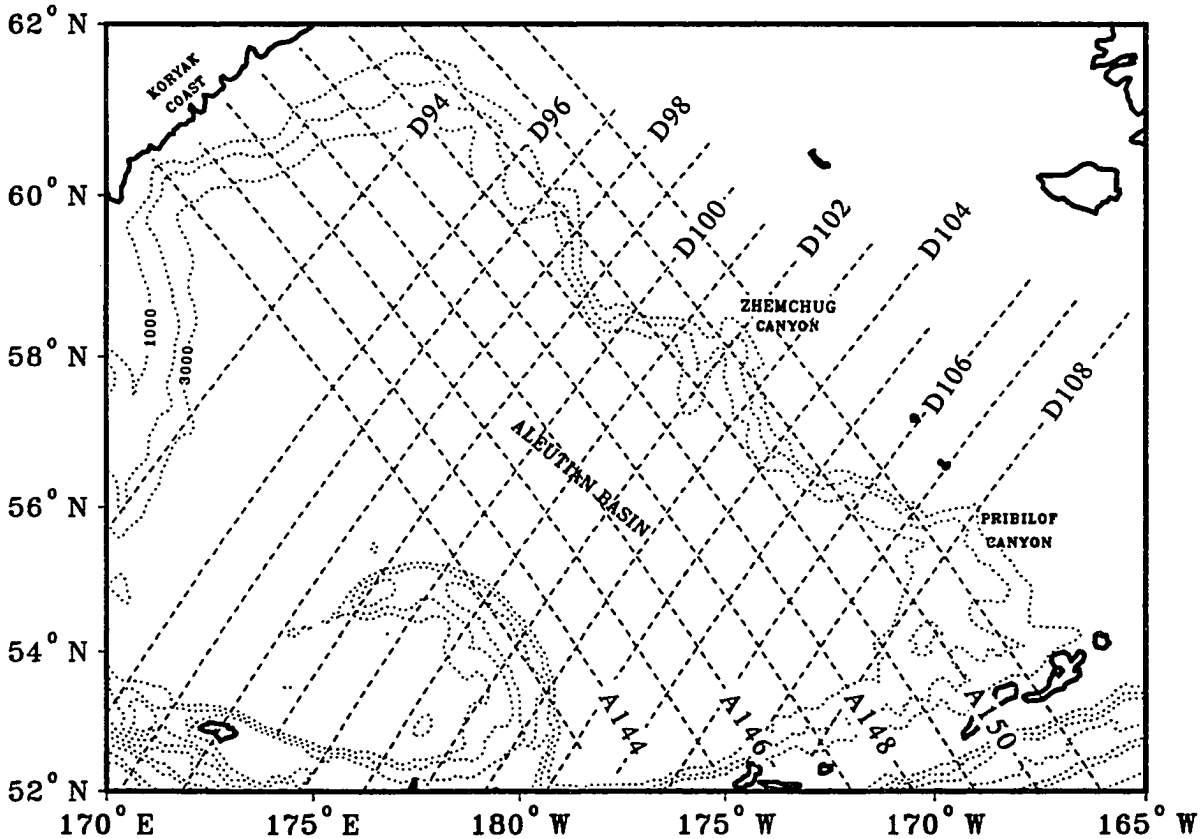

Figure 5.2 The locations of the ascending and descending orbital ground tracks in the Aleutian Basin along which measurements of SSH were acquired during orbital repeat cycle ERM 16. Bathymetric contours are also shown.

extends from near Pribilof Canyon to the Koryak coast south of Cape Navarin. Overall, the upstream half of the current, flowing between Pribilof Canyon and Zhemchug Canyon, exhibits somewhat less height variability than the downstream half. A local maximum in the variability is centered over the western flank of Zhemchug Canyon.

Altimetric observations along ascending orbital ground tracks A143 to A151 and descending orbital ground tracks D93 to D108 provide coverage

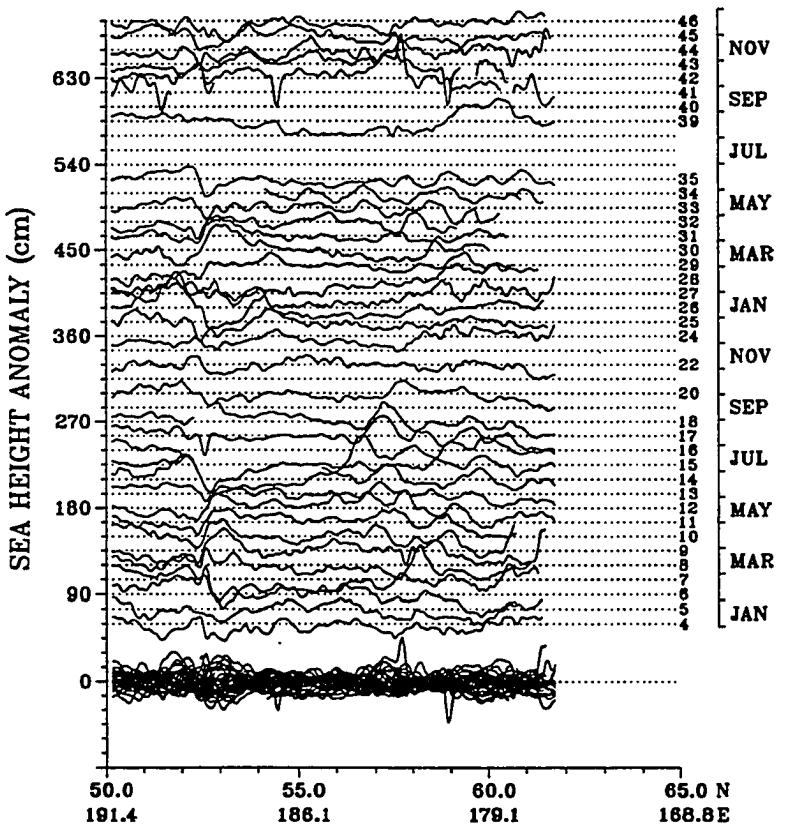

Figure 5.3 Two year (1987-1988) time series of SSH anomaly profiles along ascending ground track A148. The reference height for each individual along-track profile is displaced 15 cm from the preceding reference height. The orbital repeat cycle (ERM 4-46) is given to the right of each profile.

over the majority of the Aleutian Basin, including the domain of the BSC (Figure 5.2). The orientation of the ascending orbital ground tracks is nearly parallel to the longshore axis of the continental slope whereas the orientation of the descending ground tracks is approximately perpendicular. Comparison of Figure 5.1 and Figure 5.2 shows that the northwestern half of orbital ground track A148 lies approximately along the axis of the downstream leg of the BSC. Inspection of the time series of

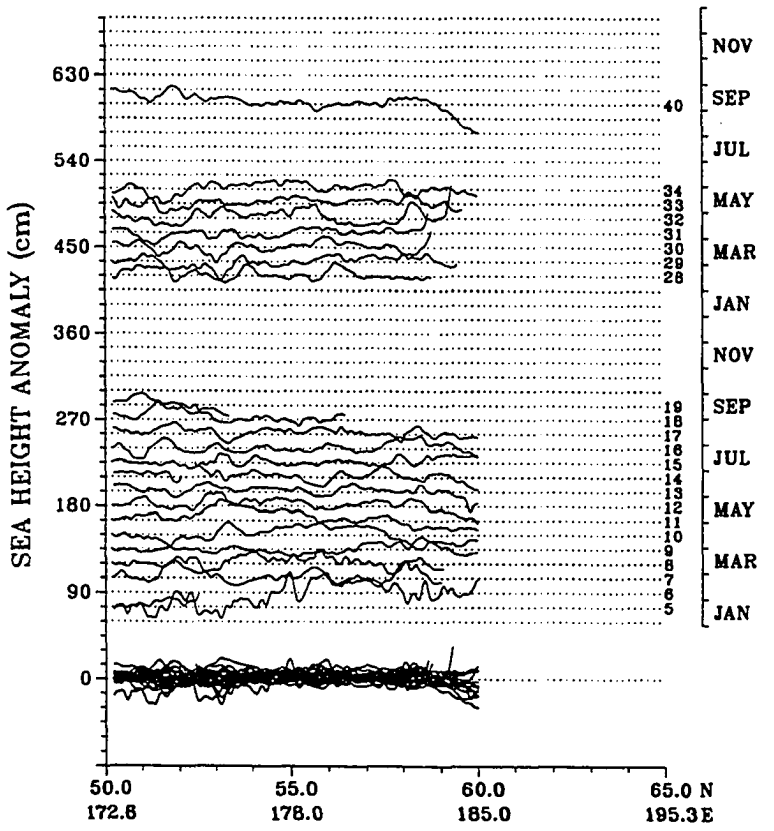

Figure 5.4 Same as Figure 5.3 only for descending ground track D100.

profiles of SSH anomalies along ground track A148 clearly shows that between roughly 56°N and 60°N there are prominent, regularly spaced SSH anomalies suggestive of a wave or eddy field (Figure 5.3). The wave field appears to be most prominent during May to August (ERMs 12-18) 1987. The wave field appears again in the spring of 1988 although the absence of observations in July and August make it difficult to compare the 1987 and 1988 wave fields. The height of the most prominent anomalies is about 25 cm. The directional trend of successive locations of 'wave crests' indicate that the propagation of the wave field has a northwestward component.

Crests appear at a given location about every four ERM orbital cycles during ERMs 12 to 18. This translates to a wave period of about 68 days.

Measurements of SSH anomalies acquired along descending ground track D100, which crosses the downstream leg of the BSC near its midpoint, show that there are two different off-shelf wave fields (Figure 5.4). The wave field over the vicinity of the continental slope (i.e. northeast of ~57.5°N) has a directional component of propagation to the northeast whereas the wavefield over the Aleutian Basin has a southwestward directional component of propagation. This suggests that the wave field observed in Figure 5.3 for ERMs 12 to 18 is limited in its off-slope extent.

Autospectra for each ERM orbital cycle of the eighty SSH anomalies lying between 56.1°N and 60.1°N along ground tracks A146, A147, and A148 were computed. Each eighty point spatial series was zero padded out to 159 points to improve the identification of spectral peaks. Individual autospectra were computed using a fast Fourier transform (FFT) routine and then time averaged for ERM orbital cycles 4-10 and 12-18. At wavelengths greater than about 100 km the power associated with the A146 anomaly field increases at all wavelengths from the earlier period to the latter (Figure 5.5a). The power associated with the anomaly field along orbital ground track A147 shows little seasonal change at wavelengths greater than 223 km, but increases at shorter wavelengths (Figure 5.5b). In particular, there is a prominent peak between 159 and 185 km. The two power spectra for the anomaly field along A148 indicate little seasonal change in power at the shorter wavelengths, but, as was the case for ground track A147, a prominent peak near 159 km dominates the

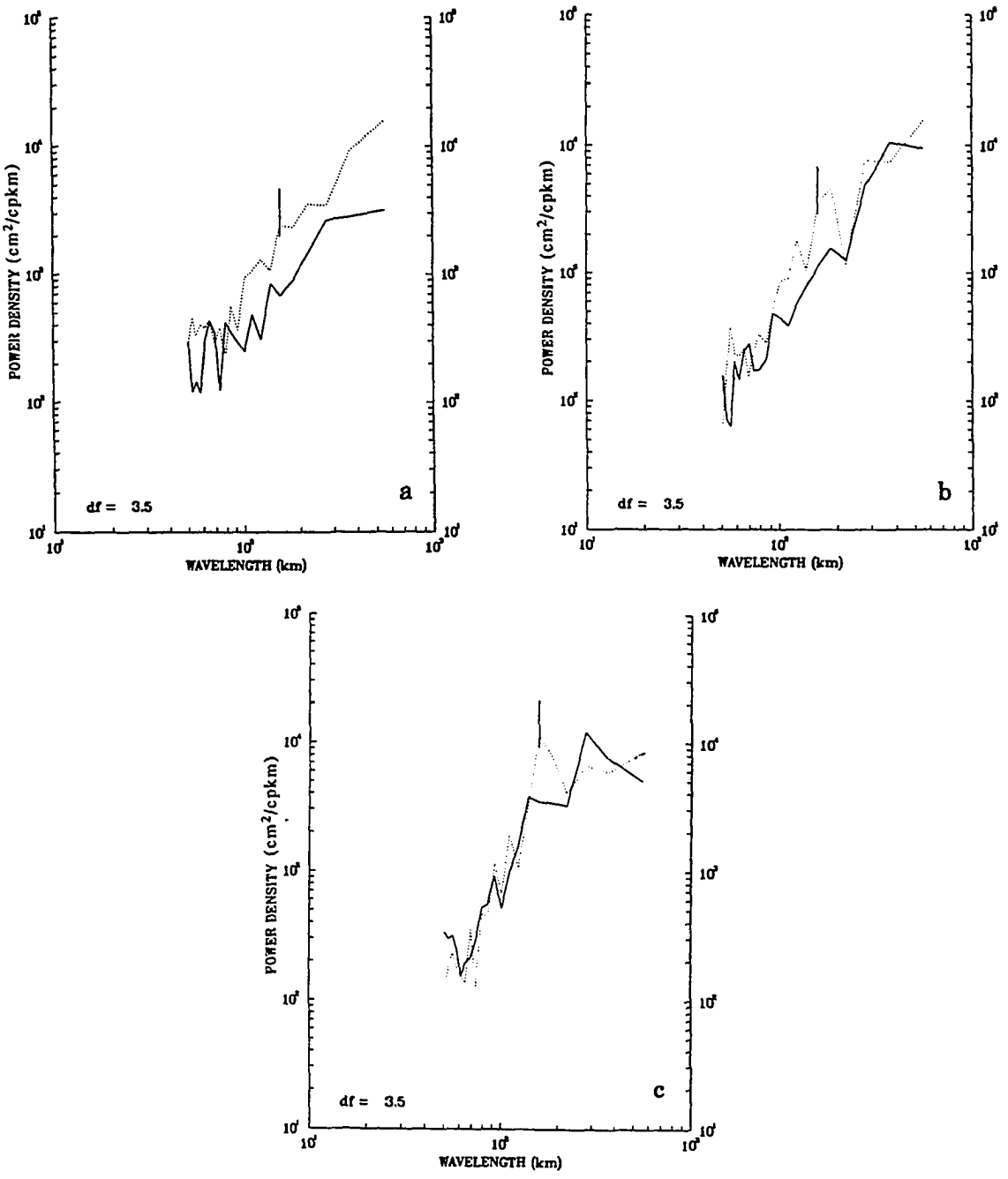

Figure 5.5 Seasonally averaged autospectral density of SSH anomalies along ground tracks (a) A146, (b) A147, and (c) A148 between 56.1°N and 60.1°N for ERM orbital repeat cycles 4 to 10 (solid line) and ERM orbital repeat cycles 12 to 18 (dotted line). The 70% confidence interval is shown for 159 km.

spectrum for the latter period (Figure 5.5c). The occurence of a spectral peak near 159 km in the A147 and A148 spectra for ERMs 12-18 and the absence of such a peak in the A146 spectrum for the same period corroborate the limited off-slope extent of the wave field as inferred from the descending track SSH anomalies shown in Figure 5.4.

Individual autospectra were also computed for each ERM orbital cycle of the twenty SSH anomalies along segments of descending ground tracks D96 to D101 lying between ground tracks A147 and A149. The shorter descending track segments were chosen to restrict sampling to waves near the continental slope (i.e. those waves with a northeastward along-track component of propagation). Each of the twenty point spatial series was also zero padded out to 159 points. Because GEOSAT acquired generally fewer measurements of SSH anomalies along descending ground tracks traversing the Bering Sea than were acquired along ascending ground tracks, space-time averages of the six descending ground track spectra during ERMs 4-10 and 12-18 were computed. Although there is no significant spectral peak, wave power decreases at all wavelengths from the earlier period to the latter with the smallest percentage decreases occuring at 101 km and 111 km (Figure 5.6).

For any given ERM repeat cycle, by using profiles of SSH anomalies, such as are shown in Figure 5.3, to locate the prominent wave crests along the ground tracks depicted in Figure 5.2 and by noting the directional component of propagation associated with each wave crest, the quasi-instantaneous wave field in the Aleutian Basin can be constructed by means of vector addition. The direction of propagation of the wave field is

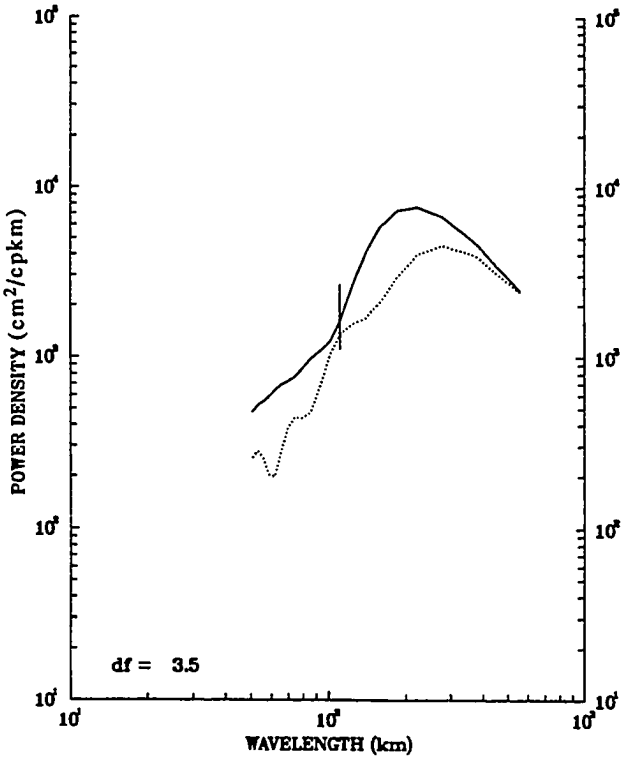

Figure 5.6 Seasonally and spatially averaged autospectral density of SSH anomalies along the portions of ground tracks D96 to D101 between ascending ground tracks A147 and A149 for ERM orbital repeat cycles 4 to 10 (solid line) and ERM orbital repeat cycles 12 to 18 (dotted line).

determined vectorially from the directional components of propagation along ascending and descending ground tracks. This has been done for orbital cycle ERM 16, a time when the wave field appears to be particularly well developed (Figure 5.7). The central time for this orbital cycle is 29 July 1987. Crest locations at which the direction of propagation is either ambiguous or uncertain are shown, but are not connected to other crest locations as part of an extended crest. There are five crests along the continental slope, one just south of Pribilof Canyon and four crests nearly

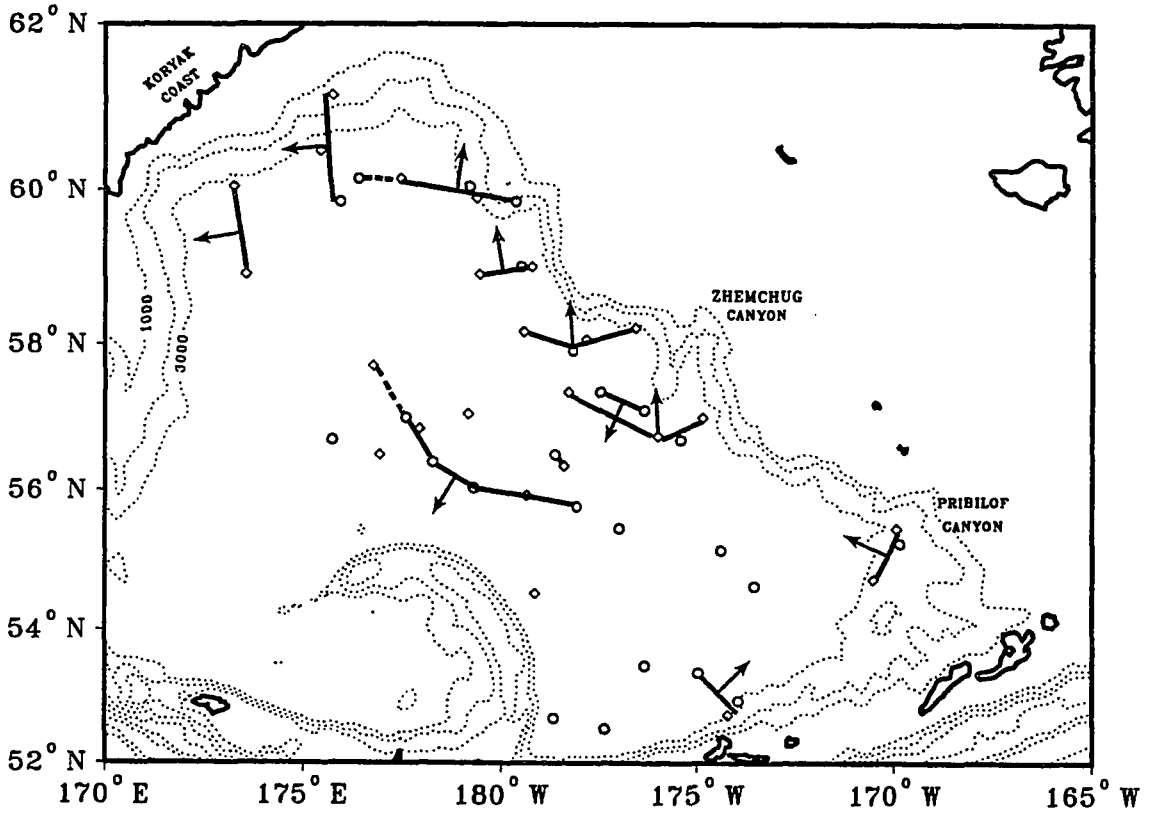

Figure 5.7 The quasi-instantaneous planetary wave field within the Aleutian Basin for orbital cycle ERM 16. Diamonds and open circles indicate the wave crest locations determined from SSH anomaly profiles along ascending and descending ground tracks, respectively. Arrows indicate the inferred direction of wave propagation.

evenly distributed from south of Zhemchug Canyon to 60°N, 179°E. The direction of phase propagation for these four crests is generally northward. A representative wavelength, measured parallel to the direction of propagation, for these four crests is about 110 km. Two crests are observed to be propagating to the southwest away from the vicinity of Zhemchug Canyon. There are also two westward propagating crests along the Koryak

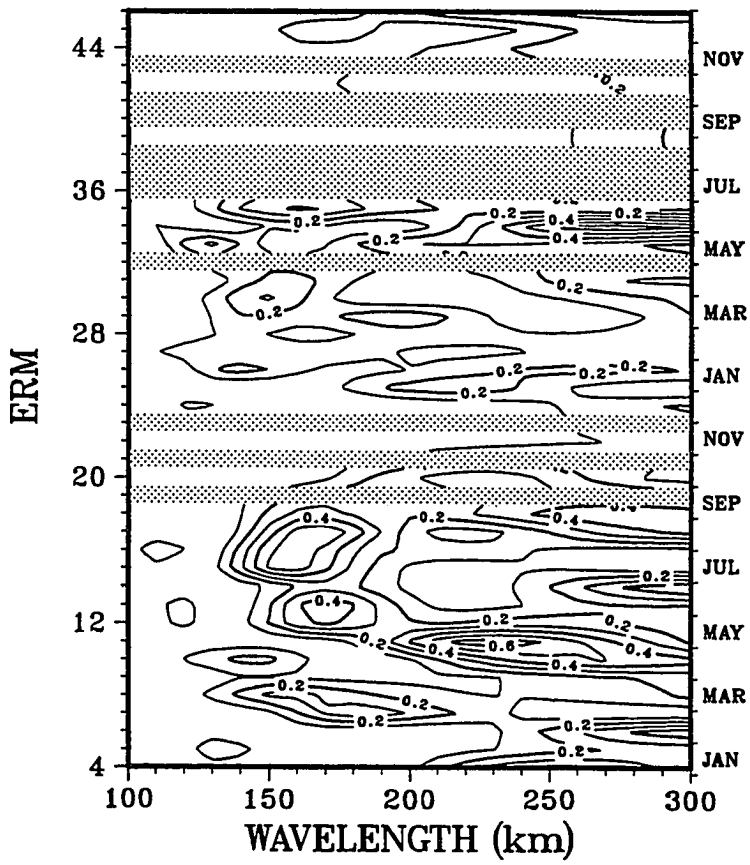

Figure 5.8 The distribution of the R^2 statistic in the wavelength-time domain for the wave field as sampled along ground track A148 between 56.1°N and 60.1°N. ERM orbital reat cycles for which there are no observations are shaded. the contour interval is 0.1.

coast. A single crest is seen to be propagating to the northeast in the southeastern portion of the basin.

A less subjective measurement of the wavelength can be obtained using a least squares procedure. The direction of propagation associated with the wave field can then be determined geometrically from the least squares estimates of wavelengths along ascending and descending tracks.

From the same eighty point (560 km long) profiles of SSH anomalies along ascending ground track A148 as were used in the computation of the autospectra, a linear trend and bias were first removed to filter out waves much longer than the peak along-track wavelength estimated above. This procedure was repeated for the same twenty point (140 km long) descending track profiles of SSH anomalies used in the computation of their autospectra. Each detrended and debiased profile of SSH anomalies was then fit in a least squares procedure to a sinusoid function, F(s),

$$F(s) = A \cos \frac{2\Pi}{\lambda} s + B \sin \frac{2\Pi}{\lambda} s \qquad (5.1)$$

where s is the along track distance of the individual SSH anomaly measurement from the beginning of the segment and where the wavelength, λ, is varied by 10 km increments from 100 - 300 km for the ascending track segments and from 80 - 280 km for the descending track segments. The R^2 statistic was computed for each least squares procedure and was plotted as a function of ERM orbital cycle and wavelength in order to identify peak wavelengths and their seasonal occurance.

The distribution of the R^2 statistic in the wavelength-time domain for wave field as sampled along ground track A148 shows that there are three principal wavebands whose peak wavelengths are at about 165 km, 230 km, and 300 km (Figure 5.8). The most persistent waveband, occuring from about ERM 12 to 18 (May-August), is centered at about 165 km. This estimate is effectively the same as the spectrally estimated peak wavelength. The 165 km waveband also appears for a shorter duration during ERM 7-8. Using the 0.3 R^2 contour to differentiate between it and

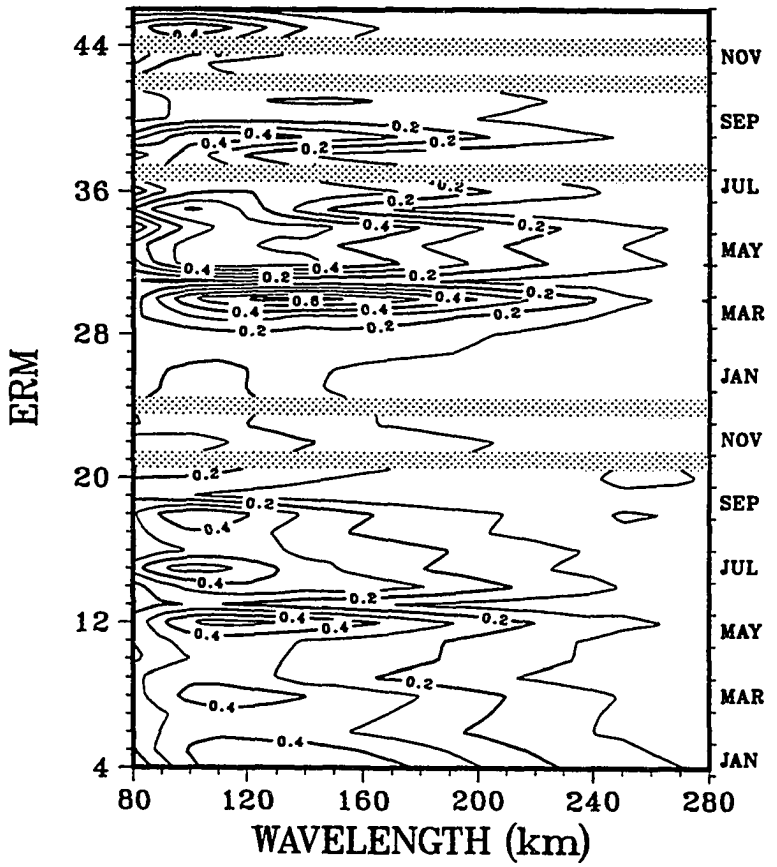

Figure 5.9 The distribution of the average R^2 statistic in the wavelength-time domain for the wave field as sampled along segments of ground tracks D96 to D100 between ascending ground tracks A147 and A149. ERM orbital repeat cycles for which there are no observations are shaded. The contour interval is 0.1.

the waveband centered at 230 km, the 165 km waveband has an average bandwidth of about 40 km.

Figure 5.9 shows the distribution of the average R^2 statistic for ground tracks D96 to D101. The peak wavelength decreases from about 130 km during ERM 4 to about 105 km during ERM 18 and the intensity of the

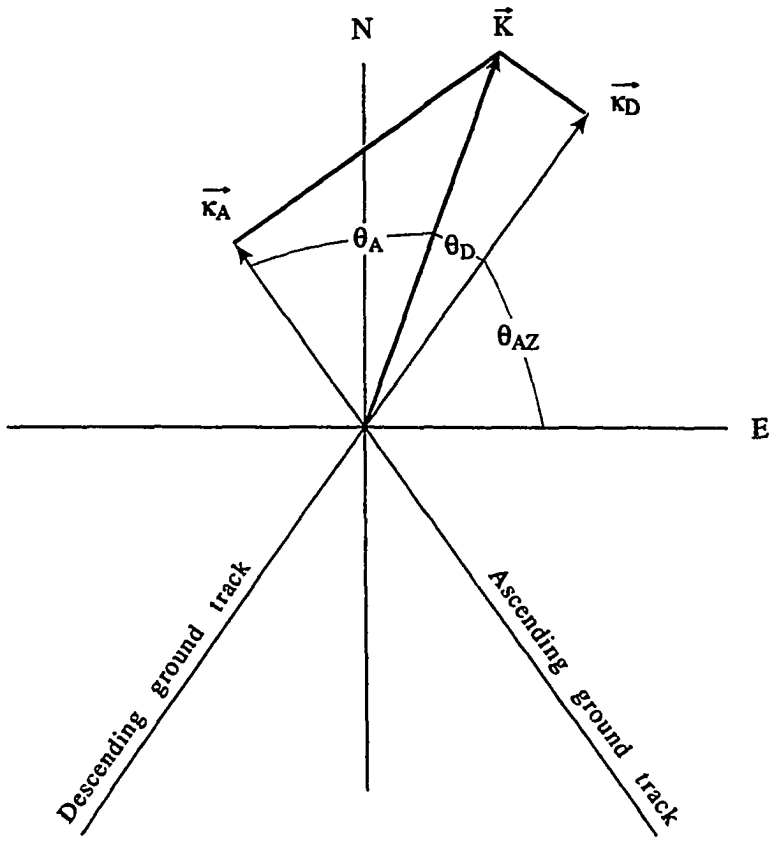

Figure 5.10 The geometry of the wave field relative to ascending and descending orbital ground tracks.

wave field appears to vary over three to four ERM orbital cycles (51-68 days). For the period from ERM 12 to ERM 18 the descending track peak wavelength is about 110 km with an average range of about 85 km to 155 km (again using the 0.3 R^2 contour as a bandwidth threshold). This estimate of peak wavelength also agrees closely with the corresponding spectral estimate.

From the geometry of the wave field relative to the orbital ground tracks (Figure 5.10), it is seen that

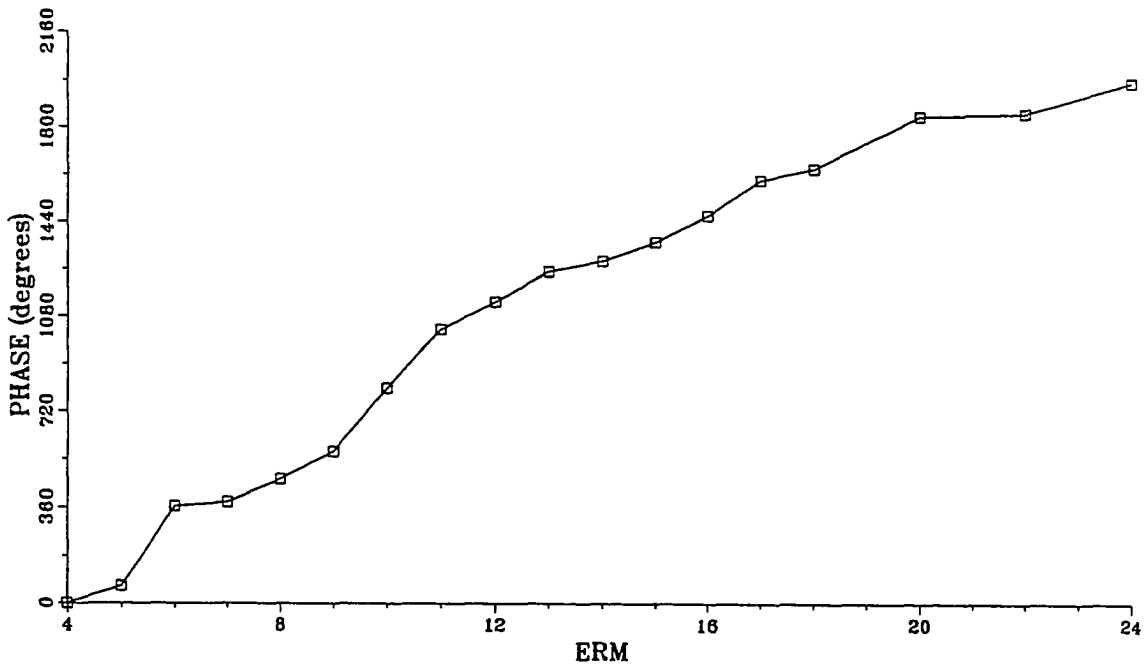

Figure 5.11 Time series of phase of the 165 km wave field along ground track A148 relative to its phase during ERM 4.

$$\theta_\Sigma = \theta_A + \theta_D = 2(90° - \theta_{AZ}) \tag{5.2}$$

where θ_A and θ_D are the respective angles between the wavenumber vector, $\vec{K}$, and the ascending and descending orbital ground tracks and where θ_{AZ} is the azimuthal angle between the orbital ground track and a local line of latitude. Additionally,

$$|\vec{K}| = \frac{|\overrightarrow{\kappa_{A,D}}|}{\cos \theta_{A,D}} \tag{5.3}$$

where $\overrightarrow{\kappa_A}$ and $\overrightarrow{\kappa_D}$ are the ascending and descending track wavenumber vectors. It follows from (5.2) and (5.3) that

$$\theta_{A,D} = \tan^{-1}\left(\frac{\frac{|\overrightarrow{\kappa_{D,A}}|}{|\overrightarrow{\kappa_{A,D}}|} - \cos\theta_{\Sigma}}{\sin\theta_{\Sigma}}\right). \qquad (5.4)$$

Solving (5.4) using θ_{AZ} (at 58°N) = 54.46°, $\kappa_A = 2\pi/165$ (-20,+20) km and $\kappa_D = 2\pi/110$ (+45,-25) km gives θ_A = 51.2° (range from 32.9° to 62.9°) and θ_B = 19.9° (range from 38.2° to 8.2°). Substituting these values into (5.3) inverting the results and multiplying by 2π gives the peak wavelength of the ERM 12-18 wave field as 103 km (range 122 km to 84 km). This is close to the 110 km wavelength subjectively estimated from Figure 5.7. The corresponding direction of propagation is 15.7°T (range from 357.4°T to 26.4°T).

Figure 5.11 shows the phase of the wave field along ground track A148 relative to its phase during ERM 4. Phase was determined from the coefficients in (5.1) with the wavelength estimate fixed at 165 km. The derivative (slope) of the curve represents the frequency of the wave field. A least squares procedure was used to estimate the slope between ERM orbital cycles 12-18 from which a wave period of 72.2 days was obtained. This is close to the wave period subjectively estimated from Figure 5.3. Limiting wave periods of 72.2 days and 68.3 days are obtained using the same procedure for limiting wavelengths 145 km and 185 km, respectively.

The orientation of the ascending ground tracks relative to the continental slope along the upstream portion of the BSC is not as advantageous for describing the local wave/eddy field as it is for the downstream portion. However, the profiles of SSH anomalies from an upstream location near the intersection (55.9°N,172°W) of ground tracks A150 (Figure 5.12) and D106 (Figure 5.13) indicate that there appear to be

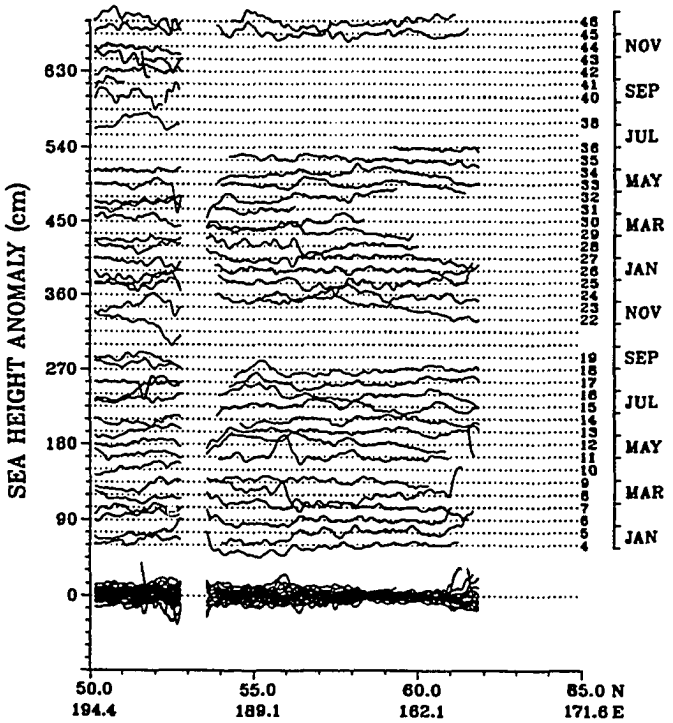

Figure 5.12 Same as Figure 5.3 only for ascending ground track A150.

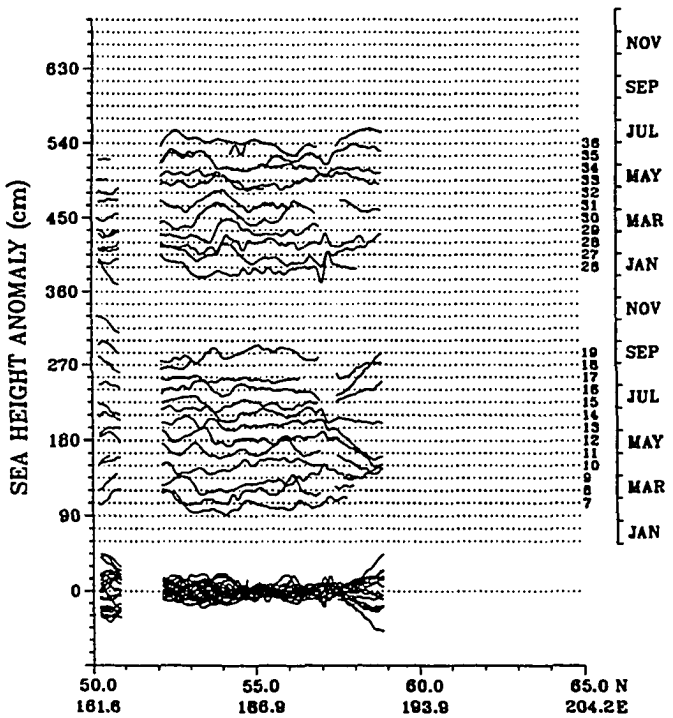

Figure 5.13 Same as Figure 5.3 only for descending ground track D106.

only two significant passing anomalies. These occur during ERMs 8 and 11, for which the central dates are 15 Mar 87 and 5 May 87, respectively. The absence of any significant anomalies during ERMs 12-18 suggests that the wave/eddy fields associated with the upstream and downstream portions of the BSC are dynamically dissimilar.

Section 5.2 Results

Because the wave field in the downstream leg of the Bering Slope Current appears to be longer lived and better developed than that in the upstream leg, this section will focus on the former. The relatively long wave period observed along the downstream leg of the Bering Slope Current and the limited offshore extent (measured from the shelf break) of the wave field suggest that these waves are topographic planetary waves. For topographic planetary waves which are long compared to the internal Rossby radius of deformation, the effects of stratification are negligible (LeBlond and Mysak, 1978). Paluskiewicz and Niebauer (1984) estimate the internal Rossby radius of deformation in the Bering Sea to be about 7.5 km which is much smaller than the 103 km wavelength estimated from the altimeter data. Therefore, the observed wave field is assumed to be barotropic. Barotropic planetary waves conserve potential vorticity, $(f + \zeta)/H$, i.e.

$$\frac{d}{dt}\left(\frac{f+\zeta}{H}\right) = 0 \tag{5.5}$$

in which f is the planetary vorticity (Coriolis parameter), ζ is the relative vorticity, and H is the depth of the water column. By introducing a mass transport stream function, φ, for which

$$Hu = -\frac{\partial \varphi}{\partial y}, \quad Hv = \frac{\partial \varphi}{\partial x}, \tag{5.6}$$

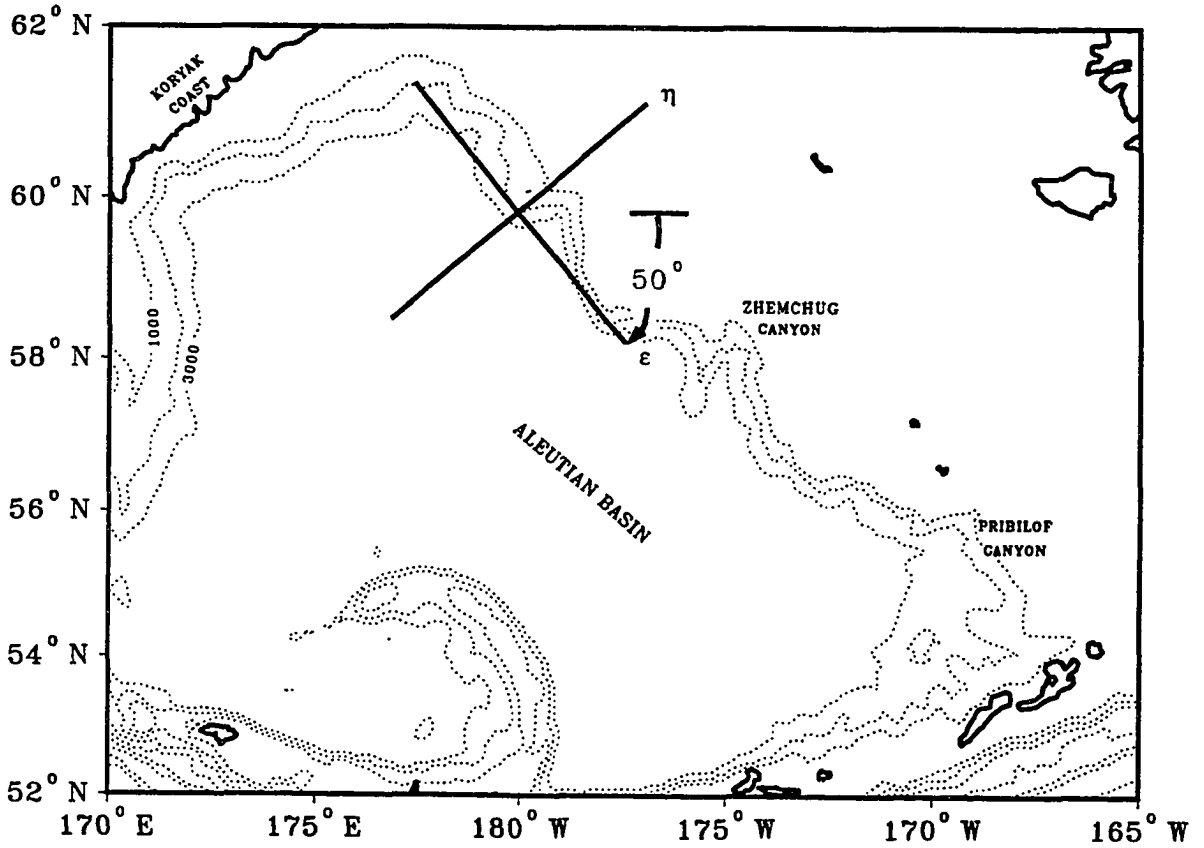

Figure 5.14 Geometry of the rotated coordinate system (ε, η) which is aligned so that $H \approx H(\eta)$.

the linearized form of (5.5) obtains

$$\left(\frac{\varphi_{xt}}{H}\right)_x + \left(\frac{\varphi_{yt}}{H}\right)_y - \left(\frac{f}{H}\right)_x \varphi_y + \left(\frac{f}{H}\right)_y \varphi_x = 0 \qquad (5.7)$$

where the subscripts denote partial derivatives.

Because topography is expected to influence the dynamics of the wave field it is convenient to change to a coordinate system aligned with the topography (ε, η), such that $H=H(\eta)$ (Figure 5.14). The new coordinate system is rotated at an angle θ to the x-axis

$$\varepsilon = x \cos\theta + y \sin\theta \tag{5.8}$$

$$\eta = -x \sin\theta + y \cos\theta. \tag{5.9}$$

Assuming that the stream function exhibits the characteristic time dependence $e^{-i\omega t}$ and invoking Rhines' (1969) 'first approximation' which allows terms proportional to $H^{-1}i\omega H_{x,y}$ to be neglected for low frequency waves (i.e. $\omega << f$), (5.7) becomes, in the rotated coordinate system,

$$\varphi_{\varepsilon\varepsilon} + \varphi_{\eta\eta} + \frac{i}{\omega}\left[\beta\left(\varphi_\varepsilon \cos\theta - \varphi_\eta \sin\theta\right) - f\frac{H_\eta}{H}\varphi_\varepsilon\right] = 0. \tag{5.10}$$

Substituting the stream function for two dimensional planetary waves

$$\varphi(\varepsilon,\eta) = \varphi_0 \exp\left[i(k\varepsilon + l\eta)\right] \tag{5.11}$$

into (5.10) gives the dispersion relation for barotropic topographic planetary waves

$$\omega = -\frac{\left(\beta(\cos\theta - \frac{l}{k}\sin\theta) - f\frac{H_\eta}{H}\right)k}{k^2 + l^2}. \tag{5.12}$$

The components of the phase velocity and group velocity are given by

$$\vec{c}_p = -\frac{\beta}{(k^2 + l^2)^2}(k^2, kl) \tag{5.13}$$

and

$$\vec{c}_g = \frac{\beta}{(k^2 + l^2)^2}(k^2 - l^2, 2kl). \tag{5.14}$$

respectively. In (5.13) and (5.14) β' is the topographically augmented β

$$\beta' = \beta \left(\cos\theta - \frac{1}{k}\sin\theta\right) + \frac{f}{L}. \tag{5.15}$$

in which $L = -(H_\eta/H)^{-1}$.

If the observed waves associated with the Bering Slope Current are, in fact, topographic planetary waves then the wave field should lie over topography characterized by a length scale appropriate for the wavelength and wave period determined from observations made by the GEOSAT altimeter. Therefore, altimetrically derived estimates of wavenumber and frequency, allow (5.12) to be solved for the topographic length scale,

$$L = -\left(\frac{H_\eta}{H}\right)^{-1} = -\frac{f\,k}{\omega\,(k^2 + l^2) + \beta\left(\cos\theta - \frac{1}{k}\sin\theta\right)k} \tag{5.16}$$

which can then be compared to the length scale computed from the local topography.

The longshore axis of the continental slope between Zhemchug Canyon and the Koryak coast is declined roughly 50 degrees from the lines of latitude. The period and wavelength previously estimated were 72.2 days and 103 km, respectively. The angle that the wavenumber vector makes with the longshore axis of the continental slope is about 124 degrees. Consequently, the wavenumbers, in the rotated coordinate system, are computed to be $k = 2\pi \cos(124°)/103\text{ km} = -3.411 \times 10^{-2}\text{ km}^{-1}$ and $l = 2\pi \sin(124°)/103\text{ km} = 5.057 \times 10^{-2}\text{ km}^{-1}$. The frequency is computed to be $\omega = 2\pi/(72.2\text{ d} \times 8.64 \times 10^4\text{ s d}^{-1}) = 1.007 \times 10^{-6}\text{ s}^{-1}$. At 58°N, $f = 1.237 \times 10^{-4}\text{ s}^{-1}$ and $\beta = 1.213 \times 10^{-8}\text{ s}^{-1}\text{ km}^{-1}$. Substituting these values into (5.16) gives a

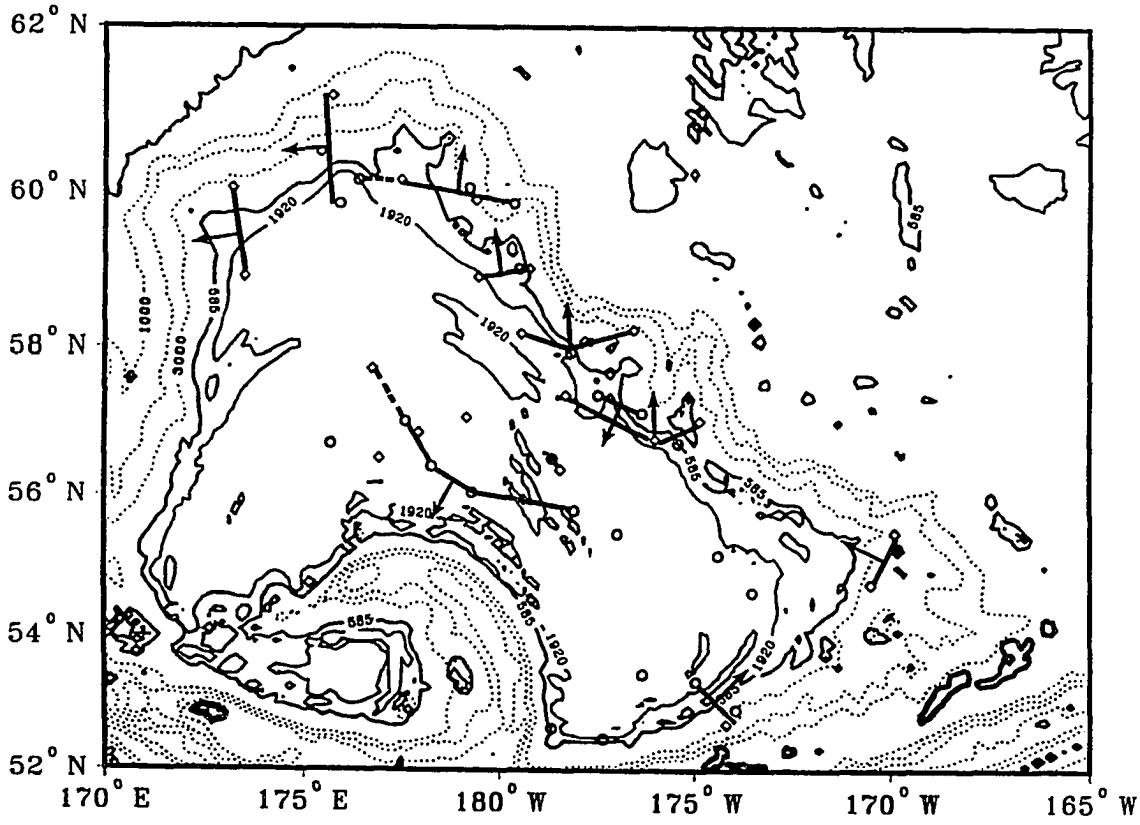

Figure 5.15 Location of the 585 km and 1920 km topographic length scale contours in relation to the ERM 16 wave crests.

topographic length scale, L, of about 1070 km. Substituting the limiting values for wavenumber and frequency into (5.16) gives topographic length scales ranging from 585 km to 1920 km. For comparison, the magnitude of the local topographic length scale was computed by central difference from a smoothed version (5 km radial smoothing, interpolated to a 1/6° x 1/12° grid, Δx = 1/3° and Δy = 1/6°) of the ETOPO5 bathymetric data set and the 585 km and 1920 km contours were plotted (Figure 5.15). The wave crests in the downstream leg of the Bering Slope Current are seen to straddle the limiting contours.

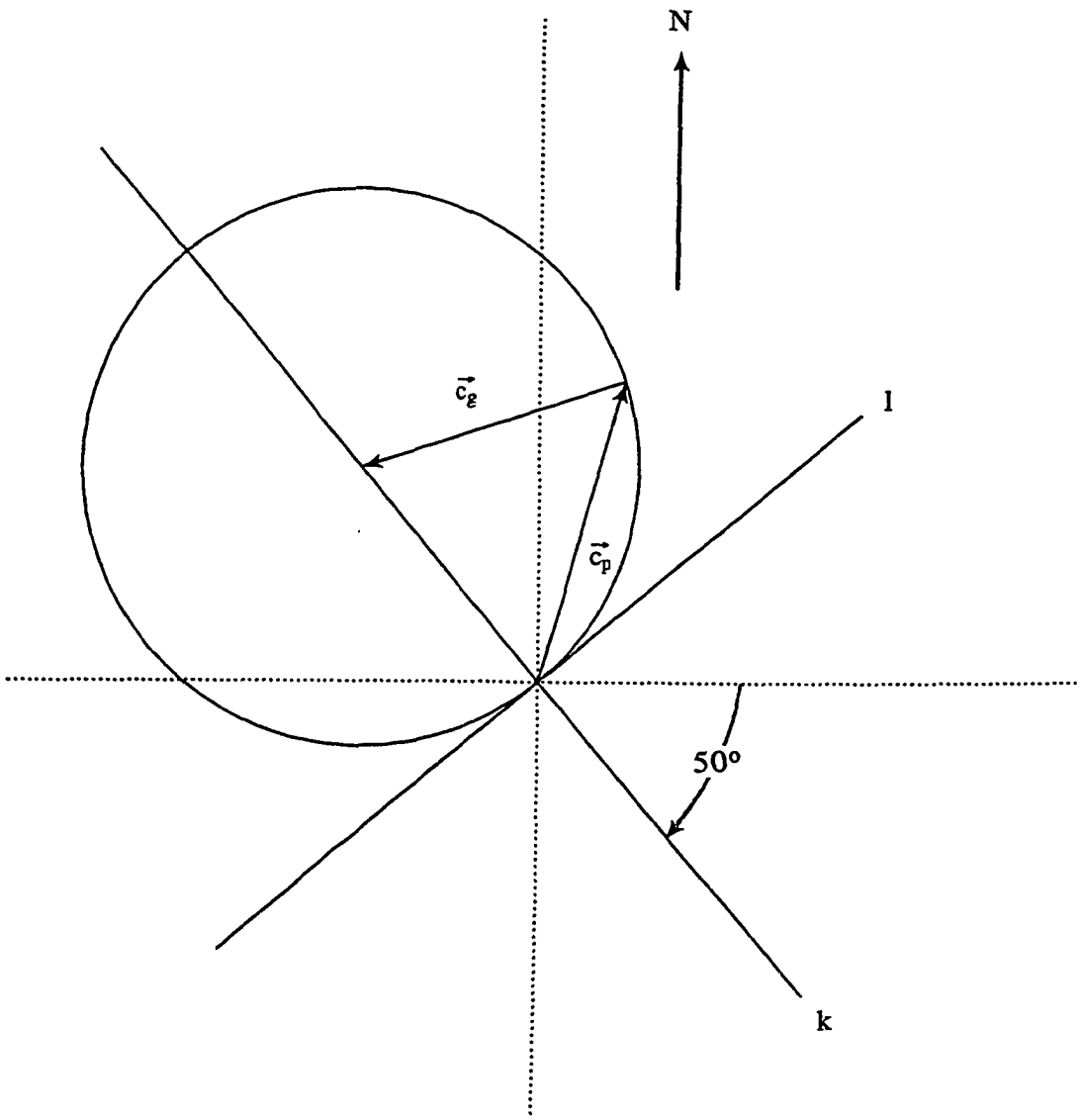

Figure 5.16 The slowness circle in rotated wavenumber space. The k wavenumber axis is approximately parallel to the longshore axis of the continental slope downstream from Zhemchug Canyon.

Solving (5.13) and (5.14) gives a phase velocity of 1.7 cm s^{-1} directed to the north-northeast and a group velocity of 2.9 cm s^{-1} directed to the west-southwest. This can be illustrated graphically by plotting the slowness

curve (a circle of constant wave frequency in wavenumber space) for the observed values in the rotated coordinate system (ε, η) (Figure 5.16). The center of the slowness circle is at $(-\beta'/2\omega, 0)$. Recalling that the longshore axis of the continental slope is parallel to the k axis, the direction of wave energy propagation, given by the group velocity vector, is seen to be away from the continental slope. This is the expected direction of energy propagation for waves forced at a boundary.

Assuming that the height of the downstream wave field, ξ, can be modeled as

$$\xi' = \xi_o \left[1 + \sin\left(\frac{2\pi}{\lambda_n} n\right)\right] \tag{5.17}$$

where n is the distance normal to the wave crest, the maximum geostrophic velocity can be estimated from the geostrophic equation

$$u = -\frac{g}{f}\frac{\partial \xi'}{\partial n}. \tag{5.18}$$

Using the values $g = 9.81$ m s^{-1}, $f = 1.237 \times 10^{-4}$ s^{-1}, $\lambda_n = 1.03 \times 10^5$ m, and $\xi_o =$ 0.06 m (the mean of the amplitudes obtained from (5.1) using the SSH anomalies along ground track A148 for ERMs 12-18) and solving for the derivative in (5.18) at $n = 0$, a maximum geostrophic velocity of about 29 cm s^{-1} is obtained. This value agrees reasonably well with the maximum surface baroclinic velocities computed by Kinder et al. (1975) for the BSC (their figures 13 and 14).

Section 5.3 Discussion and conclusions

The altimetrically observed wave field and underlying bottom topography have characteristics which have been shown to satisfy the dispersion relation for topographic planetary waves. The dispersion relation used to determine the topographic length scale, equation (5.12), ignored the presence of a mean flow associated with the BSC. Beginning again with (5.5) and letting the vorticity include a mean flow, $U(\eta)$, directed along the ε-axis

$$\zeta = \left(\frac{\phi_\varepsilon}{H}\right)_\varepsilon + \left(\frac{\phi_\eta}{H}\right)_\eta - U_\eta \tag{5.19}$$

the real portion of the resulting dispersion relation obtains

$$\omega = Uk - \frac{\left(\beta(\cos\theta - \frac{1}{k}\sin\theta) - f\frac{H_\eta}{H}\right)k}{k^2 + l^2} + \frac{\frac{\partial^2 U}{\partial \eta^2}k}{k^2 + l^2}. \tag{5.20}$$

Assuming a jet-like velocity profile for the northwestward flowing BSC, the first term on the right hand side of (5.20) is positive whereas the third term is negative (recall that $k<0$). Scaling the ratio of the first term to the third term gives

$$\frac{U(k^2 + l^2)}{\frac{\partial^2 U}{\partial \eta^2}} \sim \frac{L_{BSC}^2}{\lambda_{eddy}^2} \tag{5.21}$$

where L_{BSC} is the width of the BSC and λ_{eddy} is the wavelength of the topographic wave field. Consideration of Figures 5.5a and 5.5b, which show the wave field to be present along ground track A147 but not along A146, and of Figure 5.2, which shows the locations of these ground tracks in relation to the shelf break, allows an upper limit width for the BSC of roughly 150 km to be inferred. The actual width is somewhat less than this. While an accurate determination of the cross stream velocity profile is required, (5.21) demonstrates the possibility that the effects associated with the first and third terms of (5.20) can cancel one another and that the observed wave/eddy field can be reasonably described by (5.12).

It has been shown that during the spring and summer months a system of topographic planetary waves having a period of about 72 days and a wavelength of about 103 km propagated along the downstream leg of the Bering Slope Current. Recalling that the SSH anomalies associated with the Bering Slope Current were predominantly positive anomalies (Figure 5.3), the planetary wave field might manifest itself as a train of anticyclonic eddies. Paluskiewicz and Niebauer (1984) suggested that topographic planetary waves generated the eddies they observed in satellite infrared imagery of the eastern Bering Sea (the upstream leg of the Bering Slope Current). They estimated the along-slope wavelength of the eddy field to be about 140 km and the period to be about 84 days, values which are in reasonable agreement with the along-slope wavelength ($\lambda_\varepsilon = 2\pi/k = 184$ km) and the 72 day period estimated from the SSH anomaly data.

The east-west flow regime inferred east-west wave crest orientation over the continental slope downstream from Zhemchug Canyon is

qualitatively consistent with that indicated by the dynamic topography at that location presented by Kinder et al. (1975). While the authors also interpreted the eddy structures observed in their dynamic topography in terms of planetary waves, their estimated period (1.1 year) and wavelength (425 km) are much greater than those presented here. However, their estimates were based on the baroclinic flow field which may not correspond the barotropic field. Additionally, the alongshore spacing between their hydrographic transects was about 150 km (their Figures 2 and 16) which is not close enough to resolve the spatial scale of the wave field described above. This spacing would alias their results to longer wavelengths and longer wave periods. As a consequence, the estimated 1.1 year wave period, even ignoring topographic effects, is questionable.

Other dynamic topographies which indicate the presence of eddies or meanders associated with the Bering Slope Current have been presented by Takenouti and Ohtani (1974), Sayles et al. (1979), and most recently by Verkhunov and Tkachenko (1992). However, the accuracy with which these topographies reproduce the flow regime of the Bering Slope Current is likely diminished by their relatively coarse hydrographic sampling schemes.

Because the topographic wave field appears to be best developed in the spring and summer months and least developed in the late fall and early winter, wind forcing, which exhibits a strong annual variation over the Bering Sea (Hughes et al., 1974), suggests itself as a suitable modulating and/or generating mechanism. The evolution of the planetary wave field, represented by a time series of the band averaged (139 km to 185

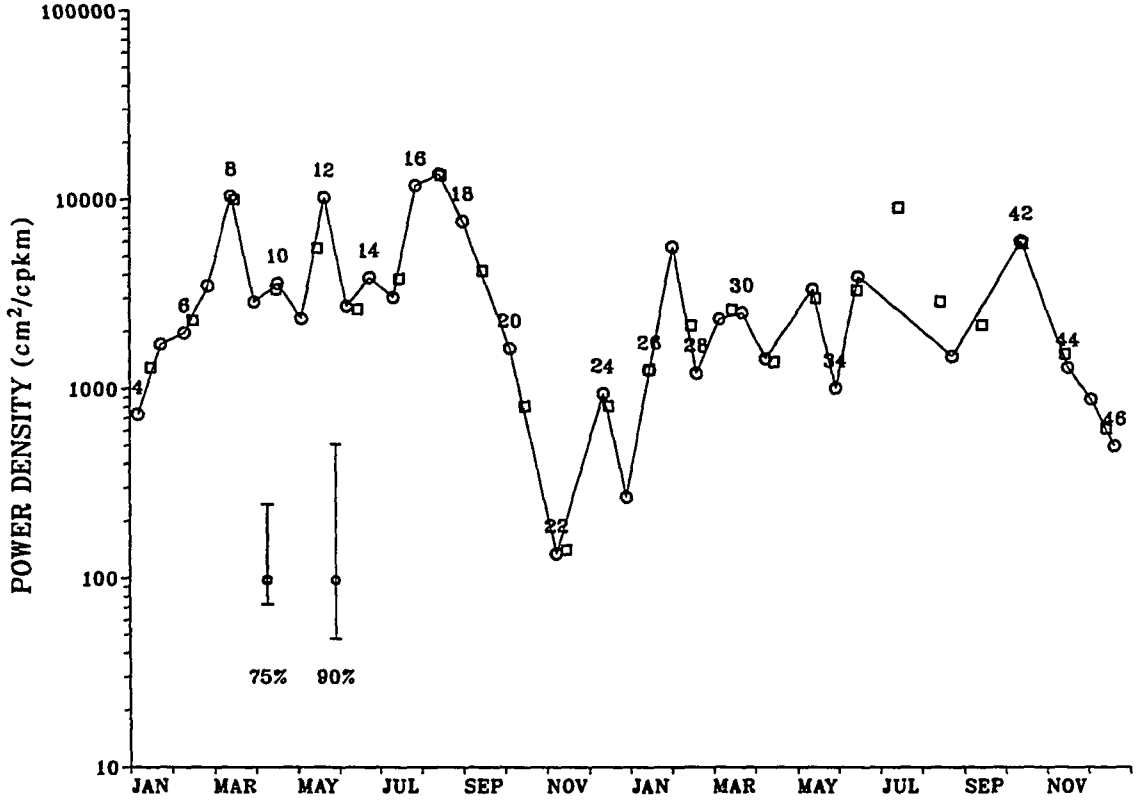

Figure 5.17 Two year (ERM 4-46) time series of average spectral power density for the wave band centered at 159 km (open circles). Open squares designate the power interpolated to mid-month.

km) power spectral density of the SSH anomalies along ground track A148 between 56.1°N and 60.1°N is shown in Figure 5.17. This wave band brackets the 159 km spectral peak of the ascending track anomalies (Figure 5.5c). A near annual signal characterizes the low frequency variability of the time series. Wave power is greatest during the spring and summer months for which it is significantly higher (> 90% C.I.) than during the late fall and early winter. During the spring and summer of 1987 (ERMs 8 to 17) wave power varies (> 75% C.I.) with a period of about 4

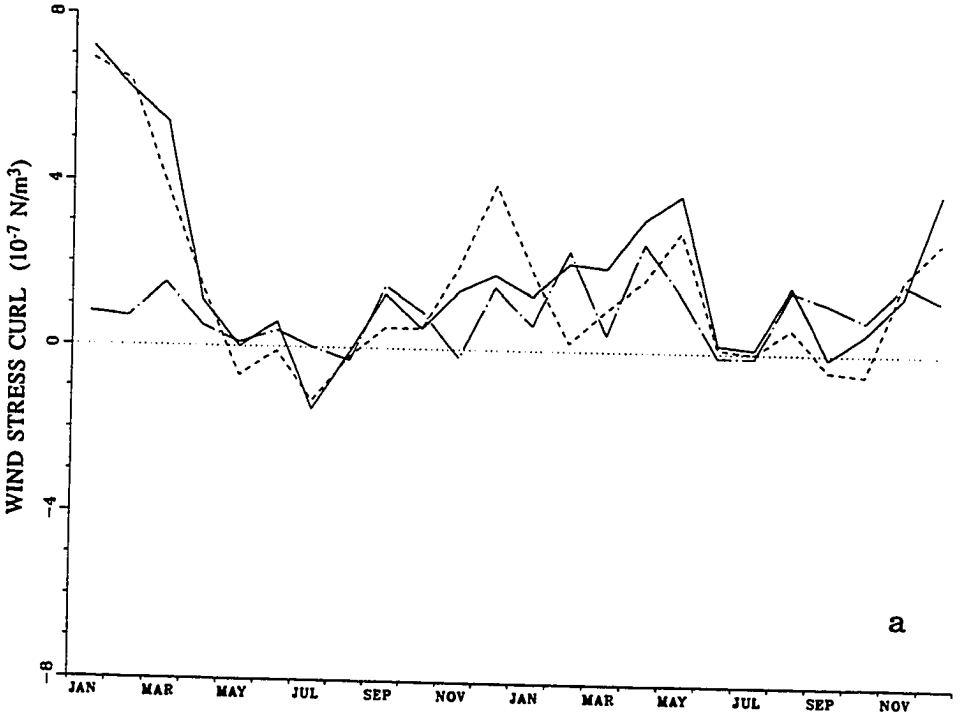

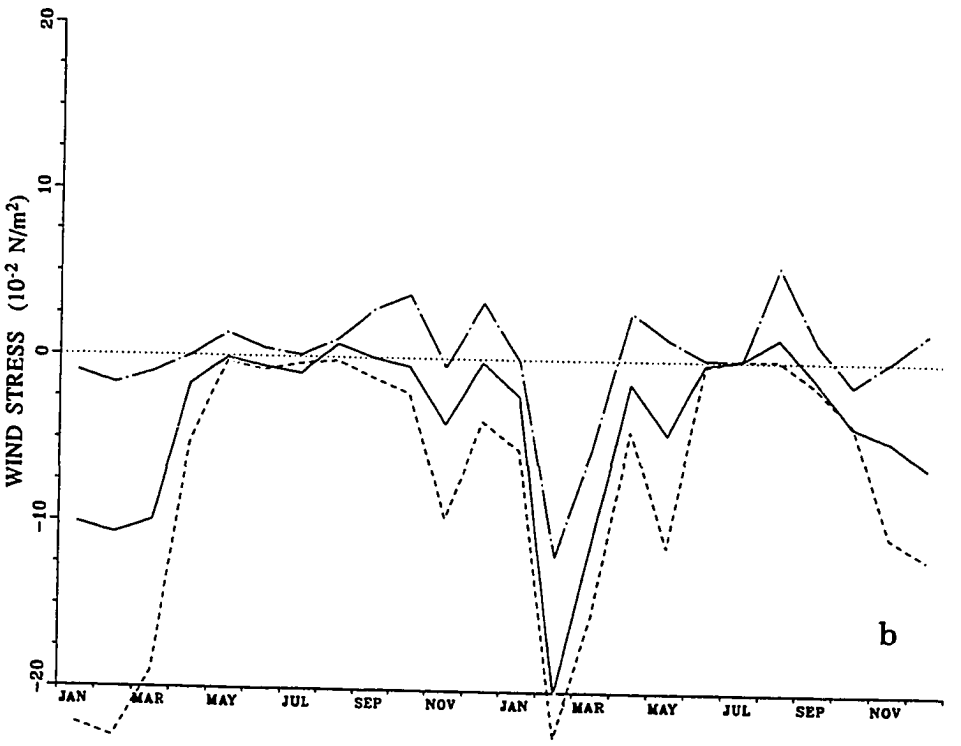

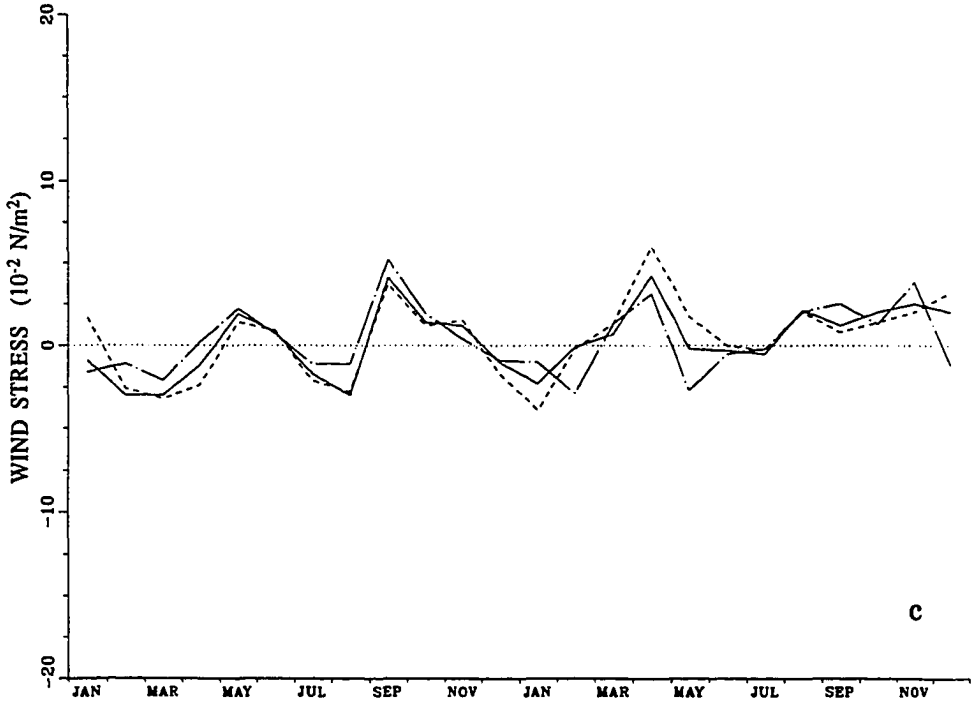

Figure 5.18 Two year time series of monthly values of (a) wind stress curl (b) cross-slope component of wind stress, τ^{η}, (c) along-slope component of wind stress, τ^{ε}, at 55.5°N, 190.0°E (chain dot), 57.0°N, 183.7°E (solid), and 59.0°N, 180.8°E (dash).

to 5 ERM orbital cycles (~68 to 85 days) which roughly approximates the 72 day period derived from the least squares procedure.

Figures 5.18a-c show the seasonal and interannual (1987-1988) variability in (a) wind stress curl (WSC) and (b) the cross-slope component of wind stress, τ^{η}, and (c) the along-slope component of wind stress, τ^{ε}, at three locations 55.5°N, 190.0°E; 57.0°N, 183.7°E; and 59.0°N, 180.8°E. The first location is near Pribilof Canyon, whereas, the second and third locations are near the ends of ground track segment A148. These three locations were chosen to allow the wind field over upstream, mid-stream

and downstream portions of the Bering Slope Current to be characterized and to illustrate any along-slope variation in the wind field. The wind data was computed from the 3^0 x 3^0 gridded FNOC monthly pressure data (see Salmon, 1992 for computational details) and interpolated to the given locations using the data at the four nearest FNOC grid points.

WSC at the mid-stream and downstream locations have prominent annual signals, in which the curl is strongly positive in late fall and early winter and near zero from spring to early fall. When the curl is near zero it varies with a 2 to 3 month period. WSC at the upstream location undergoes a much weaker annual variation upon which fluctuations having a 2 to 3 month period are superimposed. Comparison of Figures 5.17 and 5.18a indicates a near inverse relationship exists between WSC and the development of the wave field in which the relaxation of strong winter forcing by WSC coincides with the development of the topographic wave field while the fall intensification of WSC coincides with the decay of the topographic wave field.

The cross-slope component of wind stress also exhibits an annual signal at all three locations. The amplitude of this signal becomes progressively larger moving from southeast to northwest. The corresponding large annual signals evident in the plots of WSC and τ^{η} and their comparative absence in the plots of WSC and τ^{ε} imply that the along-slope variation in τ^{η} is the dominant component of WSC. As was the case for WSC the magnitude of τ^{η} is greatest during fall and winter and smallest during spring and summer.

The along-slope component of wind stress is remarkably similar at all three locations. The dominant period of variability is around 4 to 5 months with this signal being more pronounced in 1987 than in 1988.

Squared coherences between the wind forcing fields (input) and the wave power (output) were computed. The two year time series of wave power data which has an ERM sampling period of 17.05 days was interpolated to a one month period using a quadratic polynomial formed from the logarithms of wave power at the three nearest ERM sampling times. Only the first 18 months of data (zero padded to 24 months) were used to compute the squared coherences because the large gaps in the wave power data after ERM 35 resulted in some suspect interpolated monthly values (Figure 5.17). The shortness of the wave power time series allows only a very few comparative realizations of wind and wave processes. The resulting coarse spectral resolution and high significance thresholds impose severe statistical limitations on the analysis of the response of the topographic wave field to wind forcing.

Figure 5.19a shows that over the bandwidth of convolution averaging (0.2083 cpm) there is no significant coherence between WSC at any of the three locations and wave power. However, there is a coherence peak at 2.4 months (~73 days) for WSC at the mid-stream location. A corresponding local coherence minimum occurs for periods between 2.18 months and 2.67 months for WSC at the upstream location. This is interpreted to indicate that the topographic wave field is not remotely forced. Although tempered by the lack of statistical significance these observations suggest that the topographic wave field is locally forced by short period variability in WSC.

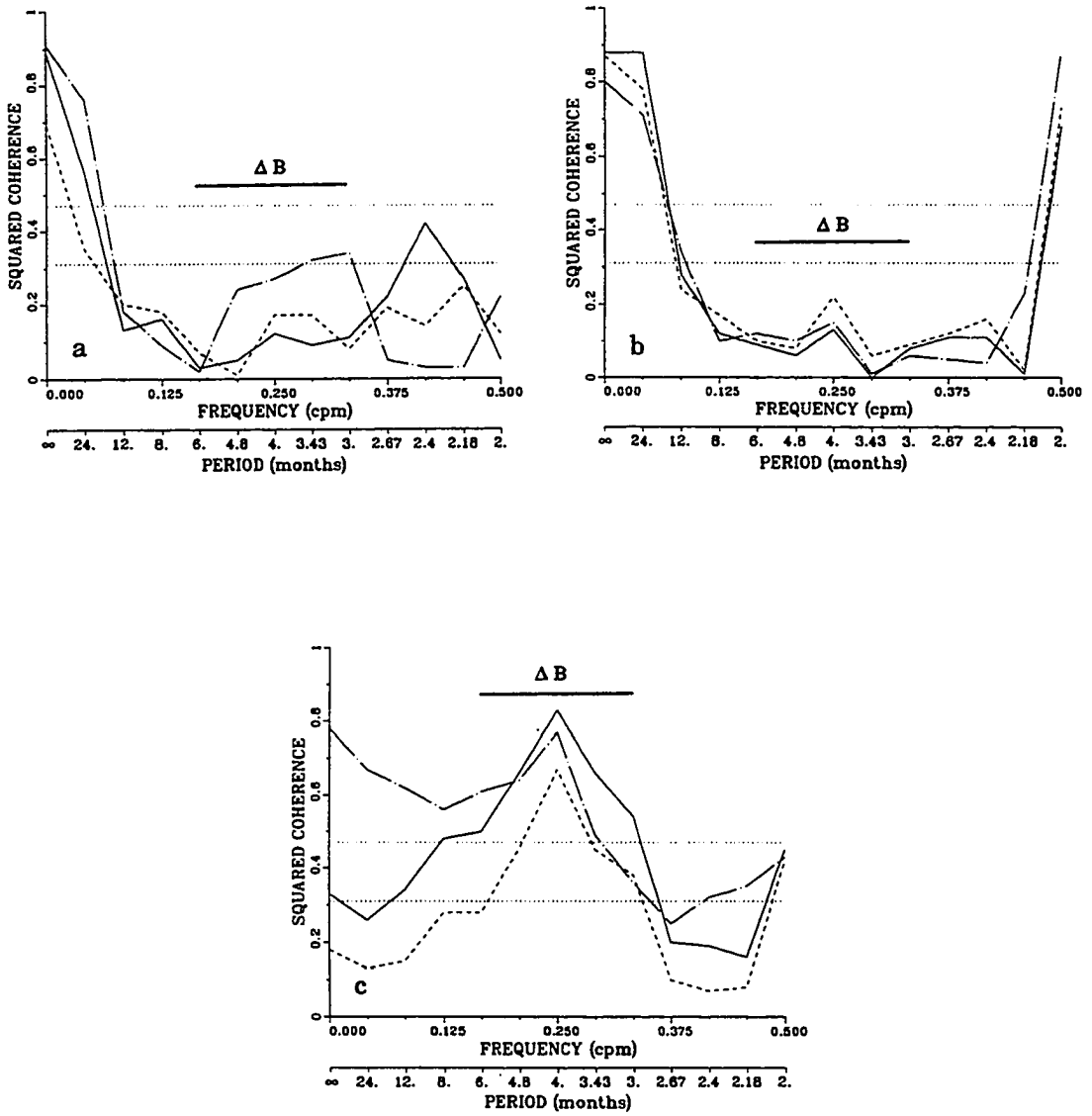

Figure 5.19 Squared coherence between topographic wave power and (a) WSC, (b) τ^{η}, (c) τ^{ε}, at 55.5°N, 190.0°E (chain dot), 57.0°N, 183.7°E (solid), and 59.0°N, 180.8°E (dash). Significance levels of 60% and 80% are shown as dotted lines. The solid horizontal line labeled ΔB indicates the bandwidth of convolution averaging (0.2083 cpm).

The squared coherences between cross-slope winds at all three locations and wave power exhibit a similar dependency on frequency (Figure 5.19b). In spite of the role cross-slope wind stress has with respect to WSC, comparison of Figures 5.19a and 5.19b indicate that it is WSC, not τ^{η}, that appears to force the topographic planetary wave field.

Figure 5.19c shows that overall, along-slope winds at the most southerly location are significantly coherent with wave power over a broad range of frequencies, whereas, the least significant coherence is associated with along-slope winds at the most northerly location. For all three locations the maximum coherence between τ^{ε} and wave power is at a period of 4 months. Interestingly, comparison of Figures 5.17 and 5.18c show that wave power peaks at very nearly the same times (ERMs 8, 12, and 17) that the magnitude of τ^{ε} peaks. This observation along with the observed coherences, suggests that the topographic planetary wave field responds to along-slope winds, but that along-slope winds are not themselves sufficient to generate the observed wave field.

These forcing mechanisms are also in evidence for what is arguably the most studied eastern boundary current, the California Current system. In her investigation of this current system, Hickey (1979) suggested both wind stress curl and the along-shore component of wind stress as forcing mechanisms. McCreary et al. (1987) showed that solutions to a viscid, linearized ocean model forced by wind stress curl and the along-shore component of wind stress reasonably described some features of the California Current system. In a more general investigation of eastern boundary currents Philander and Yoon (1982) show that a time dependent

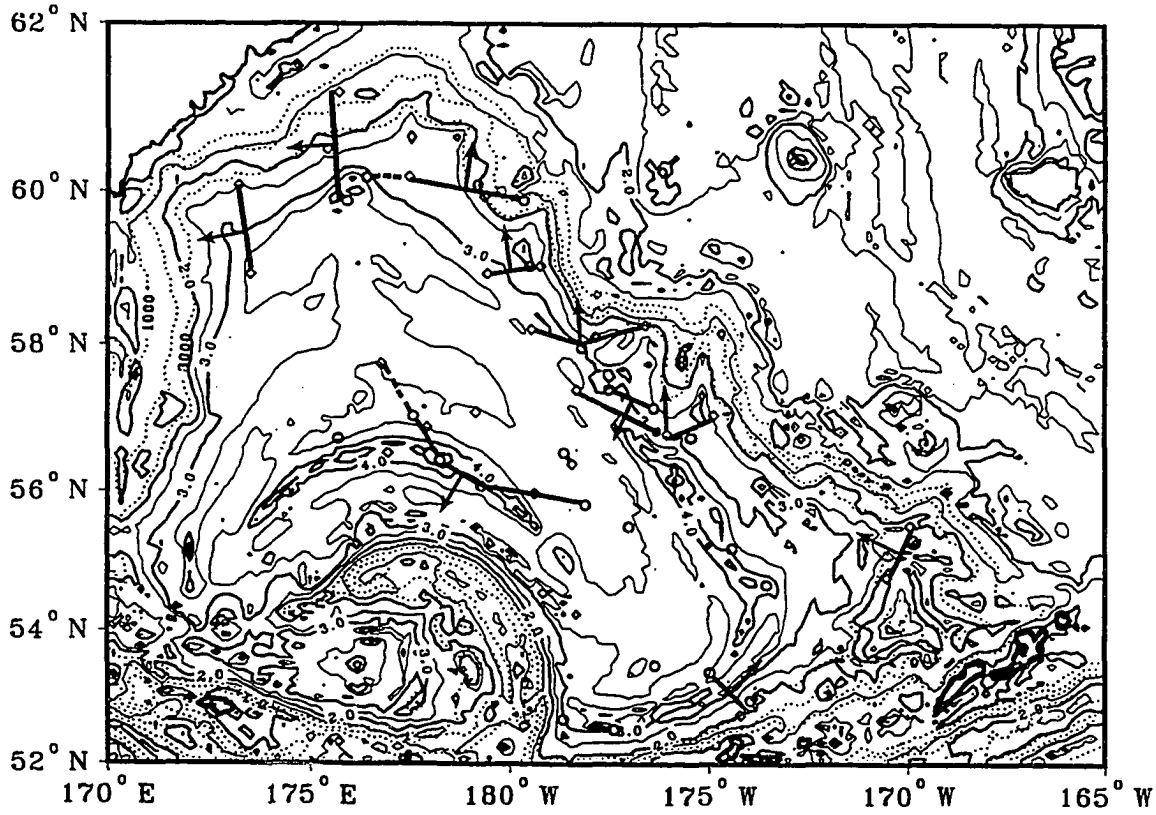

Figure 5.20 Plot of the topographic length scale, $L = -(H_\eta/H)^{-1}$, for the Aleutian Basin including wave crest locations. The contour interval is 0.5, in units of log L. The 1000 m, 2000m, and 3000m isobaths are shown as dotted lines.

along-shore component of wind stress can excite planetary waves along an eastern boundary.

A factor which may also contribute to the observed lower variability and the apparent absence of a persistent and well defined wave/eddy field in the upstream portion of the Bering Slope Current (Figure 5.1) is that in the upstream region, the topographic length scale, L, varies greatly across a relatively short off-slope distance (Figure 5.20). Near the shelf break the

characteristic topographic length scale is O(100 km) whereas just 100 km offshore from the shelf break the length scale is O(10000 km). For the downstream leg these length scales are O(100 km) and O(3000 km), respectively. Consequently, topographic beta varies more for water columns undergoing cross-slope excursions within much of the upstream leg *vis a vis* water columns undergoing similar excursions within the downstream leg of the Bering Slope Current. Alternately, the dispersive effects associated with the upstream topographic environment, as described by (5.12), are greater than those associated with the downstream topography. Manifestations of this would be a weaker, less persistent topographic wave field and reduced upstream SSH variability.

Wave scattering represents another mechanism which may effect the reduced variability in the upstream portion of the BSC. Planetary waves can be scattered by topographic features for which the radius of curvature is less than or equal to the wavelength of the incident wave (LeBlond and Mysak, 1978). While there are small corrugations in the topography of the upstream portion of the continental slope for which the local topographic radii of curvature are small, the west wall of Zhemchug Canyon is a very prominent topographic feature with a radius of curvature much less than the wavelength of the topographic waves (Figure 5.2). This feature can act to scatter the incident topographic planetary waves creating a shadow zone immediately downstream. The southwestward propagating wave crests in the central Aleutian Basin (Figure 5.7) which appear to have originated from the Zhemchug Canyon area may result from scattering. Royer and Emery (1984) reported on a satellite-tracked

drifter which followed a sinuous southwestward trajectory from Zhemchug Canyon across the central Bering Sea. Stabeno and Reed (1992) also reported on a drifter which followed a similar trajectory. A six year mean dynamic topography of the Bering Sea computed by Ohtani (1972) showed a chain of eddies north of Bowers Ridge whose axis lies on a line joining Near Strait and Zhemchug Canyon. Verkhunov and Tkachenko (1992) presented a fall 1990 dynamic topography for the western Bering Sea which also was suggestive of an eddy field between Near Strait and Zhemchug Canyon. Planetary wave scattering might be the mechanism responsible for these observations.

The particular geometry of the continental slope and orbital ground tracks in the central Bering Sea, in conjunction with the short orbital repeat period compared to the observed wave period, has allowed the barotropic topographic planetary wave field associated with the Bering Slope Current to be observed and described. The temporal and spatial variability of the wave field suggests the Bering Slope Current system is more complex than previously described. The proximity of the wave field to the shelf break might affect the cross-shelf transport of heat, salt, and nutrients thereby influencing the along-slope distribution and abundance of primary producers, zooplankton and fish stocks. Finally, the estimated wavelength and wave period suggest finer and more frequent sampling strategies for future hydrographic and biological surveys in the region.

Bibliography

Agreen, R.W. 1982. The 3.5 year GEOS-3 data set. NOAA Tech. Memo. NOS-NGS-33, Natl. Oceanic and Atmos. Admin., Rockville, Md.

Arsen'ev, V.S. 1967. Currents and water masses of the Bering Sea [In Russian, English summary]. Izd. Nauka, Moscow. (Transl., 1968., Nat. Mar. Fish. Serv. Northwest Fish. Center, Seattle, Wash.), 135 pp.

Born, G.H., J.A. Dunne, and D.B.Lame. 1979. Seasat mission overview. Science 204:1405-1406.

Brown, O.B., D.B. Olson, J.W. Brown, and R.H. Evans. 1983. Satellite infrared observation of the kinmatics of a warm-core ring. Aust. J. Mar. Freshwater Res. 34:535-545.

Calman, J. 1987. Introduction to Sea-surface Topography from Satellite Altimetry. *Johns Hopkins APL Technical Digest.* 8 (2), 206-211.

Cartwright, D.E. and R.D. Ray. 1990. Oceanic tides from Geosat altimetry. J. Geophys. Res. 95:3069-3090.

Chelton, D.B., M.G. Schlax, D.L. Witter, and J.G. Richman. 1990. Geosat altimeter observations of the surface circulation of the Southern Ocean. J. Geophys. Res. 95:17877-17903.

Cheney, R.E., B.C. Douglas, R.W. Agreen, L.L. Miller, and D.L. Porter. 1987. Geosat altimeter geophysical data record (GDR) user handbook. NOAA Tech. Memo NOS-NGS-46.

Cheney, R.E. and J.G. Marsh. 1981. Oceanic eddy variability measured by GOES 3 altimeter crossover differences. EOS. **62**:743-752.

Cheney, R.E., J.G. Marsh, and B.D.Beckley. 1983. Global mesoscale variability from collinear tracks of Seasat altimeter data. J. Geophys. Res. **88**:4343-4354.

Davis, C.S. and P.H. Wiebe. 1985. Macrozooplankton biomass in a warm-core Gulf Stream ring: Time series changes in size structure, taxonomic composition, and vertical distribution. J. Geophys. Res. **90**:8871-8874.

Dobrovol'skii, A.D. and V.S. Arsen'ev. 1959. On the question of the currents of the Bering Sea [in Russian]. Probl. Severa **3**:3-9. (Transl., Nat. Res. Coun. Can., Ottawa).

Douglas, B.C. and R.E. Cheney. 1981. Ocean mesoscale variability from repeat tracks of Geos 3 altimeter data. J. Geophys. Res. **86**:10931-10937.

Douglas, B. C. and P.D. Gaborski. Observation of sea surface topography with Geos 3 altimeter data. J. Geophys. Res. **84**:3893-3896.

Emery, W.J., T.C. Royer, and R.W. Reynolds. 1985. The anomalous tracks of North Pacific drifting buoys 1981 to 1983. Deep-Sea Research. **32**:315-347.

Favorite, F. 1967. The Alaskan Stream. Bull. Int. North Pacific Fish. Comm. 21: 1-20.

Favorite, F. 1974. Flow into the Bering Sea through Aleutian island passes. Ch. 1. In *Oceanography of the Bering Sea, with emphasis on renewable resources*, ed. D.W. Hood and E.J. Kelley, 3-37, Publ.2, Inst. Mar. Sci., Univ. of Alaska, Fairbanks.

Favorite, F., A.J. Dodimead, and K. Nasu. 1976. Oceanography of the subarctic Pacific region. Inter. N. Pac. Fish. Comm. Bull. 33.

Firing, E. and R.C. Beardsley. 1976. The behavior of a barotropic eddy on a β-plane. J. Phys. Oceanogr. 6:57-65.

Fugilister, F.C. and L.V. Worthington. 1951. Some results of a multiple ship survey of the Gulf Stream. Tellus. 3:1-14.

Gill, A.E. 1982. *Atmosphere-Ocean Dynamics, Int. Geophys. Ser.* vol. 20, ed. W.L. Donn, 662 pp., Academic, New York.

Gill, A.E., J.S.A. Green, and A.J. Simmons. 1974. Energy partition in the large scale ocean circulation and production of mid-ocean eddies. Deep-Sea Res. 21:499-528.

Greenwood, A.L., A. Nathan, G. Neumann, W.J. Pierson, F.C. Jackson, and T.E. Pease. 1969. Oceanographic applications of radar altimetry from a spacecraft. Remote Sensing Environ. 1:71-80.

Hickey, B.M. 1979. The California Current System- hypotheses and facts. Prog. Oceanog. 8:191-279.

Hooker, S.B. and D.B.Olson. 1984. Center of mass estimation in closed vortices: A verification in principle and practice. J. Atmos. and Oceanic Technol. 1:247-255.

Hood, D.W. and E.J. Kelley. 1974. Introduction. In *Oceanography of the Bering Sea, with emphasis on renewable resources*, ed. D.W. Hood and E.J. Kelley, xv-xxi, Publ.2, Inst. Mar. Sci., Univ. of Alaska, Fairbanks.

Hughes, F.W., L.K. Coachman, and K. Aagard. 1974. Circulation, transport, and water exchange in the western Bering Sea. Ch. 3. In *Oceanography of the Bering Sea, with emphasis on renewable resources*, ed. D.W. Hood and E.J. Kelley, 59-98, Publ.2, Inst. Mar. Sci., Univ. of Alaska, Fairbanks.

Jacobs, G. A., G.H. Born, and M.E. Parke. 1991. Construction of the global annual cycle from GEOSAT altimeter data with an estimation of the M2 tidal error. Eos. **72**:258.

Kelly, K.A., and S.T. Gille. 1990. Gulf Stream surface transport and statistics at 69°W from the Geosat altimeter. J. Geophys. Res. **95**:3149-3161.

Kinder, T.H., D.C. Chapman, and J.A. Whitehead, Jr. 1986. Westward intensification of the mean circulation on the Bering Sea shelf. J. Phys. Oceanogr. **16**:1217-1229.

Kinder, T.H., L.K. Coachman, and J.A. Galt. 1975. The Bering Slope Current System. J. Phys. Oceanogr. 5:231-244.

Kinder, T.H. and L.K. Coachman. 1977. Observation of a bathymetrically trapped current ring. J. Phys. Oceanogr. 7:946-952.

Kinder, T.H. and L.K. Coachman. 1978. The front overlaying the continental slope of the eastern Bering Sea. J. Geophys. Res. 83: 4551-4559.

Kinder, T.H. and J.D. Schumacher. 1981a. Hydrographic structure over the continental shelf of the southeastern Bering Sea. In *The Eastern Bering Sea Shelf: Oceanography and Resources*, ed. D.W. Hood and J.A. Calder, 31-52, University of Washington Press.

Kinder, T.H. and J.D. Schumacher. 1981b. Circulation over the continental shelf of the southeastern Bering Sea. In *The Eastern Bering Sea Shelf: Oceanography and Resources*, ed. D.W. Hood and J.A. Calder, 53-75, University of Washington Press.

Leben, R. R., G.H. Born, J.D. Thompson, and C.A. Fox. 1990. Mean sea surface and variability of the Gulf of Mexico using Geosat altimetry data. J. Geophys. Res. 95:3025-3032.

LeBlond, P.H. and L.A. Mysak. 1978. *Waves in the Ocean.* Elsevier. Amsterdam

Lybanon, M., and R.L. Crout. 1987. The NORDA GEOSAT oceans applications program. Johns Hopkins APL Technical Digest. 8:212-218.

Matthews, P.E., M.A. Johnson, and J.J. O'Brien. 1992. Observation of mesoscale features in the northeast Pacific using Geosat radar altimetry. J. Geophys. Res. 97:17829-17840.

McConathy, D.R. and C.C. Kilgus. 1987. The Navy GEOSAT Mission: An Overview.*Johns Hopkins APL Technical Digest.* 8 (2), 170-175.

McCreary, J.P., P. Kundu, and S-Y. Chao. 1987. On the dynamics of the California Current system. J. Mar. Res. 45:1-32.

McEwen, G.F., T.G. Thompson, and R. Van Cleve. 1930. Hydrographic sections and calculated currents in the Gulf of Alaska, 1927 and 1928. Report of the International Fisheries Commmission. 4:5-36.

Natarov, V.N. 1963. Water masses and currents of the Bering Sea [in Russian]. *Trudy VNIRO* 48:111-133. (Transl., 1968, in *Soviet fisheries investigations in the northeastern Pacific*, Part 1, pp.110-130, avail. Nat.Tech. Inf. Serv., Springfield Va., TT 67-51203).

Ohtani, K. 1965. On the Alaska Stream in summer. Bull. Fac. Fish. Hokkaido Univ. 15: 260-273.

Ohtani, K., Y. Akibi, and Y. Takenouti. 1972. Formation of Western subarctic water in the Bering Sea. In *Biological oceanography of the northern North Pacific Ocean*, ed. A.Y. Takenouti et al. Idemitsu-shoten, Tokyo, pp. 31-44.

Olson, D.B. 1980. The physical oceanography of two rings observed by the cyclonic ring experiment, Part 2, Dynamics. J. Phys. Oceanogr. 10:514-528.

Olson, D.B., R.W. Schmitt, M. Kennelly, and T.M. Joyce. 1985. A two-layer diagnostic model of the long-term physical evolution of warm-core ring 82B. J. Geophys. Res. **90**:8813-8822.

Overland, J.E. and R.W. Preisendorfer. 1982. A significance test for principal components applied to cyclone climatology. Mon. Wea. Rev. **110**:1-4.

Overland, J.E. and A.T. Roach. 1987. Northward flow in the Bering and Chukchi Seas. J. Geophys. Res. **92**:7097-7105.

Paluszkiewicz, T. and H.J. Niebauer. 1984. Satellite observations of circulation in the eastern Bering Sea. J. Geophys. Res. **89**:3663-3678.

Pedlosky, J. 1987. *Geophysical Fluid Dynamics.* 624 pp., Springer-Verlag, New York.

Philander, S.G.H. and J.H. Yoon. 1982. Eastern boundary currents and coastal upwelling. J. Phys. Oceangr. **12**:862-879.

Ratmanov, G.E. 1937. On the hydrology of the Bering and Chukchi seas [in Russian]. *Issled. Morei SSSR. Gidrometeoizdat* (Leningrad) **25**:10-118, (Transl., avail. Univ. Wash. Lib., Seattle).

Reed, R.K. 1984. Flow of the Alaskan Stream and its variations. Deep-Sea Research. **31**:369-386.

Reed, R.K. 1990. A year-long observation of water exchange between the North Pacific and the Bering Sea. Limnol. Oceanogr. **35**:1604-1609.

Reed, R.K., F.I. Gonzalez, and L. Miller. 1991. On the structure and stability of the Alaskan Stream. J. Marine. Res. **49**:719-726.

Reed, R.K. and J.D. Schumacher. 1986. Physical Oceanography. Ch. 3. In *The Gulf of Alaska, Physical Environment and Biological Resources*, ed. D.W. Hood and S.T. Zimmerman, 57-75.

Reid, J.L. 1973. *Northwest Pacific Ocean waters in winter.* The Johns Hopkins University Press. Baltimore.

Rhines, P.B. 1969. Slow oscillations in an ocean of varying depth. Part 1. Abrupt topography. J. Fluid Mech. **37**:161-189.

Robinson, A.R. and J.C. McWilliams. 1974. The baroclinic instability of the open ocean. J. Phys. Oceanogr. **4**:281-294.

Robinson, I.S. 1985. *Satellite Oceanography, an introduction for oceanographers and remote sensing scientists*, Ellis Horwood Ltd.,Chichester, England

Royer, T.C. 1981. Baroclinic transport in the Gulf of Alaska Part I. Seasonal variations of the Alaska Current. J. Mar. Res. **39**:239-250.

Royer, T.C. and W.J. Emery. 1984. Circualtion in th Bering Sea, 1982-1983, based on satellite-tracked drifter observations. J. Phys. Oceanogr. **14**:1914-1920.

Sailor, R.V. and A.R. LeShack. 1987. Preliminary determination of the GEOSAT radar altimeter noise spectrum. *Johns Hopkins APL Technical Digest.* 8 (2), 182-183.

Salmon, D.K. 1992. On interannual variability and climate change in the North Pacific. Phd. thesis, 219 pp., University of Alaska Fairbanks.

Sayles, M.A., K. Aagaard, and L.K. Coachman. 1979. *Oceanographic Atlas of the Bering Sea Basin*, University of Washington Press, Seattle.

Schwiderski, E.W. 1980. On charting global tides. Rev. of Geophys. Space Phys. 18:243-268.

Stabeno, P.J. and R.K. Reed. 1991. Recent Langrangian measurements along the Alaskan Stream. Deep-Sea Res. 38:289-296.

Tabata, S. 1982. The anticyclonic, baroclinic eddy off Sitka, Alaska in the northeast Pacific Ocean. J. Phys. Oceanogr. 12:1260-1282.

Takenouti, A.Y. and K. Ohtani. 1974. Currents and water masses in the Bering Sea: A review of Japanese work. Ch. 2. In *Oceanography of the Bering Sea, with emphasis on renewable resources*, ed. D.W. Hood and E.J. Kelley, 39-57, Publ.2, Inst. Mar. Sci., Univ. of Alaska, Fairbanks.

Thomson, R.E. 1972. On the Alaskan Stream. J. Phys. Oceanogr. 2:363-371.

Thompson, J.D., G.H. Born, G.A. Maul. 1983. Collinear-track altimetry in the Gulf of Mexico from SEASAT: measurements, models, and surface truth. J. Geophys. Res. 88:1625-1636.

Toulany, B. and C. Garrett. 1984. Geostrophic control of fluctuating barotropic flow through straits. J. Phys. Oceanogr. **14**:649-655.

Verkhunov, A.V. and Y.Y. Tkachenko. 1992. Recent observations of variability in the western Bering Sea current system. J. Geophys. Res. **97**:14369-14376.

Wakker, K.F., R.C.A. Zandbergen, M.C. Naeije, and B.A.C. Ambrosius. 1990. Geosat altimeter data analysis for the oceans around South Africa. J. Geophys. Res. 95:2991-3006.

Weare, B.C., A.R. Navato, and R.E. Newell. 1976. Empirical orthogonal analysis of Pacific sea surface temperatures. J. Phys. Oceanogr. **6**:671-678.

White, W.B. and S. Tabata. 1987. Interannual westward-propagating baroclinic long-wave activity on Line P in the eastern midlatitude North Pacific. J. Phys. Oceanogr. 17:385-396.

White, W.B. and C-K Tai. 1990. Continuous assimilation of Geosat altimetric sea level observations into a numerical synoptic ocean model of the California Current. **95**:3127-3148.

Wiebe, P.H., G.R. Flierl, C.S. Davis, V. Barber, and S.H. Boyd. 1985. Macrozooplankton biomass in Gulf Stream warm-core rings: Spatial distribution and temporal changes. J. Geophys. Res. **90**:8885-8902.

Wyrtki, K., L. Magaard, and J. Hager. 1976. Eddy energy in the oceans. J. Geophys. Res. **81**:2641-2646.

Zlotnicki, V., L.-L. Fu, and W. Patzert. 1989. Seasonal variability in global sea level observed with Geosat altimetry. J. Geophys. Res. 94:17959-17969.

Zlotnicki, V., A. Hayashi, and L.-L. Fu. 1990. The JPL-Oceans-8902 version of Geosat altimetry data. JPL Tech. Rep. JPL D-6939.